

An Experimental Study of a Three-Dimensional Thrust Augmenting Ejector Using Laser Doppler Velocimetry

Bruce L. Storms

(NASA-CR-177531) AN EXPERIMENTAL STUDY OF A
THREE-DIMENSIONAL THRUST AUGMENTING EJECTOR
USING LASER DOPPLER VELOCIMETRY (California
Polytechnic State Univ.) 132 p CSCI 20D

N89-24569

G3/34 Unclass
0212676

CONTRACT NCC2-484
May 1989



National Aeronautics and
Space Administration

An Experimental Study of a Three-Dimensional Thrust Augmenting Ejector Using Laser Doppler Velocimetry

Bruce L. Storms

California Polytechnic State University, San Luis Obispo, California

Prepared for
Ames Research Center
CONTRACT NCC2-484
May 1989



National Aeronautics and
Space Administration

Ames Research Center
Moffett Field, California 94035

Table of Contents

	Page
List of Tables.....	iv
List of Figures	v
Nomenclature	xi
Abstract	1
CHAPTER 1: Introduction.....	3
CHAPTER 2: Experimental System.....	13
CHAPTER 3: Results and Discussion.....	25
CHAPTER 4: Conclusions	39
References.....	41
Appendices:	
APPENDIX A: Tables and Figures	43
APPENDIX B: Sample Calculations	113
APPENDIX C: LDV Performance.....	119

PRECEDING PAGE BLANK NOT FILMED

List of Tables

	Page
1. Ejector geometry. All dimensions in millimeters.	44
2. Survey locations. H = hot wire; L = LDV.	44
3. Calculated jet exit velocities for $z/d=-2.6$. (All values in m/s)	45
4. Calculated jet exit velocities for $z/d=-3.9$. (All values in m/s)	46
5. Calculated jet exit velocities for $z/d=-5.2$. (All values in m/s)	47

List of Figures

	Page
1. Thrust augmenting ejector concepts for V/STOL aircraft from Ref. 1.	48
2. Axial velocity profiles in the mixing chamber of the two-dimensional ejector studied in Ref. 4 using laser Doppler velocimetry. Open symbols represent constant area ejector. Solid symbols represent diffused flow ejector. \square , Pr=1.06; \circ , Pr=1.45; Δ , Pr=2.04; \diamond , Pr=1.06 one velocity component LDV system.	49
3. Axial turbulence intensity profiles in the mixing chamber. For a key to the symbols, see the caption of Figure 2.	50
4. Transverse turbulence intensity profiles in the mixing chamber. For a key to the symbols, see the caption of Figure 2.	51
5. Reynolds stress profiles in the mixing chamber. For a key to the symbols, see the caption of Figure 2.	52
6. Regions of the ejector flow field defined by Ref. 4 and 5.	53
7. Hypermixing nozzle exit studied in Ref. 8.	54
8. Cross slot nozzle exit studied in Ref. 9.	55
9. Growth of axisymmetric free jet with and without pulsations obtained in Ref. 10 using hot wire anemometry.	56
10. Constant area ejector geometry showing primary nozzle and mixing chamber.	57
11. Primary nozzle geometry. All dimensions in millimeters.	58
12. Plumbing schematic for primary air supply.	59
13. Secondary air plenum with vertical perforated pipe. All dimensions in millimeters.	60

14. Three segments of ejector nozzle showing vertical measurement stations.	61
15. LDV optics for color separation and coupling to fiber optic cables.	62
16. Fiber-optic probe in backscatter configuration.	63
17. LDV forward scatter configuration.	64
18. Laser Doppler velocimeter focal volume.	65
19. Mineral oil seeding device.	66
20. Diagnostic print out generated by LDV and hot wire data acquisition routines.	67
21. Axial velocity profiles at $z/d = -2.6$ obtained by LDV (□) and hot wire anemometry (♦) for $0 \leq x/L \leq 0.29$.	68
22. Axial velocity profiles at $z/d = -2.6$ obtained by LDV (□) and hot wire anemometry (♦) for $0.44 \leq x/L \leq 1.2$.	69
23. Axial velocity profiles at $z/d = -3.9$ obtained by LDV (□) and hot wire anemometry (♦) for $0 \leq x/L \leq 0.29$.	70
24. Axial velocity profiles at $z/d = -3.9$ obtained by LDV (□) and hot wire anemometry (♦) for $0.44 \leq x/L \leq 1.2$.	71
25. Axial velocity profiles at $z/d = -5.2$ obtained by LDV (□) and hot wire anemometry (♦) for $0 \leq x/L \leq 0.29$.	72
26. Axial velocity profiles at $z/d = -5.2$ obtained by LDV (□) and hot wire anemometry (♦) for $0.44 \leq x/L \leq 1.2$.	73
27. Axial velocity profiles at $x/L = 0.02$ obtained by LDV and normalized by the calculated jet exit velocity.	74
28. Axial velocity profiles at $z/d = -2.6$ (□), -3.9 (Δ), and -5.2 (♦) obtained by LDV for $0.44 \leq x/L \leq 1.2$.	75
29. Centerline velocity results including free jet data from Ref. 4.	76

30. Evolution of the normalized jet width including free jet data from Ref. 4.	77
31. Transverse velocity profiles at $z/d = -2.6$ obtained by LDV (■) and hot wire anemometry (♦) for $0 \leq x/L \leq 0.29$.	78
32. Transverse velocity profiles at $z/d = -2.6$ obtained by LDV (■) and hot wire anemometry (♦) for $0.44 \leq x/L \leq 1.2$.	79
33. Transverse velocity profiles at $z/d = -3.9$ obtained by LDV (■) and hot wire anemometry (♦) for $0 \leq x/L \leq 0.29$.	80
34. Transverse velocity profiles at $z/d = -3.9$ obtained by LDV (■) and hot wire anemometry (♦) for $0.44 \leq x/L \leq 1.2$.	81
35. Transverse velocity profiles at $z/d = -5.2$ obtained by LDV (■) and hot wire anemometry (♦) for $0 \leq x/L \leq 0.29$.	82
36. Transverse velocity profiles at $z/d = -5.2$ obtained by LDV (■) and hot wire anemometry (♦) for $0.44 \leq x/L \leq 1.2$.	83
37. Transverse velocity profiles at $z/d = -2.6$ (■), -3.9 (Δ), and -5.2 (♦) obtained by LDV for $0.44 \leq x/L \leq 1.2$.	84
38. Axial turbulence intensity profiles at $z/d = -2.6$ obtained by LDV (■) and hot wire anemometry (♦) for $0 \leq x/L \leq 0.29$.	85
39. Axial turbulence intensity profiles at $z/d = -2.6$ obtained by LDV (■) and hot wire anemometry (♦) for $0.44 \leq x/L \leq 1.2$.	86
40. Axial turbulence intensity profiles at $z/d = -3.9$ obtained by LDV (■) and hot wire anemometry (♦) for $0 \leq x/L \leq 0.29$.	87
41. Axial turbulence intensity profiles at $z/d = -3.9$ obtained by LDV (■) and hot wire anemometry (♦) for $0.44 \leq x/L \leq 1.2$.	88
42. Axial turbulence intensity profiles at $z/d = -5.2$ obtained by LDV (■) and hot wire anemometry (♦) for $0 \leq x/L \leq 0.29$.	89

43. Axial turbulence intensity profiles at $z/d = -5.2$ obtained by LDV (▣) and hot wire anemometry (♦) for $0.44 \leq x/L \leq 1.2$.	90
44. Transverse turbulence intensity profiles at $z/d = -2.6$ obtained by LDV (▣) and hot wire anemometry (♦) for $0 \leq x/L \leq 0.29$.	91
45. Transverse turbulence intensity profiles at $z/d = -2.6$ obtained by LDV (▣) and hot wire anemometry (♦) for $0.44 \leq x/L \leq 1.2$.	92
46. Transverse turbulence intensity profiles at $z/d = -3.9$ obtained by LDV (▣) and hot wire anemometry (♦) for $0 \leq x/L \leq 0.29$.	93
47. Transverse turbulence intensity profiles at $z/d = -3.9$ obtained by LDV (▣) and hot wire anemometry (♦) for $0.44 \leq x/L \leq 1.2$.	94
48. Transverse turbulence intensity profiles at $z/d = -5.2$ obtained by LDV (▣) and hot wire anemometry (♦) for $0 \leq x/L \leq 0.29$.	95
49. Transverse turbulence intensity profiles at $z/d = -5.2$ obtained by LDV (▣) and hot wire anemometry (♦) for $0.44 \leq x/L \leq 1.2$.	96
50. Axial turbulence intensity profiles at $z/d = -2.6$ (▣), -3.9 (Δ), and -5.2 (♦) obtained by LDV for $0.44 \leq x/L \leq 1.2$.	97
51. Transverse turbulence intensity profiles at $z/d = -2.6$ (▣), -3.9 (Δ), and -5.2 (♦) obtained by LDV for $0.44 \leq x/L \leq 1.2$.	98
52. U-V Reynolds stress profiles at $z/d = -2.6$ obtained by LDV (▣) and hot wire anemometry (♦) for $0 \leq x/L \leq 0.29$.	99
53. U-V Reynolds stress profiles at $z/d = -2.6$ obtained by LDV (▣) and hot wire anemometry (♦) for $0.44 \leq x/L \leq 1.2$.	100
54. U-V Reynolds stress profiles at $z/d = -3.9$ obtained by LDV (▣) and hot wire anemometry (♦) for $0 \leq x/L \leq 0.29$.	101

55. U-V Reynolds stress profiles at $z/d = -3.9$ obtained by LDV (▣) and hot wire anemometry (♦) for $0.44 \leq x/L \leq 1.2$.	102
56. U-V Reynolds stress profiles at $z/d = -5.2$ obtained by LDV (▣) and hot wire anemometry (♦) for $0 \leq x/L \leq 0.29$.	103
57. U-V Reynolds stress profiles at $z/d = -5.2$ obtained by LDV (▣) and hot wire anemometry (♦) for $0.44 \leq x/L \leq 1.2$.	104
58. U-V Reynolds stress profiles at $z/d = -2.6$ (▣), -3.9 (Δ), and -5.2 (♦) obtained by LDV for $0.44 \leq x/L \leq 1.2$.	105
59. Vertical velocity profiles at $z/d = -2.6$ (♦) and -3.9 (◊) obtained by hot wire anemometry for $0.02 \leq x/L \leq 0.29$.	106
60. Vertical velocity profiles at $z/d = -2.6$ (♦) and -3.9 (◊) obtained by hot wire anemometry for $0.44 \leq x/L \leq 1.2$.	107
61. Vertical turbulence intensity profiles at $z/d = -2.6$ (♦) and -3.9 (◊) obtained by hot wire anemometry for $0.02 \leq x/L \leq 0.29$.	108
62. Vertical turbulence intensity profiles at $z/d = -2.6$ (♦) and -3.9 (◊) obtained by hot wire anemometry for $0.44 \leq x/L \leq 1.2$.	109
63. U-W Reynolds stress profiles at $z/d = -2.6$ (♦) and -3.9 (◊) obtained by hot wire anemometry for $0.02 \leq x/L \leq 0.29$.	110
64. U-W Reynolds stress profiles at $z/d = -2.6$ (♦) and -3.9 (◊) obtained by hot wire anemometry for $0.44 \leq x/L \leq 1.2$.	111
65. Axial velocity profile at mixing chamber exit for $z/d=-5.2$ and the cubic spline fit used in the ejector thrust calculation.	112

Nomenclature

b	Jet width
C, D	Kings law coefficients
d	Nozzle width
E	Hot wire output
f	Frequency of pulsations
H	Mixing chamber width
K	Calibration constant for LDV
L	Mixing chamber length
N	Number of samples per point
p	Static pressure
q	Dynamic pressure
R	Universal gas constant
Re	Reynolds number
S	Mixing chamber vertical height
T	Calculated thrust
u, U	Velocity component in the axial direction
$\langle U \rangle$	Volume average velocity
U'	r.m.s value of the axial velocity fluctuation
$\overline{u'v'}, \overline{u'w'}$	Reynolds stress correlations
v	Velocity component in the transverse direction
V'	r.m.s value of the transverse velocity fluctuation
w	Velocity component in the vertical direction
W'	r.m.s value of the vertical velocity fluctuation

X	Primary nozzle location
x	Axial location measured from the nozzle exit
y	Transverse location measured from the nozzle centerline
z	Vertical location measured from the channel centerline
z_c	Confidence coefficient
λ	Wavelength of light
θ	Included angle between laser beams
ρ	Density of air
ω	Weighting function for bias correction
ξ	Downstream distance from mixing chamber entrance

Superscripts and Subscripts

amb	Ambient conditions
b	Blue laser beam pair
c	Centerline value
cal	Calibration value
e	Primary jet exit conditions
ej	Ejector value
g	Green laser beam pair
n	Isolated primary nozzles
o	Stagnation conditions
-	Mean value
'	Fluctuation from the mean

ABSTRACT

AN EXPERIMENTAL STUDY OF A THREE-DIMENSIONAL THRUST AUGMENTING EJECTOR USING LASER DOPPLER VELOCIMETRY

Bruce Lowell Storms

Flow field measurements have been obtained in a three-dimensional thrust augmenting ejector using laser Doppler velocimetry and hot wire anemometry. The primary nozzle, segmented into twelve slots of aspect ratio 3.0, was tested at a pressure ratio of 1.15. Results are presented on the mean velocity, turbulence intensity, and Reynolds stress progressions in the mixing chamber of the constant area ejector. The segmented nozzle was found to produce streamwise vortices that may increase the mixing efficiency of the ejector flow field. Compared to free jet results, the jet development is reduced by the presence of the ejector walls. The resulting thrust augmentation ratio of this ejector was also calculated to be 1.34.

CHAPTER 1

Introduction

Ejectors are currently being considered for use in vertical or short takeoff and landing (V/STOL) aircraft¹. By diverting the main jet through a thrust augmenting ejector, it is possible to obtain the additional thrust required for V/STOL activities. Large-scale tests funded by NASA-Ames involve the so-called chordwise ejectors (fuselage and short diffuser) of Fig. 1(a) and 1(b). The spanwise ejector of Fig. 1(c) is another configuration, suitable for STOL activities, that is being studied by Rockwell. A number of problems must still be solved before the ejector concept may be fully implemented². High performance aircraft, for example, cannot accommodate the long chambers required for complete mixing of the ejector flow. Thus, it is desired to optimize the ejector design to increase the turbulent mixing.

The thrust augmentation of an ejector is associated with the entrainment of surrounding atmosphere by the primary jet flow and the subsequent mixing of this entrained air with the primary jet³. Additional thrust results from the low pressure on the shroud entrance region caused by the entrainment of the secondary flow. Pressure recovery is then attained by the turbulent mixing of the primary and secondary flows. A diffuser is often incorporated to further increase the thrust augmentation by reducing the inlet pressure. Since the thrust augmentation increases with more

efficient mixing of the primary and secondary flows, many recent studies have focused on the fluid mechanics of this process.

Recent Ejector Research

Two-dimensional Ejectors

One of the most recent experimental studies of ejectors was done by Bernal and Sarohia⁴ in 1984. The primary jet was a slot-type two-dimensional nozzle that measured 0.8 cm by 50.8 cm. The two shroud geometries that were studied were the constant area and diffused flow ejectors of which the former is most relevant to the present study. The constant area ejector had a length-to-width ratio of 3.0 with the primary nozzle displaced one channel width in front of the inlet plane. The ejector was operated with no onset flow at a Reynolds number based on nozzle width of 8.5×10^4 . Measurements of the flow field were made with a two component laser Doppler velocimeter (LDV) in forward scatter with an expected accuracy of $\pm 2\%$ for the velocity components and turbulence intensities. The expected accuracy in the Reynolds stress, however, was as high as $\pm 10\%$.

Axial velocity, turbulence intensity, and Reynolds stress profiles are shown in Fig. 2-5. It was determined that the lateral momentum transport is related to the Reynolds stress profiles of Fig. 5. At the centerline, a positive derivative of the Reynolds stress with respect to y indicates a reduction of the momentum with downstream distance while a negative derivative away from the centerline indicates a increase in the downstream momentum. The flow field

measurements identified three flow regions in the ejector as shown in Fig. 6. The entrance region, $x < 2.5H$ (H = ejector width), is characterized by a lack of interaction between the ejector wall and primary jet. The interaction region, $2.5H < x < 6.25H$, is characterized by positive interaction between the wall and primary jet resulting in pressure recovery and an increase in fluid momentum near the wall with downstream distance. The "pipe" flow region, $x > 6.25H$, is characterized by increased skin friction with little improvement in the uniformity of the velocity profile. A maximum thrust augmentation ratio (ratio of ejector thrust to primary jet thrust) of 1.23 was obtained from this configuration at a primary pressure ratio of 1.94.

A 1987 publication by Lund, Tavella, and Roberts⁵ reports the results of a computational study of two-dimensional ejectors based on a viscous-inviscid approach. This approach divides the ejector into two regions shown in Fig. 6 to minimize computational effort. The first region is not affected by viscous or turbulent stresses while the second region contains significant fluid shear. The predictions of the viscous-inviscid algorithm were compared with the measurements of Ref. 4. Comparison of computed and measured velocity profiles indicated that the algorithm accurately predicted jet spreading as well as the decay of the maximum velocity. The computed thrust augmentation ratio of 1.26, marginally higher than the experimental value of 1.23, also validated the results of the computation. Many parametric variations were then computed to determine optimum ejector performance. As a result, it was determined that a higher performance is achieved by increasing the ejector length up to a

length-to-width ratio of approximately seven where skin friction becomes significant. The optimum longitudinal nozzle position was also determined to be at the ejector inlet plane.

In 1983, Alperin and Wu⁶ noted that the analytical study of compressible flow in a constant area ejector yields two solutions. Furthermore, these solutions were found to be related by the normal shock relations. The first solution always results in subsonic mixed flow at the exit of the ejector while the second always yields supersonic mixed flow. To obtain a second solution thrust augmenting ejector, the secondary flow at the start of mixing must be transonic or supersonic. As a result, good performance may be obtained at supersonic flight speeds with relatively simple inlet geometries⁷. First solution ejectors, however, experience high losses with increased freestream velocity unless the inlet geometry is optimized for that flight regime. If the second solution ejector can be demonstrated experimentally, forward propulsion will be another practical application of the ejector concept.

Other Nozzle Configurations

Because the thrust augmentation is a function of the mixing efficiency, numerous analytical and empirical studies have been performed with various primary nozzle geometries. One example is the computational study of the "hypermixing" nozzle by Bevilaqua⁸ in 1976. The nozzle exit was divided into several segments with a length-to-width ratio of 8.0. The flow from each segment was alternately given an upward or downward velocity component so that it exhausted at a 15° angle from the jet axis as shown in Fig. 7. This

nozzle configuration created streamwise vortices that increased the turbulent mixing in the ejector. With an inlet area ratio of approximately 24.5, the exhaust flow was fully mixed within five channel widths and an thrust augmentation ratio in excess of 2.0 was obtained. However, reductions in ejector length resulted in significant performance losses. It was determined that the ejector length may be reduced with no loss of thrust augmentation by increasing the aspect ratio of the hypermixing nozzle segments. It was also noted that there is an optimum ejector length for every given nozzle geometry. If the ejector is shorter than the optimum, incomplete mixing reduces the thrust augmentation. If the ejector is too long, the augmentation is reduced by increased wall friction.

In 1978, Mefferd and Bevilaqua⁹ combined the hypermixing nozzle with a "cross slot" nozzle in a computer analysis of a variety of geometries. The cross slot nozzle is divided into many thin elements which are cut back to form a wedge as shown in Fig. 8. This configuration produces a pair of counter-rotating vortices at the end of each jet segment which aids in turbulent mixing and provides approximately the same increase in entrainment as the hypermixing nozzle. The baseline thrust augmentation ratio for the hypermixing and cross slot nozzles alone were calculated to be 1.37 and 1.34, respectively. The computed results indicated that the hypermixing and cross slot mechanisms are not readily combined since this combination reduced the ejector entrainment. Experimental thrust and flow field measurements of a selected configuration supported this conclusion.

In an attempt to further increase thrust augmentation, Bernal, Sarohia, and Bui studied the entrainment of pulsatile ejector flows¹⁰. The flow entering the nozzle plenum was modulated from frequencies of 20 to 1500 Hz by passing the flow through a pneumatic transducer. The jet growth, shown in Fig. 9, was found to be significantly increased with pulsations and a 10 to 15% gain in ejector thrust was obtained over the steady-state performance. Except for very low Strouhal numbers, $fd/U_e < 0.05$, this increase in performance was independent of frequency of pulsations and proportional to its amplitude.

LDV Measurements

Recent LDV measurements were obtained in 1987 by Driver¹¹. A turbulent boundary layer study was made using a three-component, three-color LDV system in forward scatter. The experimental uncertainties for this configuration were $\pm 2\%$ in the mean velocity components, $\pm 7\%$ in the turbulence intensities, and -7% to $+20\%$ in the Reynolds stresses. The uncertainty in the Reynolds stresses reflects the belief that the measured values are 10-20% lower than the actual values as a result of multiple seed particle measurements (ie. more than one particle passing through the measurement volume at one time).

A 1985 publication detailed the LDV measurements in turbulent jets that were obtained by Ramaprian¹². A two-component TSI system was employed in forward scatter using polarization separation to identify the individual velocity components. The experimental uncertainties in velocity, turbulence intensity, and Reynolds stress

were found to be $\pm 1\%$, $\pm 5\%$, and $\pm 10\%$, respectively. The mean properties of the jet were shown to agree with existing data while the turbulent velocities and fluxes, as measured by the LDV, were found to be lower than the hot-wire measurements by as much as 15-25%. The reason for these discrepancies has yet to be determined.

Another study by Nakayama¹³ employed laser Doppler velocimetry to obtain measurements in the wake of an airfoil. A two-color dual beam TSI system was used in this study and hot wire measurements were also obtained as a means of validation. A comparison with the hot wire data showed good agreement in the mean velocity and shear stress profiles while deviations were noticeable in the measured turbulence intensities. Although no quantitative analysis was presented, it was noted that the LDV turbulence intensity data tend to be high due to noise in the signal while the hot-wire measurements were low due to spatial and temporal averaging.

A relevant publication by McLaughlin and Tiederman¹⁴ addressed the statistical bias of one-component LDV measurements in turbulent flows. Biased statistics occur because a larger than average volume of fluid passes through the probe volume during periods when the velocity is faster than the mean and, similarly, a smaller than average volume passes through the probe volume at slower than average velocities. Since the seeding is assumed to be uniformly distributed in the flow, the probability of measuring a velocity larger than the mean is greater than measuring a velocity slower than the mean. Consequently, the measured velocity is biased toward the faster end of the velocity range. In computing the true mean velocity and

turbulence intensity, it is necessary to weight each measurement with the inverse of the magnitude of the velocity vector as follows:

$$\bar{u} = \frac{\sum_{i=1}^N \omega_i u_i}{\sum_{i=1}^N \omega_i}$$

$$\sqrt{u'^2} = \left[\frac{\sum_{i=1}^N \omega_i (u_i - \bar{u})^2}{\sum_{i=1}^N \omega_i} \right]^{1/2}$$

where the weighting function is defined as

$$\omega_i = (u_i^2 + v_i^2 + w_i^2)^{-1/2}$$

For this computation, however, all three components of velocity are required. A simplified biasing correction is introduced using a weighting function based on the x component of velocity alone. It is demonstrated that for turbulence intensities less than 15%, the mean of the biased distribution is less than 2% high. For turbulence levels up to 35%, the one-dimensional correction is shown to provide reasonable accuracy with less than 2% error. It is noted that statistical biasing produces greater error in the turbulence measurements than it does in the mean measurements. However, the biased measurements are still within 2% of the actual values for turbulence levels less than 10%. Also, if the seed is not uniformly distributed, as with mixing flows, statistical biasing of the velocity measurements may be even higher.

In another publication on two-component LDV measurements, Orloff and Olson¹⁵ applied a biasing correction to their data using the weighting function given by

$$\omega_i = (u_i^2 + v_i^2)^{-1/2}$$

for the i^{th} pair of velocity measurements. The weighted averages were then computed from

$$\begin{aligned}\bar{u} &= \sum_{i=1}^N \omega_i u_i / S & \overline{u'^2} &= \sum_{i=1}^N \omega_i (u_i - \bar{u})^2 / S \\ \bar{v} &= \sum_{i=1}^N \omega_i v_i / S & \overline{v'^2} &= \sum_{i=1}^N \omega_i (v_i - \bar{v})^2 / S \\ \overline{u'v'} &= \sum_{i=1}^N \omega_i (u_i - \bar{u})(v_i - \bar{v}) / S\end{aligned}$$

where

$$S = \sum_{i=1}^N \omega_i$$

Although the resulting corrections of the mean velocities were 1.5% or less, the errors in the calculated components of the Reynolds stress tensor were significant. The correction to the squares of the turbulence intensities were as high as 3.4% which compounded into a 7.3% error in the Reynolds stress.

Current Research

The current research is the study of an ejector flow field using both laser Doppler velocimetry and hot wire anemometry. The LDV system can simultaneously measure two components of velocity, the corresponding turbulence intensities, and the Reynolds stress. Although LDV measurements have been made previously in ejector flow fields, the geometry of the NASA ejector facility is unique and yields a three-dimensional flow that has yet to be investigated. The only previous data obtained from this configuration were thrust measurements at JPL which have yet to be published. The

experimental research involves a static ejector test with a primary pressure ratio of approximately 1.1 in which the secondary air is drawn in from the lab facility. The objective of this research is to follow the evolution of the velocity profiles in the ejector mixing chamber. The resulting flow field measurements will supply the boundary conditions and a means of validation for a Navier-Stokes code. This research also serves as a low speed test of the ejector facility. Eventually, the ejector will operate with primary and secondary pressure ratios of 9.0 and 3.5, respectively, in an attempt to demonstrate the existence of the second solution.

CHAPTER 2

Experimental System

Ejector Model

The ejector model was built under contract with NASA-Ames at JPL in Pasadena, California. After limited testing, the research was cancelled due to a change in direction of JPL research and the ejector model was then transported to NASA-Ames.

A sketch of the model is shown in Fig. 10 and the relevant dimensions are listed in Table 1 on page 39. The mixing chamber has an inlet radius of 95 mm and an adjustable diffuser at the exit. For the current study, the diffuser angle was set to zero yielding a constant area configuration with a length-to-width ratio of 4.8. The primary nozzle is segmented into twelve slots of aspect ratio 3.0 as shown in Fig. 11. The nozzle angle and longitudinal position can be varied through the adjustment of two concentric rings. For the present study, the nozzle was aligned with the mixing chamber centerline and the nozzle exit was located 0.85 channel widths downstream of the ejector inlet. Optical access for LDV measurements is provided by glass windows on the upper and lower surfaces of the mixing chamber.

A plumbing schematic for the primary air supply is presented in Fig. 12. The primary air for the nozzles was supplied by a compressor at a pressure of 100 psig. Because oil deposits on the windows of the mixing chamber were interfering with LDV measurements, it was necessary to install an after-cooler and a dry

air filter to obtain clean air. An in-line regulator was incorporated to produce a primary pressure ratio of 1.15 and to remove any fluctuations created by the compressor. The resultant pressure, measured at 10 Hz over a five minute period, had a standard deviation of no more than 4%. The selected pressure ratio yielded a jet exit velocity of approximately 150 m/s ($Re_d = 2.4 \times 10^4$) which is a limit imposed by the optics and electronics of the LDV system.

Since the model was initially designed to demonstrate the second solution, the ejector may be supplied with both primary and secondary air to simulate forward flight. For the current static test, the secondary air plenum was left open to the atmosphere so that air could be drawn in freely through the vertical perforated pipe shown in Fig. 13. The area of the secondary air plenum is approximately 20 times the ejector inlet area. In addition, a perforated plate is located upstream of the mixing chamber to reduce the turbulence of the secondary flow.

Horizontal positioning of the LDV and hot wire probes was made possible by a two axis traverse table. An accuracy of $\pm 25 \mu\text{m}$ was obtained using optical encoders to measure shaft rotation. Ten axial traverse positions were chosen using the following equation which includes one survey downstream of the mixing chamber exit:

$$1 - \cos \frac{n\pi}{16} \quad n = 0, 1, \dots, 9$$

This selection provides for a more detailed study near the jet exit where the flow is changing most rapidly. Transverse measurements were separated by 2.5 mm except near the nozzle exit where more detail was desired.

Vertical positioning in 3.2 mm increments was accomplished by elevating the probe holder with aluminum shim stock. This increment was chosen because it is approximately equal to the spatial resolution of the LDV system. Flow field measurements were obtained at three vertical locations: $z/d = -2.6$, -3.9 , and -5.2 where d is the nozzle width. The locations relative to the nozzle are shown in Fig. 14. Note that these vertical locations were a compromise to optimize the efficiency of both the transmitting and receiving optics.

Laser Doppler Velocimeter

Optical System

The flow field measurements were obtained with a two-component fiberoptic laser Doppler velocimeter made by TSI. A Spectra-Physics model 165 argon-ion laser with a maximum output of four watts was used as the light source. The color separator layout, shown in Fig. 15, yields the 514.5 nm and 488 nm beam pairs (green and blue, respectively) employed to measure two velocity components. The laser beam is first split into two equal intensity beams, one of which is then shifted by 40 MHz by the Bragg cell. This shift serves to eliminate directional ambiguity in the signal since the resultant Doppler frequency will now be centered around 40 MHz instead of zero. The two beams then pass through polarization rotators to obtain the identical polarization necessary for efficient light wave interference. Two dispersion prisms separate the green and blue lines which are then guided with mirrors to the fiber coupling optics. Each beam passes through a translator and focusing

lens which can be adjusted for optimum coupling to the polarization preserving fibers.

Thirty meters of fiber connect the color separating optics to an optical probe which may be located remotely. This probe contains both the focusing and the receiving optics for light collection in the backscatter configuration as shown in Fig. 16. Small collimating lenses within the probe reproduce the laser beams which then pass through a 500 mm focal length lens. Focussed to a point, the four beams create the measurement volume which was empirically determine to be an ellipsoid with a length and width of 3.80 mm and 0.20 mm, respectively. The optimum laser power for data acquisition was determined to be 700 mW. At this setting, the power of the green and blue laser beams were respectively 40 mW and 20 mW per beam. The receiving optics, a combination of the transmitting and receiving lenses, focus the scattered light onto the receiving fiber which returns to the location of the color separator and laser. The green and blue lines, separated by a dichroic mirror, then enter photomultiplier tubes which convert the light to an analog signal.

To obtain a higher signal-to-noise ratio, the system was also modified for forward scatter light collection as shown in Fig. 17. Two lenses, with focal lengths of 250 and 350 mm, were employed 10° off-axis to focus the scattered light onto a multimode fiber compatible with the optics of the backscatter system. An analysis of the LDV performance in the forward and backscatter configurations is presented in Appendix B.

The velocity component measured and associated calibration constant for each beam pair are determined by the geometry of the transmitting optics. The interference of two laser beams creates fringes of light so that the only component of velocity measured is perpendicular to the probe axis in the plane of the beams as shown in Fig. 18. The Doppler calibration constant which relates the frequency of the scattered light to the particle velocity is given by the equation

$$K = \frac{\lambda}{2 \sin(\theta / 2)}$$

where λ is the light wavelength and θ is the included angle of 5.28° . The constants for the green and blue beam pairs are $K_g = 5.5831 \text{ (m/sec)(MHz)}^{-1}$ and $K_b = 5.2955 \text{ (m/sec)(MHz)}^{-1}$, respectively. These constants were also determined experimentally with a spinning wire and were found to agree within 1%. The probe was positioned to measure the velocity components at $\pm 45^\circ$ from the ejector axis in order to increase the highest measurable axial velocity of the system.

The LDV geometry described above could be used to measure the velocity field only at distances from the shroud wall where a measurement volume was allowed to form. Closer to the wall, one of the green and blue beams was blocked since the beams entered the mixing chamber at an angle of 2.64° from vertical. The distance from the shroud wall where measurements were possible was a function of the depth into the channel of the desired survey. For the three vertical locations considered, this distance was approximately 2 mm.

For the same reason, measurements were also impossible in the immediate vicinity of the nozzle.

Flow Seeding Device

In order to measure the velocity with any LDV system, it is necessary to seed the flow with particles. The particles must be large enough to provide adequate light scattering, but small enough to follow the flow.

An effective seeding method was determined to be the seeding of only the secondary flow with mineral oil. The seeding device was relatively simple as it consisted of a jet of air impinging on the surface of the mineral oil in a sealed bottle as shown in Fig. 19. The seeded air leaving the bottle contained oil particles of approximately 3-5 μm in diameter, a reasonable size for light scattering in this LDV system. The secondary flow was seeded in the plenum through the perforated pipe. The boundary layer along the glass surfaces prevented the rapid deposit of oil so that LDV measurements could be obtained for over 30 minutes before the glass required cleaning. The coincident data rate ranged from 40 to 80 samples per second except near the centerline close to the nozzle exit ($|y/H| < 0.05$ and $x/L < 0.2$). Since the flow is not well mixed in this region, typical data rates ranged from 5 to 25 samples per second.

Signal Processors and Data Acquisition

The velocity measurement can only be obtained after sufficient signal processing of the photomultiplier tube output. Two Macrodyne model 3001 counter processors were used for this

purpose, one for each measured velocity component. The counter processors incorporate both high and low-pass filters. The low-pass filters served to remove the high frequency noise while the high-pass filters were used primarily for pedestal removal. Here, the pedestal refers to the flux of light scattered by each beam individually which appears in addition to the Doppler frequency. The high and low-pass filters were typically set to 8 MHz and 16 MHz, respectively, to create an 8 MHz bandwidth. Two programmable signal sources were utilized to downmix the actual Doppler frequency to the mid-frequency of 12 MHz. Level detectors within the counter processors determined the presence of a Doppler burst created by a particle within the measurement volume. The Doppler frequency was then determined from the time required for eight cycles in the burst. The measured frequency output by the counter processor was in digital form.

A coincidence interface served to inhibit the output of the counter processors until the data passed a coincidence test. This test initiated a time window of 50 μ sec when a burst was detected by one of the counter processors. If the second processor did not detect a burst by the end of the time window, the data from the first processor was discarded and a new time window was initiated. If the data from both processors was received within the window, the coincidence interface allowed the transfer of data to a HP model 6942A Multi-Programmer which was used as a memory buffer.

The data acquisition by the Multi-Programmer was controlled by a HP 3000 minicomputer system. Once 1024 coincident samples of the velocity had been obtained, the data was transferred to the

minicomputer for data reduction. The data was stored on a floppy disk for further analysis at a later date. The number of samples taken was a compromise designed to minimize the uncertainty of the results while maintaining a reasonable total time of the experiment.

The first step in data reduction was to convert the measured Doppler frequencies to velocities using the corresponding calibration constant. Since the LDV measured the velocity components at $\pm 45^\circ$ with respect to the ejector axis, the following simple transformations yield the axial and transverse velocity components:

$$u = U_G \cos 45^\circ + U_B \cos 45^\circ$$

$$v = U_G \sin 45^\circ - U_B \sin 45^\circ$$

where U_G and U_B refer to the velocities measured by the green and blue beam pairs, respectively.

Hot Wire Anemometry

Measurements of the mean and fluctuating velocity components were also obtained with X-wire constant temperature anemometry. The probes were DISA type 55P51 (platinum-coated tungsten) which are nominally $\pm 45^\circ$ to the probe axis. DISA type 55M01 constant temperature anemometers with a standard bridge were used with a 1.5 overheat ratio. Large signal amplifiers followed by sample and hold amplifiers permitted simultaneous sampling of both hot wire channels. As with the LDV measurements, 1024 samples were obtained at each location.

Velocity calibration was accomplished by aligning the probe with a jet issuing from a DISA calibrating nozzle and measuring the wire output, E , for approximately ten values of the calibration velocity,

U_{cal} . The Kings Law coefficients were then determined by a least squares fit of the data to:

$$E^2 = C + D [U_{cal}]^{1/2}$$

An angle calibration was obtained using the same calibration nozzle at the maximum calibration velocity. The wire output was measured for successive angles from the nozzle axis of $-40^\circ, -35^\circ, \dots, +40^\circ$. The measured data was then fit to linear functions of the form:

$$\begin{aligned} u &= a_{11} W_1 + a_{12} W_2 & W_1 &= \left[\frac{E_1^2 - C_1}{D_1} \right]^2 \\ v(\text{or } w) &= a_{21} W_1 + a_{22} W_2 & W_2 &= \left[\frac{E_2^2 - C_2}{D_2} \right]^2 \end{aligned}$$

Here, the single subscripts refer to the respective wire. The values of a_{ij} were then used to resolve the velocity components of the ejector measurements. The calibrations were repeated each day before and after data acquisition. Since the laboratory room temperature varied by no more than $\pm 2^\circ\text{C}$, the calibration constants were found to vary a maximum of 3%.

The hot wire survey locations were chosen to coincide with the LDV measurements. However, no measurements were possible within 3.8 mm of the mixing chamber wall due to the size of the probe holder. At $z/d = -2.6$ and -3.9 , surveys were obtained at every axial location except at the nozzle exit, $x/L = 0$, where the probe would have contacted the nozzle. The vertical velocity component was also obtained at these locations by rotating the probe 90° about its axis. At $z/d = -5.2$, the current experimental setup only permitted surveys between $x/L = 0.29$ and $x/L = 1.0$.

Data Processing

The data obtained from this test was processed by the same computer that was used for data acquisition. For initial review, a one page print out was produced for each data point with the results of the velocity calculations and computer generated histograms (Fig. 20). The time averaged velocities, turbulence intensities, and Reynolds stress were computed using the following standard relationships:

$$\begin{aligned}\bar{u} &= \sum_{i=1}^N u_i / N & \sqrt{u'^2} &= \left[\sum_{i=1}^N (u_i - \bar{u})^2 / N \right]^{1/2} \\ \bar{v} &= \sum_{i=1}^N v_i / N & \sqrt{v'^2} &= \left[\sum_{i=1}^N (v_i - \bar{v})^2 / N \right]^{1/2} \\ \overline{u'v'} &= \sum_{i=1}^N (u_i - \bar{u})(v_i - \bar{v}) / N\end{aligned}$$

where N is the number of samples. In all measurements of this experiment, the number of samples per data point was 1024.

For a large number of samples, the statistical uncertainties¹⁶ in the mean velocity, turbulence intensity and Reynolds stress can be written as

$$\begin{aligned}\bar{u} \pm z_c \frac{\sqrt{u'^2}}{\sqrt{N}} & \quad \sqrt{u'^2} \pm z_c \frac{\sqrt{u'^2}}{\sqrt{2N}} \\ \bar{v} \pm z_c \frac{\sqrt{v'^2}}{\sqrt{N}} & \quad \sqrt{v'^2} \pm z_c \frac{\sqrt{v'^2}}{\sqrt{2N}} \\ \overline{u'v'} \pm z_c \overline{u'v'} \sqrt{2/N}\end{aligned}$$

where z_c is the confidence coefficient. A 95% confidence level that the statistical uncertainty is less than the value computed from the corresponding equation is obtained by setting $z_c = 1.96$.

Other Instrumentation

The ejector was instrumented with two 25 psid pressure transducers. One was employed to measure the lower nozzle total pressure relative to the static pressure at the nozzle exit. The second transducer measured the static pressure at the nozzle exit relative to ambient. A J-type thermocouple was also installed to measure the total temperature in the nozzle. From this information, it was possible to compute the jet exit velocity using Bernoulli's principle:

$$U_e = \sqrt{2(p_o - p_e) / \rho_e}$$
$$\text{where } \rho_e = \frac{P_e}{RT_e}$$

A third 1 psid pressure transducer was used to measure the static pressure at the exit of the mixing chamber.

CHAPTER 3

Results and Discussion

Flow Field Measurements

The axial and transverse velocity components (u and v) were obtained using both laser Doppler velocimetry and hot wire anemometry. LDV surveys were obtained at ten axial locations for three vertical stations. Most of the LDV surveys were repeated with hot wire anemometry. A summary of the survey locations and corresponding measurement types is presented in Table 2 on page 39.

Because of the model configuration, LDV measurements of the vertical velocity were not possible. Therefore, the vertical velocity component was measured using hot wire anemometry only. The measurement stations include the nine downstream axial locations listed in Table 2 at two of the vertical stations ($z/d=-2.6$ and -3.9).

The ensuing discussion examines the characteristics of the velocity, turbulence intensity, and Reynolds stress profiles for the three measured velocity components. The possible errors and estimated uncertainty are addressed in the final section of the flow field discussion.

Axial and Transverse Velocity Measurements

Mean velocities. The progression of the axial mean velocity in the mixing chamber at $z/d=-2.6$ is shown in Fig. 21-22. Because each velocity profile is normalized by the local centerline velocity, the

expected centerline velocity decay is not observed. However, the centerline velocities of the LDV measurements that are listed on the graphs do follow the expected trend. Note that the axial velocity profile at $x/L=0.0$ was normalized by a calculated jet exit velocity since no centerline measurement was possible due to the obstruction of the laser beams. The calculation of the jet exit velocity is discussed in detail later.

The development of the axial velocity profiles is representative of typical jet flows. Near the nozzle exit at $x/L \leq 0.29$, the high velocity jet is surrounded by the low velocity entrained flow. As the primary jet mixes with the secondary flow, the jet spreads laterally and encompasses the entire channel by $x/L=0.62$. As mixing continues, the axial velocity profiles become more uniform.

The axial velocity progressions at $z/d=-3.9$ and -5.2 are presented in Fig. 23-24 and Fig. 25-26, respectively. A comparison of the axial velocity profiles at the three vertical locations reveals the three-dimensionality of the flow field. Although the axial velocity progressions at $z/d=-2.6$ and -5.2 are almost identical, significant differences are evident between these two stations and the velocity profiles at $z/d=-3.9$. Because of a lower centerline velocity at $z/d=-3.9$, the normalized secondary flow velocity is significantly higher for $0.02 \leq x/L \leq 0.29$ in Fig. 23. A plot of the axial velocity profiles at $x/L=0.02$ for all three vertical stations is shown in Fig. 27. These profiles, normalized by the jet exit velocity, clearly indicate that the axial centerline velocity in the blocked region of the nozzle is significantly lower than the velocity in the potential core of the jet. However, when the LDV axial velocity profiles at each vertical

location are plotted together for $x/L \geq 0.44$ as in Fig. 28, it is evident that the flow further downstream becomes essentially two-dimensional.

The centerline velocity results are presented in Fig. 29 along with free jet data from Ref. 4. Here, the measured centerline velocities are normalized by the calculated jet exit velocities. A sample calculation by the isentropic expansion of the nozzle total pressure is included in Appendix A. Since the nozzle total pressure was measured just upstream of the nozzle plenum, this calculation neglects in flow turning and nozzle exit losses. From the LDV and hot wire measurements at $x/L=0.02$, it was observed that the axial velocity was, on average, 90% of the jet exit velocity. However, previous jet data indicates that this location ($x/d=1.45$) is still within the potential core and there should be no jet velocity decay until $x/d=5.2^{19}$. The highest centerline to jet exit velocity ratio of 0.938 was chosen as a conservative correction to account for the total pressure losses in the primary nozzle. These corrected jet exit velocities for the LDV and hot wire measurements are included for reference purposes in Tables 3-5 on pages 40-42.

The centerline velocity results close to the nozzle exit ($x/L \leq 0.29$) clearly illustrate the three-dimensional effects of the nozzle geometry. Note that the abnormal velocity progressions at $z/d=-3.9$ correspond to the blocked portion of the nozzle as shown in Fig. 15. In this region, the centerline velocity actually increases with downstream distance as the entrained flow mixes with the primary jet flow. Further downstream, the centerline velocity decay of the ejector follows the monotonic decay observed in free jets regardless

of vertical location. However, at any fixed location downstream of $x/d=30$, it is evident that the normalized centerline velocity of the ejector results is approximately 10% higher than the free jet data of Ref. 4. Since this effect was also noted in the ejector data of Ref. 4, the higher centerline velocities can most likely be attributed to the confining ejector walls.

The evolution of the normalized jet width is presented in Fig. 30 with free jet data from Ref. 4. The jet width b is defined as the distance between points where the velocity is one-half the local centerline velocity. Sufficiently far downstream, it is observed that the jet width increases linearly with downstream distance. A least square fit to the data yields

$$b/d = 0.144 \left(\frac{x - x_0}{d} \right) \pm 0.28$$

where $x_0/d=5.75$. The slope of this linear relationship was found to be 32% lower than that of a free jet. This again indicates that the presence of the confining ejector walls may effectively hinder the jet development.

The transverse velocity measurements at $z/d=-2.6$ are presented in Fig. 31-32. The curvature of the secondary flow created by the inlet geometry is evident in the velocity profiles for $x/L \leq 0.29$. Here, the transverse velocity component of the secondary flow is toward the mixing chamber centerline. Near the nozzle exit, $|y/H| \leq 0.10$, the perturbations in the transverse velocity profiles may also indicate three-dimensional flow structures. As the flow progresses downstream, the effects of jet spreading become evident. For

$x/L \geq 0.62$, the transverse velocity component is toward the ejector walls, the opposite direction of the flow in the entrance region.

The transverse velocity progressions at $z/d = -3.9$ and -5.2 are presented in Fig. 33-34 and Fig. 35-36, respectively. These velocity profiles are similar to those at $z/d = -2.6$ except for in the region of the blocked nozzle at $z/d = -3.9$ and $x/L \leq 0.29$ shown in Fig. 33. Due to the lower axial centerline velocity, the normalized secondary flow velocity in the transverse direction is again significantly higher than at the other vertical stations. When the transverse velocity profiles for $x/L \geq 0.29$ at all three vertical stations are plotted together as in Fig. 37, it is evident that the flow in the transverse direction becomes essentially two-dimensional downstream.

Turbulence Intensities. The axial turbulence intensity profiles at $z/d = -2.6$ presented in Fig. 38-39 show the highly turbulent jet surrounded by low turbulence entrained flow close to the nozzle exit. As the flow develops downstream, the spreading of the high turbulence region is comparable to the spreading of the axial velocity profiles. A local minimum, corresponding to the potential core of the jet, is observed at the centerline of the axial turbulence intensity profiles. This feature is also present in free jets¹⁷.

The axial turbulence intensity profiles at $z/d = -3.9$ and -5.2 are presented in Fig. 40-41 and Fig. 42-43, respectively. The turbulence intensity progression at $z/d = -5.2$ does not notably differ from that of $z/d = -2.6$. However, the significantly higher normalized turbulence levels in the profiles near the nozzle at $z/d = -3.9$ in Fig. 40 again show the effect of a low centerline velocity.

The transverse turbulence intensity profiles at $z/d=-2.6$ are presented in Fig. 44-45. These profiles are similar to the axial turbulence intensity profiles except that a local minimum is not as obvious. Other studies have presented some contradicting results as to whether or not one exists in a free jet^{17,18}. The transverse turbulence intensity progression at the two other vertical stations are presented in Fig. 46-49. The noted differences between the three vertical stations follow the same trend as in the axial turbulence intensity.

The downstream profiles for $x/L \geq 0.29$ at all three vertical stations for the axial and transverse turbulence intensities are presented in Fig. 50 and 51, respectively. Both of these progressions indicate that the turbulence intensity characteristics become primarily two-dimensional as the flow develops downstream.

Reynolds Stress. The Reynolds stress profiles for all three vertical stations presented in Fig. 52-57 exhibit the one-cycle wave behavior that is common to all jet flows. As the flow develops downstream, it is observed that the peaks of the Reynolds stress profile propagate toward the ejector walls. As noted in Ref. 4, the Reynolds stress profile is related to the lateral momentum transport. At the centerline, the positive derivative of the Reynolds stress with respect to y indicates a reduction of momentum with downstream distance. The negative derivative of the Reynolds stress away from the centerline conversely indicates an increase in the downstream momentum. The Reynolds stress profiles close to the nozzle exit at $z/d=-3.9$ again illustrate the effects of the low centerline velocity and

the downstream progressions at all three vertical stations shown in Fig. 58 appear to indicate two-dimensional flow for $x/L \geq 0.29$.

Vertical Velocity Measurements

Mean Velocity. The vertical velocity profiles at the two vertical measurement stations are presented together in Fig. 59-60. These profiles exhibit a one-cycle wave behavior with the velocity up on one side of the nozzle and down on the other. This indicates that vortices are shed from the nozzle structure. As the flow develops, the vortices expand and slow as their energy is dissipated. Since the normalized profiles are very similar at both vertical locations, it appears that the vertical velocity is proportional to the centerline axial velocity. From the velocity profiles at $x/L > 0.29$, it is also evident that these vortices persist downstream at a weaker but still measurable level.

Turbulence Intensity. The vertical turbulence intensity profiles at the two vertical stations are presented together in Fig. 61-62. These profiles are similar to the axial turbulence intensity profiles with a local centerline minimum evident at many of the survey locations at $z/d = -2.6$. The spreading rate of the high turbulence region is also comparable to the axial turbulence intensity profiles while the turbulence level is noticeably lower. From the turbulence intensity profiles for $x/L \leq 0.29$, it is evident that the turbulence intensity is not proportional to the axial centerline velocity as noted in the mean velocity profiles. Due to the lower axial centerline velocity at $z/d = -3.9$, the vertical turbulence intensity near the nozzle

exit at this station is considerably higher than that of the other vertical station.

Reynolds Stress. The U-W Reynolds stress profiles for both vertical stations are presented in Fig. 63-64. Although there is considerable scatter in the Reynolds stress profiles and there is no apparent correlation between the two vertical stations, a unique form is evident in the profiles at $z/d=-2.6$ for $x/L \leq 0.29$. Instead of the one-cycle wave observed in the axial-transverse correlation, the axial-vertical Reynolds stress profiles at $z/d=-2.6$ appear to consist of two cycles. The higher Reynolds stress level at $z/d=-3.9$ may again be attributed to the low axial centerline velocity. As the flow develops downstream, the Reynolds stress profiles flatten to small fluctuations about zero.

Error Analysis

A primary source of uncertainty between the LDV and hot wire measurements is the possible discrepancy in the position of the measurements. Although the traverse table provided positioning accuracy within 25 μm , the absolute location of the mixing chamber centerline was subject to error. This is most evident in the axial velocity profiles near the nozzle at $z/d=-2.6$ (Fig. 21) which suggests a lateral position error of approximately 0.5 mm in the hot wire data. Further downstream of the nozzle, the relative magnitude of the lateral position error was reduced as the size of the jet structures increased.

Since this flow field is three-dimensional near the nozzle exit, the vertical position of the measurements in this region is also important. Some of the differences between the LDV and hot wire centerline velocities may be attributed to the uncertainty in the vertical position of the probe volumes. Small errors in the vertical location are important because the vertical lengths of the LDV and hot wire probe volumes are on the same order as the blocked regions of the segmented primary nozzle. Thus, spatial averaging becomes significant near the nozzle exit. As a result, the velocity, turbulence intensity, and Reynolds stress profiles may show the effect of vertical position error since they are normalized by the centerline axial velocity. This error is most pronounced in the blocked region of the nozzle closest to the exit ($z/d=-3.9$ and $x/L=0.02$; Fig. 23, 33, 40, 46, and 54) where the normalized LDV data is significantly higher than hot wire due to a lower measured centerline velocity.

The resolution of the axial and transverse velocity components is another possible source of error. Both the LDV and hot wire velocity data were resolved from the measured velocities at $\pm 45^\circ$ to the nozzle axis. Typically, the confidence intervals (discussed previously) for the axial and transverse velocity measurements were approximately the same size. However, when related to the axial and transverse velocities, these intervals were on the order of 1% and 30%, respectively. As the difference between two large values, the relatively low transverse velocity is more sensitive to small errors in the measured velocity components.

The three-dimensional nature of this ejector flow field may also account for some of the scatter observed in the transverse velocity

profiles. The vortices noted in the vertical velocity profiles may have created perturbations in the transverse velocity. If there was some discrepancy between the vertical locations of the LDV and hot wire measurements, the transverse velocity profiles may not show good correlation near the nozzle centerline. In the secondary flow away from the centerline, better correlation would be expected. This appears to be the case in the transverse velocity profiles at $0.02 \leq x/L \leq 0.29$ in Fig. 31 and 33.

Other considerations concern the differences between the measurement techniques. Because the sampling period was, on average, three times longer for the LDV measurements, temporal averaging may have been significant. As a result, the fluctuations in the primary nozzle pressure could have created higher measured turbulence levels in the LDV measurements. The 4% measured fluctuation in the primary nozzle pressure corresponds to approximately a 2% fluctuation in the jet exit velocity. This fluctuation becomes significant near the nozzle exit where the LDV data rate dropped as low as ten samples per second. The generally higher turbulence levels of the LDV data compared with the hot wire data in Fig. 38-49 appear to support this hypothesis.

A source of error peculiar to laser Doppler velocimetry is the possibility of statistical velocity bias as discussed previously. A bias correction was not applied to this LDV data as the validity of such a correction is questionable in mixed flows. A basic assumption of all bias corrections is that the flow is uniformly seeded with particles, and, as noted previously, this was not the case in this experimental system. As noted in Ref. 12, the estimated uncertainties in the

velocities, turbulence intensities, and Reynolds stresses are on the order of $\pm 1\%$, $\pm 5\%$, and $\pm 10\%$, respectively. Thus, the significant differences between the LDV and hot wire measurements of the Reynolds stress profiles may be the result of statistical velocity bias.

Other variables inherent in LDV systems may also account for the differences between LDV and hot wire data. During the course of a survey, the optical surface may have become coated with oil, effectively reducing the signal-to-noise ratio. In addition, the seeding may not have been uniform on both sides of the nozzle. With the threshold of the level detectors set for low seeding on one side of the nozzle, some erroneous data may have been taken on the other side with higher seeding. Both of these uncertainties may account for the asymmetric nature of some of the LDV data.

Thrust Augmentation

A standard measure of ejector performance is the thrust augmentation ratio. This value is defined as the ratio of the ejector thrust to the isolated primary nozzle thrust. The ejector and primary nozzle thrust were calculated from the measured fluid momentum as follows. Sample calculations are presented in Appendix A.

The ejector thrust was calculated using a control volume that crossed the mixing chamber exit and extended to ambient conditions about the ejector. Since the static pressure at the mixing chamber exit was approximately equal to ambient, the ejector thrust was only a function of the fluid momentum at the mixing chamber exit. The momentum at the exit was determined from the integration of a cubic spline curve fit to the LDV data as shown in Fig.

65. As noted previously, the flow field is essentially two-dimensional at the mixing chamber exit. Therefore, the total fluid momentum was determined from the calculated momentum at one vertical station assuming two-dimensional flow and neglecting the three-dimensional edge effects created by the upper and lower surfaces.

The primary nozzle thrust was calculated from the fluid momentum at the nozzle exit assuming a uniform exit velocity profile. The nozzle exit velocity was determined from the isentropic expansion of the measured total pressure to the laboratory ambient pressure. The ambient static pressure, rather than ejector static, was used in this calculation since this would be the condition in a free jet thrust measurement. As discussed previously, this calculation does not account for flow turning and nozzle exit losses. Therefore, a correction to the exit velocity was incorporated into the primary nozzle thrust calculation presented in Appendix A.

The resultant thrust augmentation ratio was calculated to be 1.34. This value is 9% higher than the corresponding value of 1.23 obtained from the two-dimensional ejector in Ref. 4. Since it was noted that the thrust augmentation ratio was relatively independent of pressure ratio⁴, it is probable that some of the additional thrust augmentation of the current three-dimensional ejector is the result of the enhanced mixing created by the vortices present in this flow field.

Several geometric parameters may have also affected the thrust augmentation of the current ejector and the two-dimensional ejector of Ref. 4. The relevant geometric parameters that differ between the

two ejectors include ejector length, nozzle longitudinal position, and ejector inlet ratio. These are discussed in more detail below.

The length-to-width ratios of the current and reference ejectors are 4.8 and 3.0, respectively. In the computational study and experimental results of Ref. 5, the thrust augmentation ratio was found to increase with ejector length up to a length-to-width ratio of approximately seven. This prediction indicates that the current ejector performance may be expected to be as much as 10% higher than that of Ref. 4.

The longitudinal location of the primary nozzle also differs between the current and reference ejectors. The two-dimensional nozzle of Ref. 4 was placed one channel width upstream of the ejector inlet while the experimental three-dimensional nozzle was located 0.85 channel widths downstream of the inlet. As noted in Ref. 5, the optimum placement of the primary nozzle is at the inlet plane of the mixing chamber. Thus, both ejectors were operating in less than optimum configurations with an estimated thrust reduction of approximately 7% each⁵.

The secondary-to-primary inlet area ratios of the current three-dimensional ejector and two-dimensional ejector of Ref. 4 are 20.0 and 12.4, respectively. As the inlet area ratio approaches unity and infinity, it is noted that the ejector reduces to the trivial case of a free jet with a thrust augmentation ratio of one. Thus, there is some optimum inlet area ratio which is also a function of ejector length⁵. A parametric study for the optimization of the inlet area ratio was not available and, therefore, the effect of this variable is unknown.

The construction of the secondary air plenum in the current ejector study also warrants analysis. As previously noted, the secondary air passes through a screen upstream of the mixing chamber entrance. The pressure drop created by this screen may have reduced the secondary air entrainment and possibly the thrust augmentation of the ejector in the current study. However, no pressure measurements were obtained in the secondary air plenum and, therefore, no quantitative analysis was possible.

CHAPTER 4

Conclusions

1. The segmented primary nozzle configuration creates vortices that persist downstream in the mixing chamber. These vortices may contribute to the mixing efficiency of the ejector flow field.

2. The axial and transverse flow field measurements near the nozzle exit also show the three-dimensional effects of the primary nozzle geometry. However, the velocity, turbulence intensity, and Reynolds stress profiles further downstream ($x/L \geq 0.44$) are independent of vertical position and indicate a primarily two-dimensional flow field.

3. Reasonable correlation was found between the LDV and hot wire measurements. The notable differences in the measurements near the centerline close to the nozzle exit are probably the result of discrepancies in vertical position between the two surveys. The LDV measurements of the velocity, turbulence intensity, and Reynolds stress may also include errors due to statistical velocity bias on the order of $\pm 1\%$, $\pm 5\%$, and $\pm 10\%$, respectively.

4. The rate of the primary jet development is reduced by the presence of the confining ejector walls. Compared to free jet results, the reduction of the jet spreading and centerline velocity decay are on the order of 30% and 10%, respectively.

5. The ejector configuration studied has a thrust augmentation ratio of 1.34. The vortices in the three-dimensional flow field are

believed to contribute to the mixing efficiency and thrust augmentation of the ejector. However, the differences in geometry between the current and reference ejectors make it difficult to quantify this contribution.

References

1. Koenig, D. G. "Investigation at Large Scale of Thrusting Ejector Applications to V/STOL Aircraft." In Proceedings: Ejector Workshop for Aerospace Applications, by University of Dayton Research Institute. Ohio: Air Force Wright Aeronautical Laboratories, 1982, 155-178.
2. Green, K. A. and J. D. Cyrus. Thrust Augmenting Ejector Technology for Navy Aircraft. New York: American Institute of Aeronautics and Astronautics, 1977. AIAA paper 77-1239.
3. Porter, J. L. and R. A. Squyers. A Summary/Overview of Ejector Augmentor Theory and Performance. Massachusetts: Vought Corporation, 1981. ATC Report R-91100-9CR-47, Vols. I and II.
4. Bernal, L. and V. Sarohia. An Experimental Investigation of Two-Dimensional Thrust Augmenting Ejectors: Final Report, Part II. Pasadena, California: Jet Propulsion Laboratory, 1984. JPL Publication 84-50, Part II.
5. Lund, Thomas S., Domingo A. Tavella, and Leonard Roberts. A Computational Study of Thrust Augmenting Ejectors Based on a Viscous-Inviscid Approach. Stanford, California: Joint Institute for Aeronautics and Acoustics, 1987. JIAA-TR-77.
6. Alperin, M. and J.-J. Wu. "Thrust Augmenting Ejectors, Part I." AIAA Journal 21 (October 1983): 1428-1436.
7. Alperin, M. and J.-J. Wu. "Thrust Augmenting Ejectors, Part II." AIAA Journal 21 (December 1983): 1698-1706.
8. Bevilaqua, P. M. "Analytic Description of Hypermixing and Test of an Improved Nozzle." Journal of Aircraft 13 (January 1976): 43-48.
9. Mefferd, L. A. and P. M. Bevilaqua. Computer-Aided Design Study of Hypermixing Nozzles. Columbus, Ohio: Rockwell International, 1978. NR 78H-91.
10. Sarohia, V., L. Bernal, and T. Bui. Entrainment and Thrust Augmentation in Pulsatile Ejector Flows. Pasadena, California: Jet Propulsion Laboratory, 1981. JPL Publication 81-36.

11. Driver, David M. and Sheshagiri K. Hebbar. "Experimental Study of a Three-Dimensional, Shear-Driven Turbulent Boundary Layer." AIAA Journal 25 (January 1987): 35-42.
12. Ramaprian, B. R. and M. S. Chandrasekhara. "LDA Measurements in Plane Turbulent Jets." Journal of Fluids Engineering 107 (June 1985): 264-271.
13. Nakayama, A. "Measurements of Separating Boundary Layer and Wake of an Airfoil Using Laser Doppler Velocimetry." In AIAA 23rd Aerospace Sciences Meeting. New York: American Institute of Aeronautics and Astronautics, 1985, 1-10.
14. McLaughlin, D. K. and W. G. Tiederman. "Biasing Correction for Individual Realization of Laser Anemometer Measurements in Turbulent Flows." The Physics of Fluids 16 (December 1973): 2082-2088.
15. Orloff, Kenneth L. and Lawrence E. Olson. "High-Resolution LDA Measurements of Reynolds Stress in Boundary Layers and Wakes." AIAA Journal 20 (May 1982): 624-631.
16. Spiegel, M. R. Probability and Statistics. New York: McGraw-Hill Book Co., 1975, 194-198.
17. Bradbury, L. J. S. "The Structure of a Self-Preserving Turbulent Plane Jet." Journal of Fluid Mechanics 23 (May 1965): 31-64.
18. Gutmark, E. and I. Wygnanski. "The Planar Turbulent Jet." Journal of Fluid Mechanics 73 (August 1976): 465-495.
19. Daily, J. W. and R. F. Harleman. Fluid Dynamics. Massachusetts: Addeson-Wesley Publishing Company, 1966, 415-419.

APPENDIX A
Tables and Figures

Table 1: Ejector geometry. All dimensions in millimeters.

d	2.4
H	38.1
L	181.8
X	48.4
S	114.3

Table 2: Survey locations. H = hot wire; L = LDV.

	<u>z/d</u>		
<u>x/L</u>	-2.6	-3.9	-5.2
0.00	L	L	L
0.02	H&L	H&L	L
0.08	H&L	H&L	L
0.17	H&L	H&L	L
0.29	H&L	H&L	H&L
0.44	H&L	H&L	H&L
0.62	H&L	H&L	H&L
0.80	H&L	H&L	H&L
1.0	H&L	H&L	H&L
1.2	H&L	H&L	L

Table 3: Calculated jet exit velocities for $z/d=-2.6$.
(All values in m/s)

<u>x/L</u>	LDV	Hot wire
0.00	139.3	-
0.02	143.0	144.0
0.08	142.3	142.6
0.17	136.4	142.6
0.29	134.5	142.4
0.44	134.8	142.0
0.62	134.2	139.9
0.80	133.8	142.7
1.0	135.2	143.6
1.2	162.2	148.9

Table 4: Calculated jet exit velocities for $z/d=-3.9$.
(All values in m/s)

<u>x/L</u>	LDV	Hot wire
0.00	131.3	-
0.02	129.6	147.4
0.08	130.3	145.6
0.17	133.0	151.1
0.29	134.3	141.2
0.44	135.4	151.2
0.62	136.0	142.5
0.80	136.8	144.9
1.0	137.6	150.5
1.2	139.8	144.9

Table 5: Calculated jet exit velocities for $z/d=-5.2$.
(All values in m/s)

<u>x/L</u>	LDV	Hot wire
0.00	139.1	-
0.02	132.3	-
0.08	134.3	-
0.17	136.2	-
0.29	140.8	146.1
0.44	141.7	141.7
0.62	142.7	146.2
0.80	146.0	148.6
1.0	143.8	150.2
1.2	150.9	-

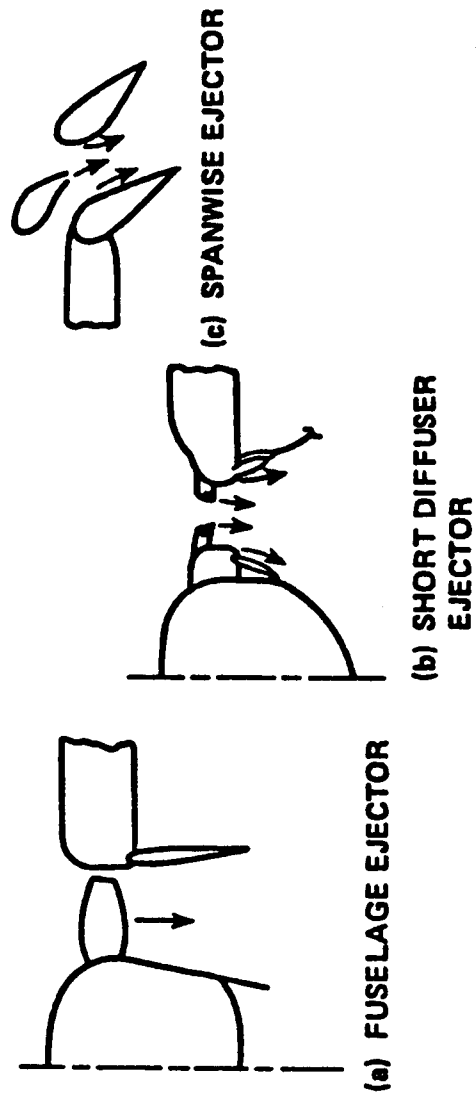


Figure 1: Thrust augmenting ejector concepts for V/STOL aircraft from Ref. 1.

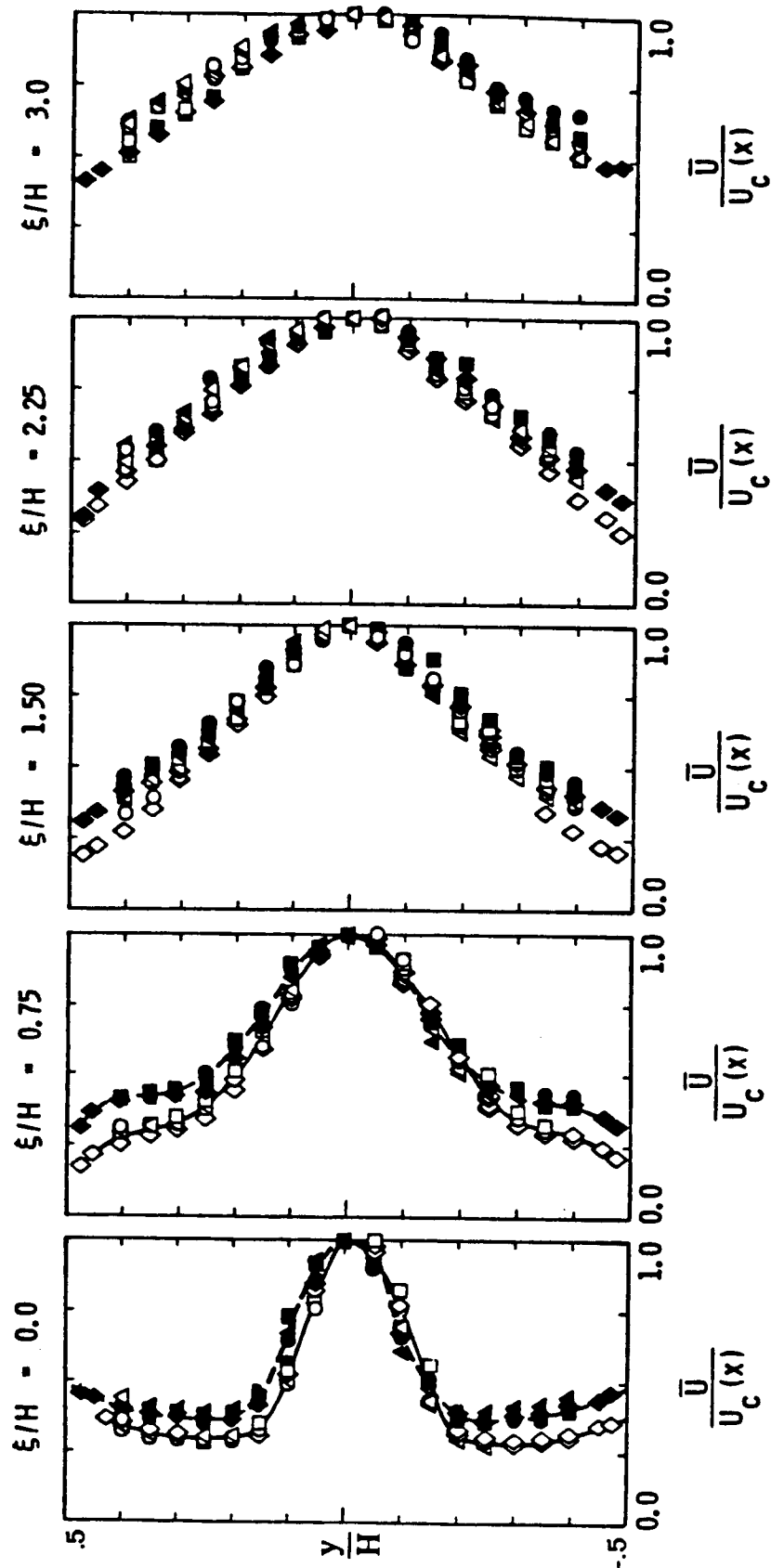


Figure 2: Axial velocity profiles in the mixing chamber of the two-dimensional ejector studied in Ref. 4 using laser Doppler velocimetry. Open symbols represent constant area ejector. Solid symbols represent diffused flow ejector. \square , $\text{Pr}=1.06$; \circ , $\text{Pr}=1.45$; Δ , $\text{Pr}=2.04$; \diamond , $\text{Pr}=1.06$ one velocity component LDV system.

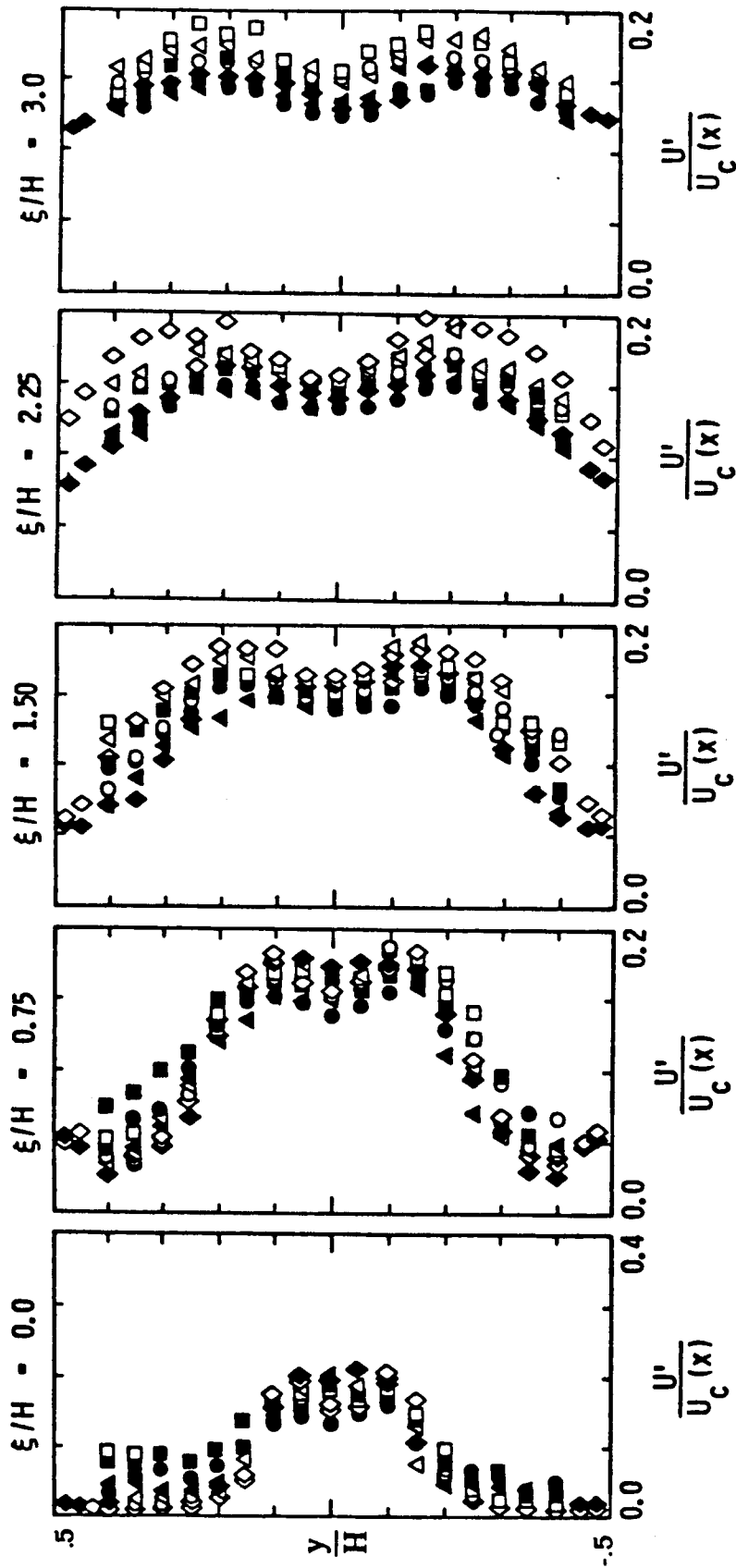


Figure 3: Axial turbulence intensity profiles in the mixing chamber of the two-dimensional ejector from Ref. 4. For a key to the symbols, see the caption of Figure 2.

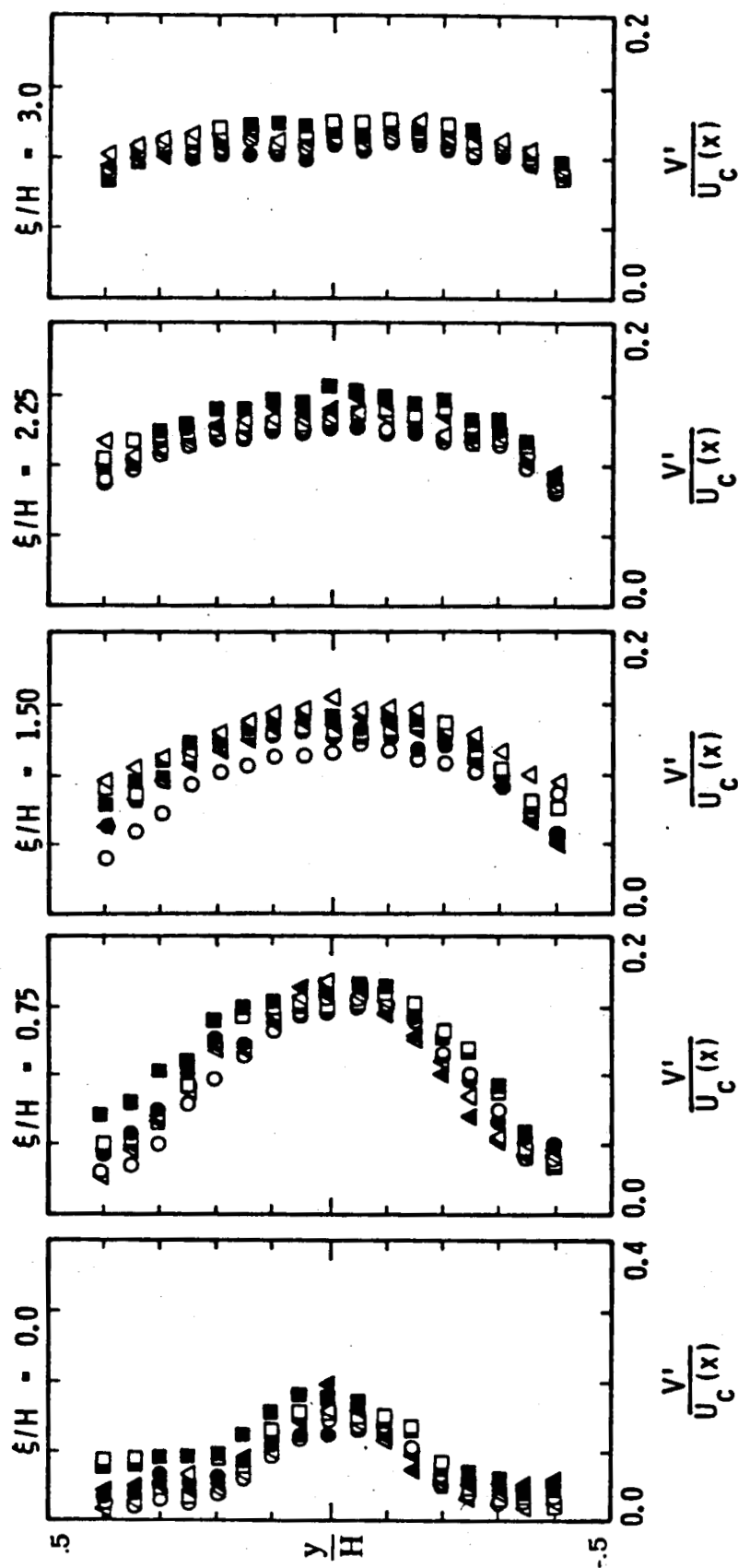


Figure 4: Transverse turbulence intensity profiles in the mixing chamber of the two-dimensional ejector from Ref. 4. For a key to the symbols, see the caption of Figure 2.

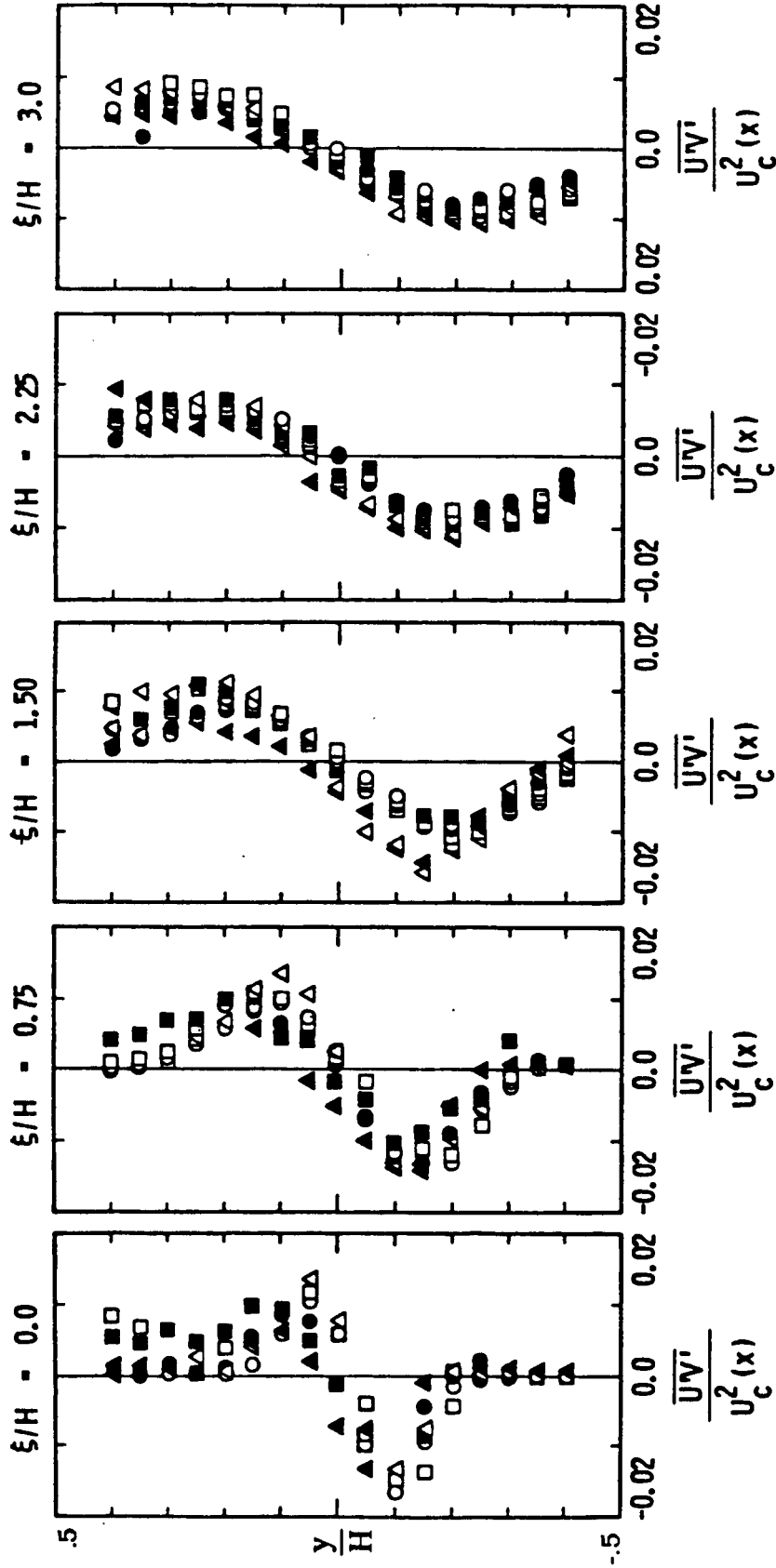


Figure 5: Reynolds stress profiles in the mixing chamber of the two-dimensional ejector from Ref. 4. For a key to the symbols, see the caption of Figure 2.

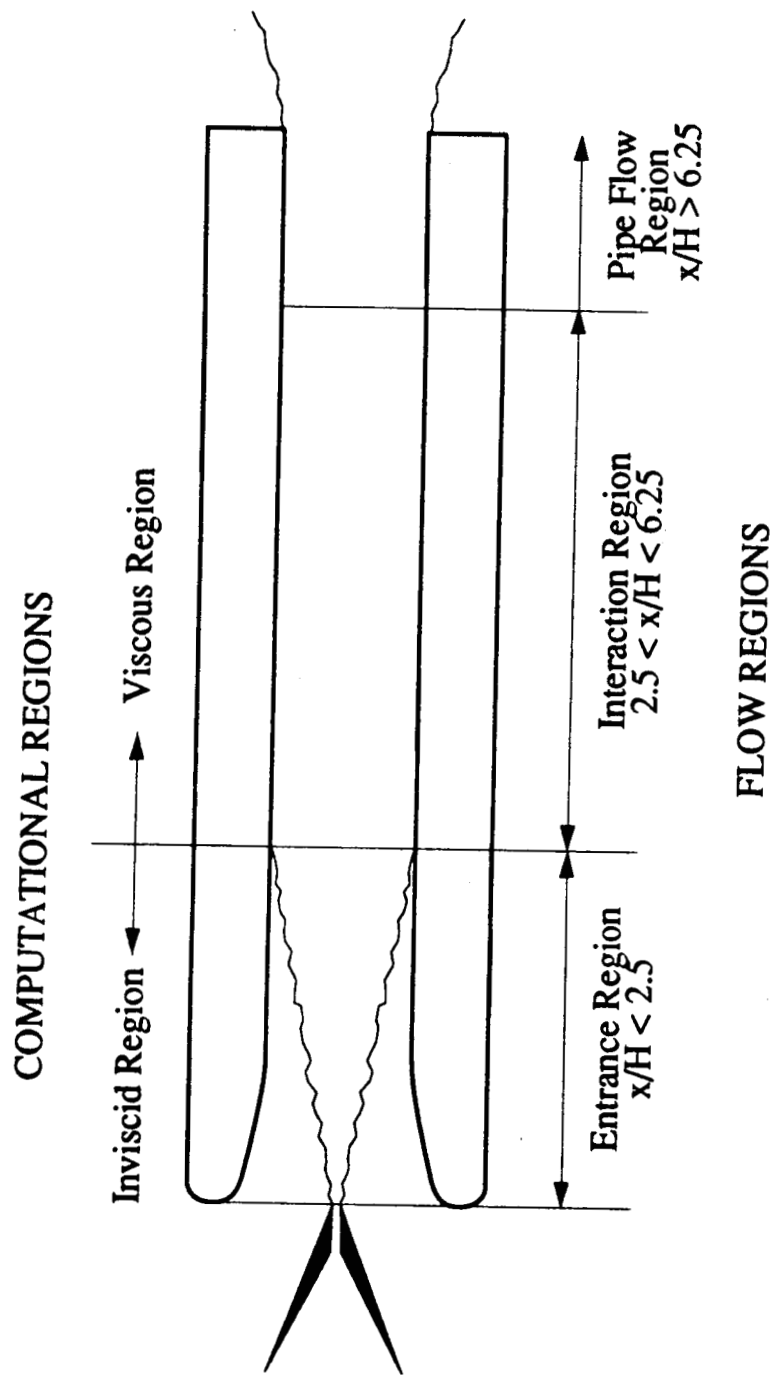


Figure. 6: Regions of the ejector flow field defined by Ref. 4 and 5.

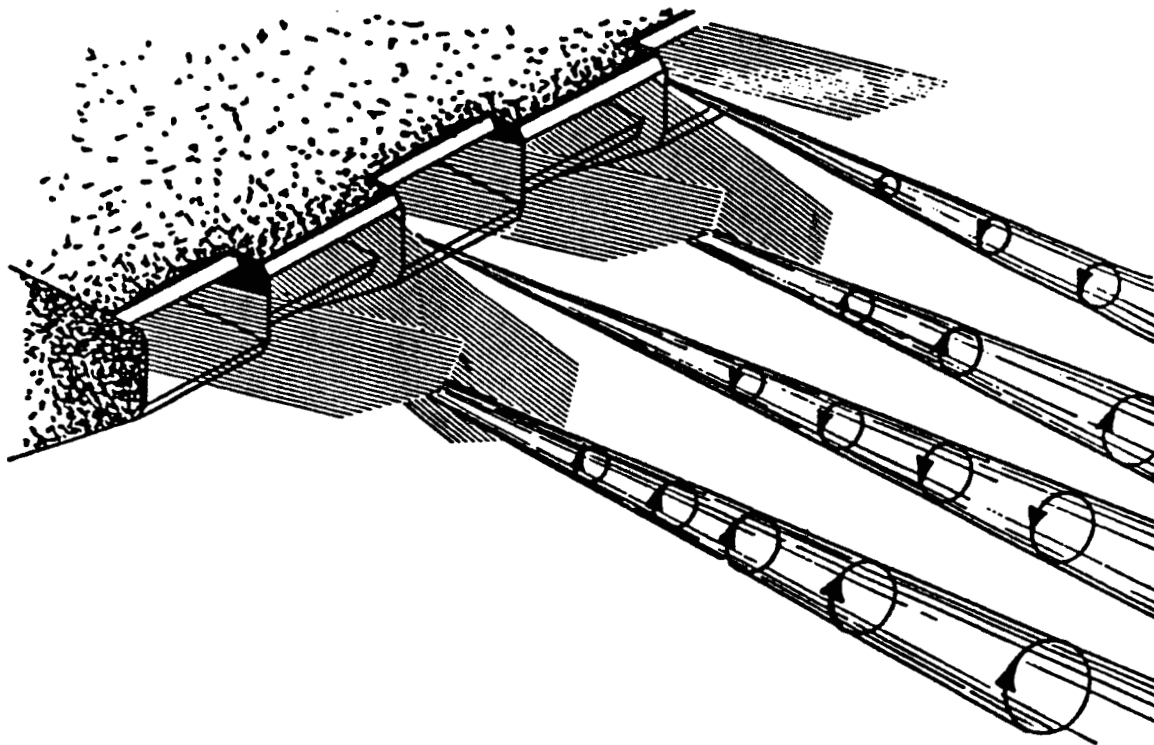


Figure 7: Hypermixing nozzle exit studied in Ref. 8.

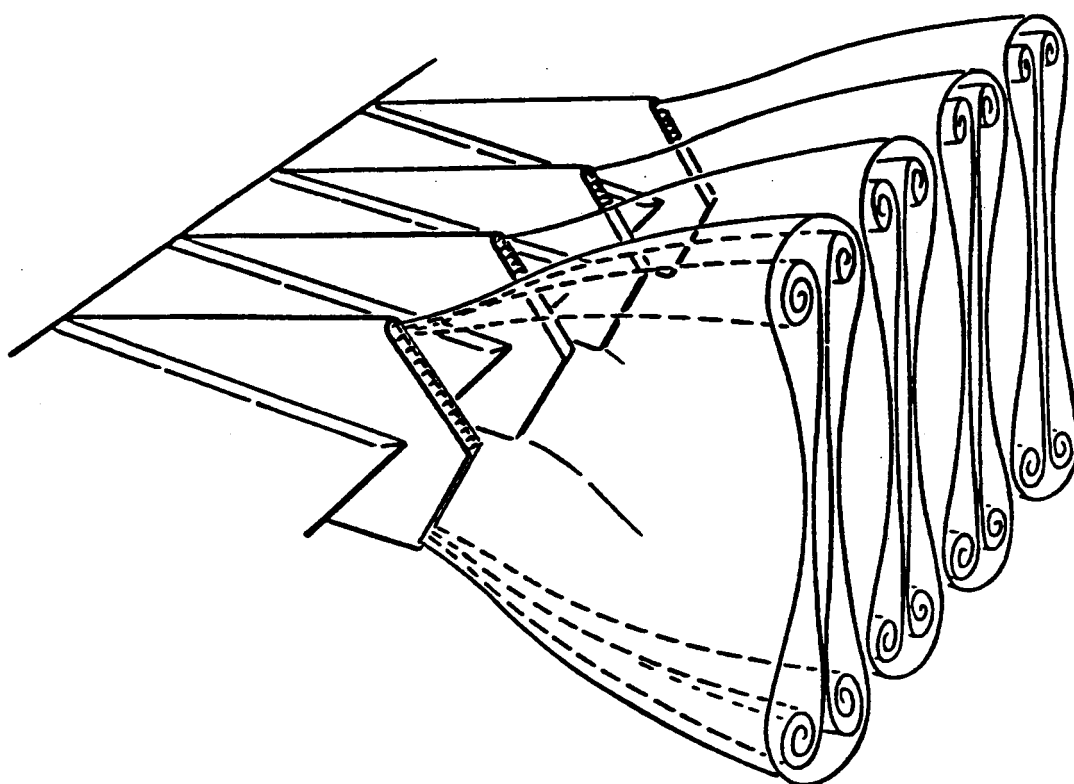


Figure 8: Cross slot nozzle exit studied in Ref. 9.

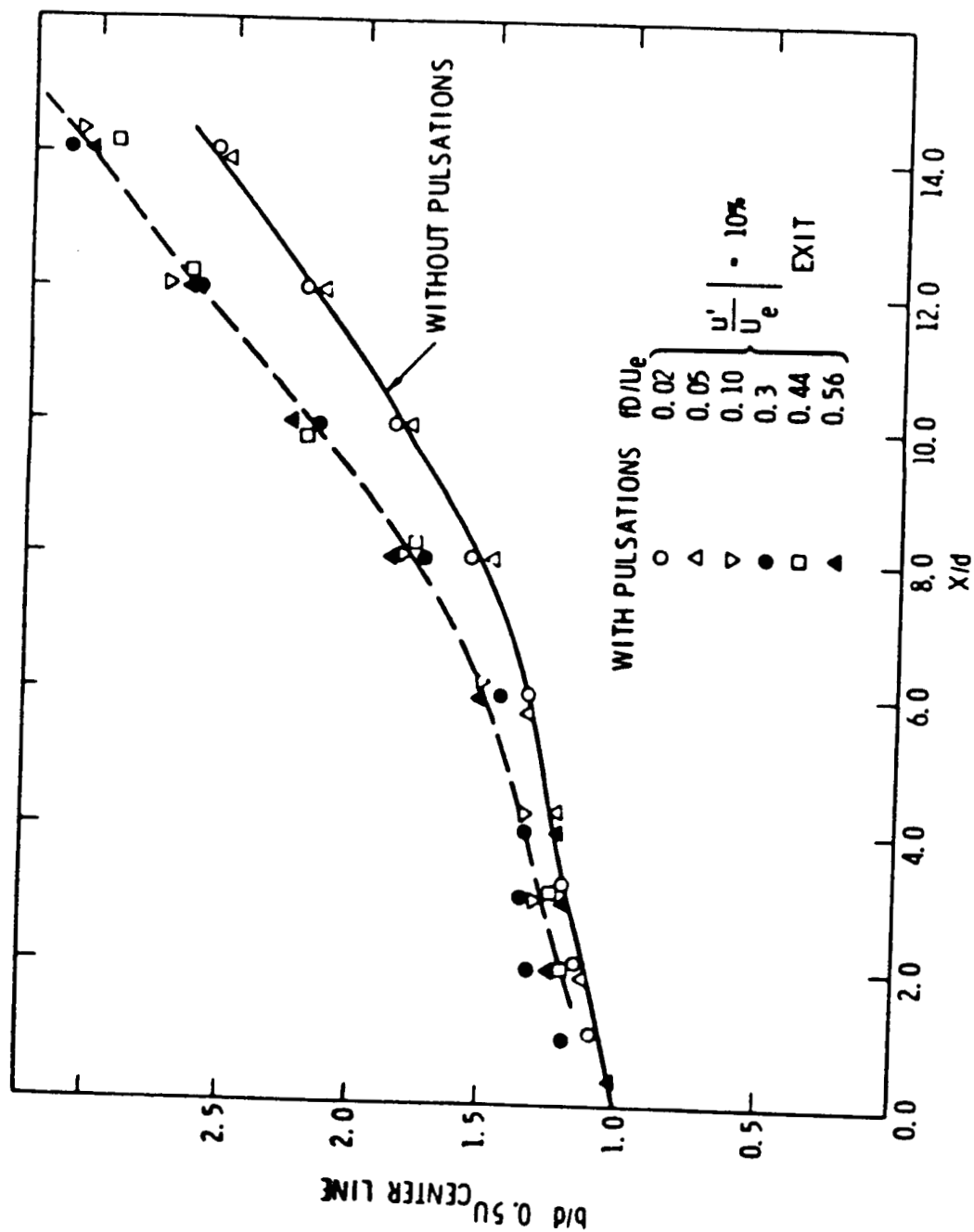


Figure 9: Growth of axisymmetric free jet with and without pulsations obtained in Ref. 10 using hot wire anemometry.

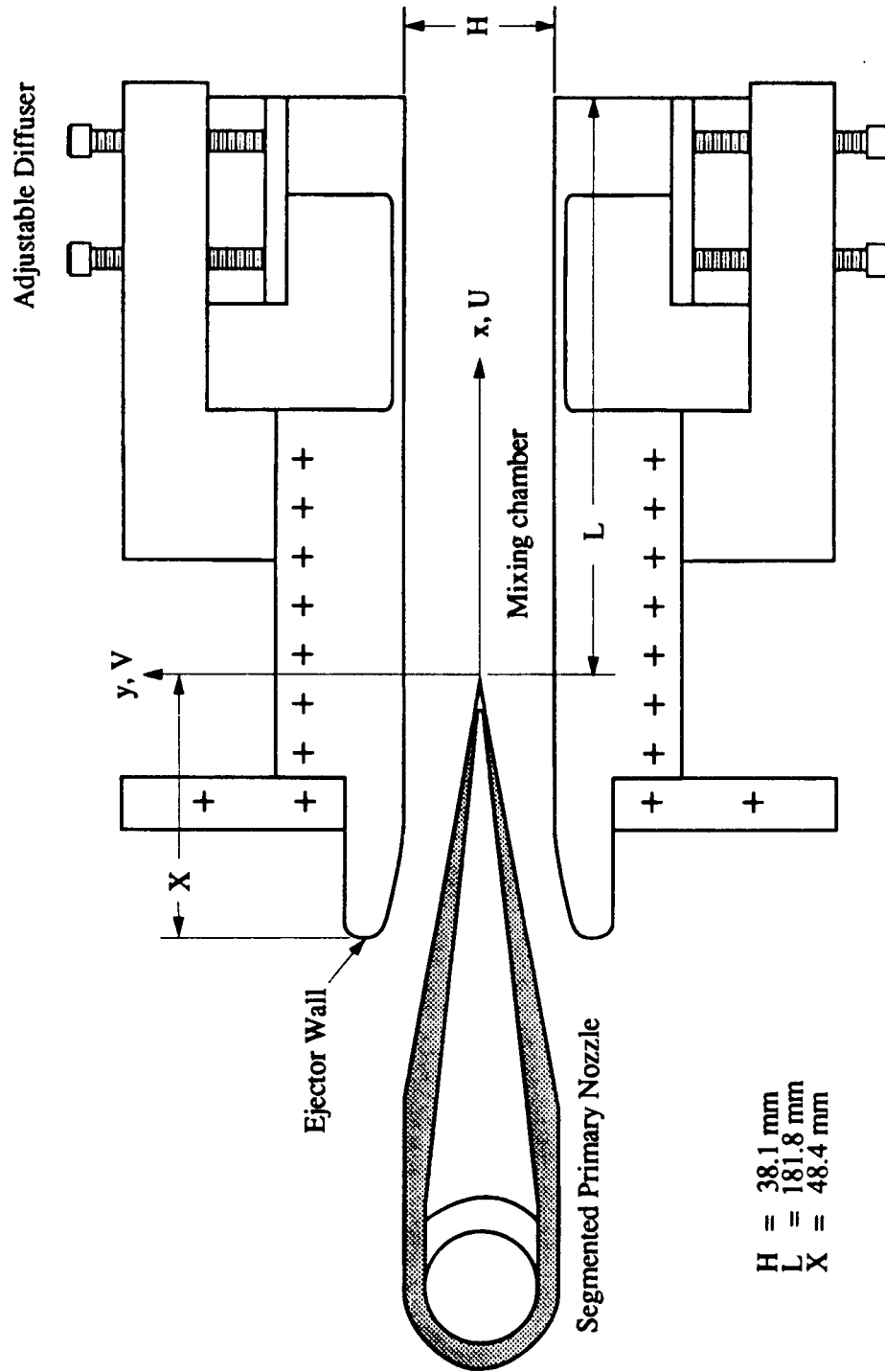
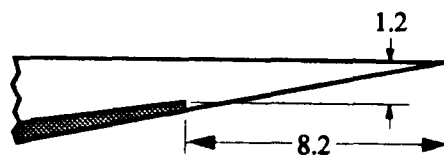
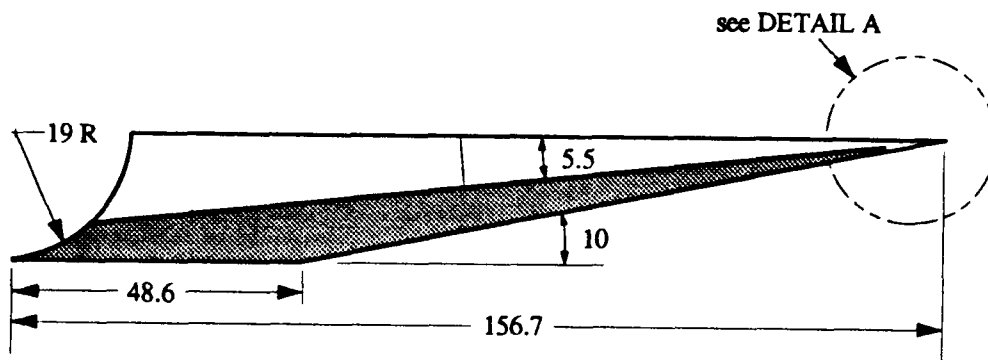
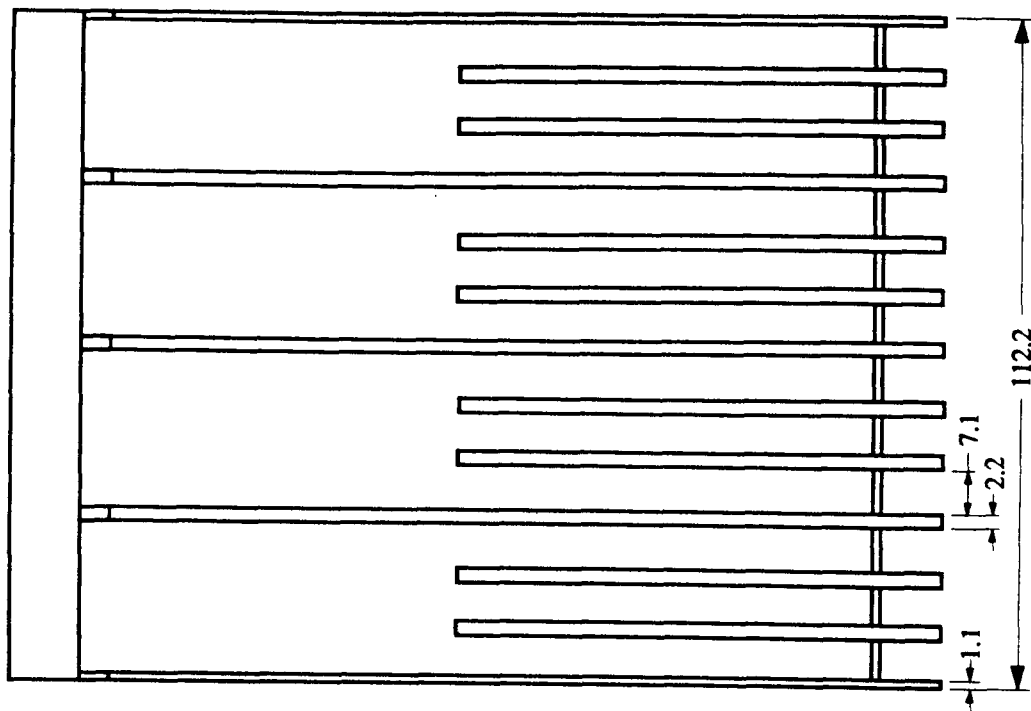


Figure. 10: Constant area ejector geometry showing primary nozzle and mixing chamber.



DETAIL A

Figure. 11: Primary nozzle geometry. All dimensions in millimeters.

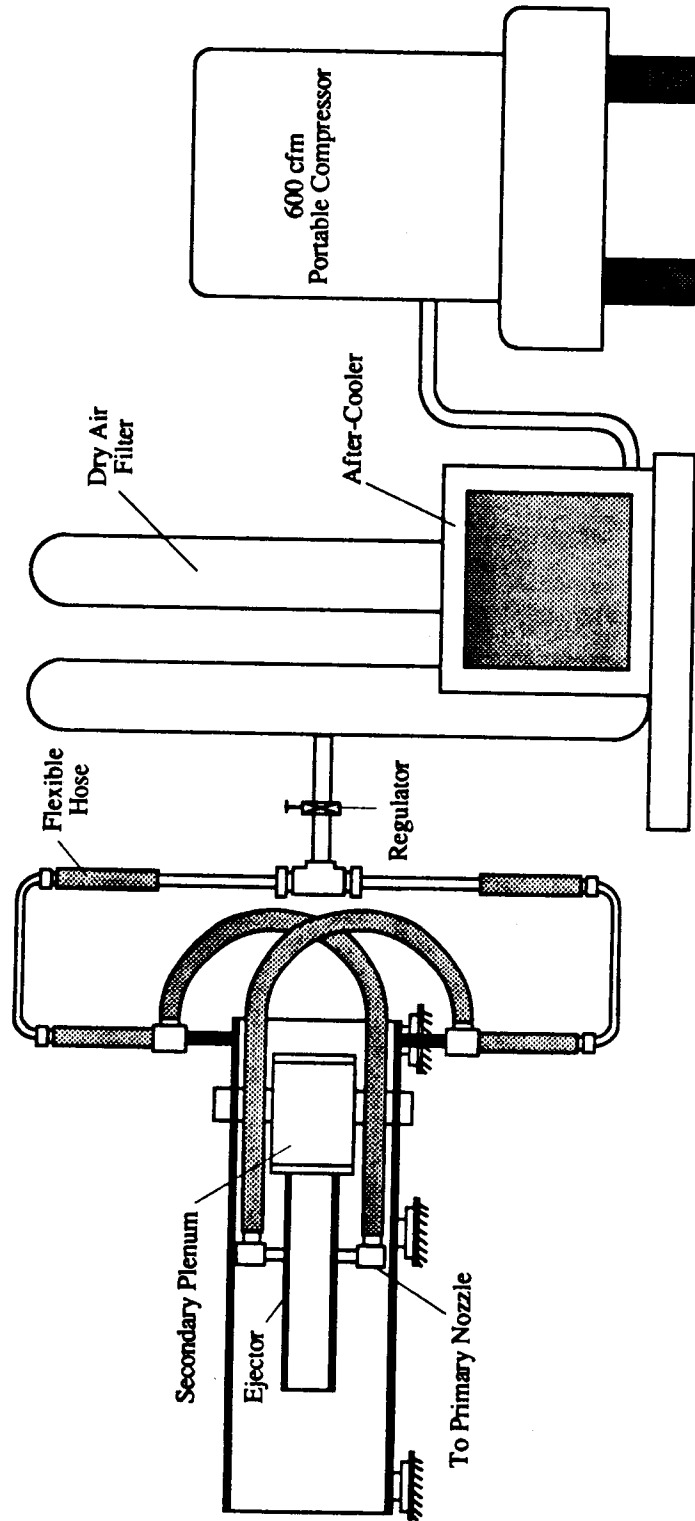


Figure 12: Plumbing schematic for primary air supply.

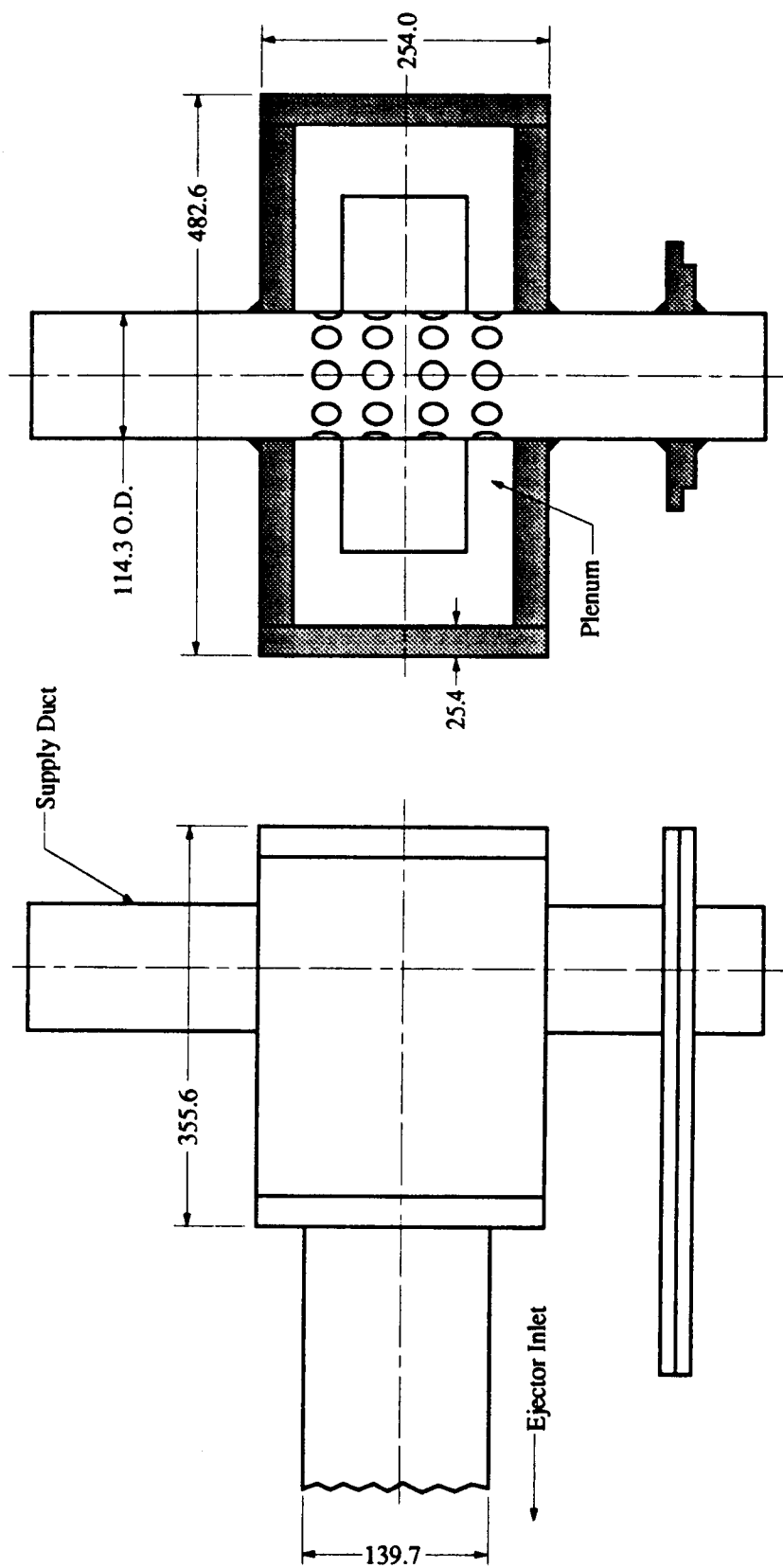


Figure 13: Secondary air plenum with vertical perforated pipe. All dimensions in millimeters.

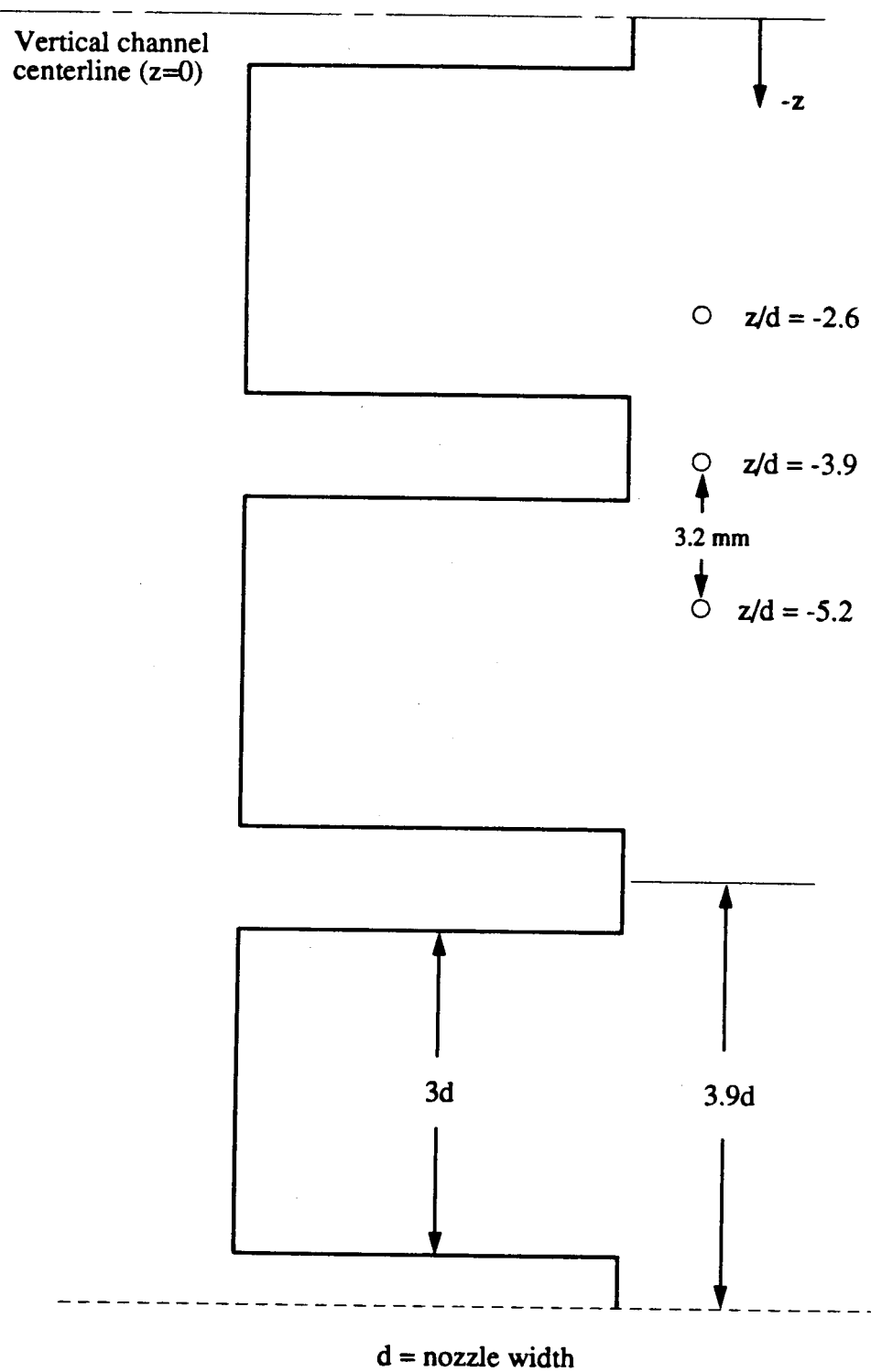


Figure. 14: Three segments of ejector nozzle showing vertical measurement stations.

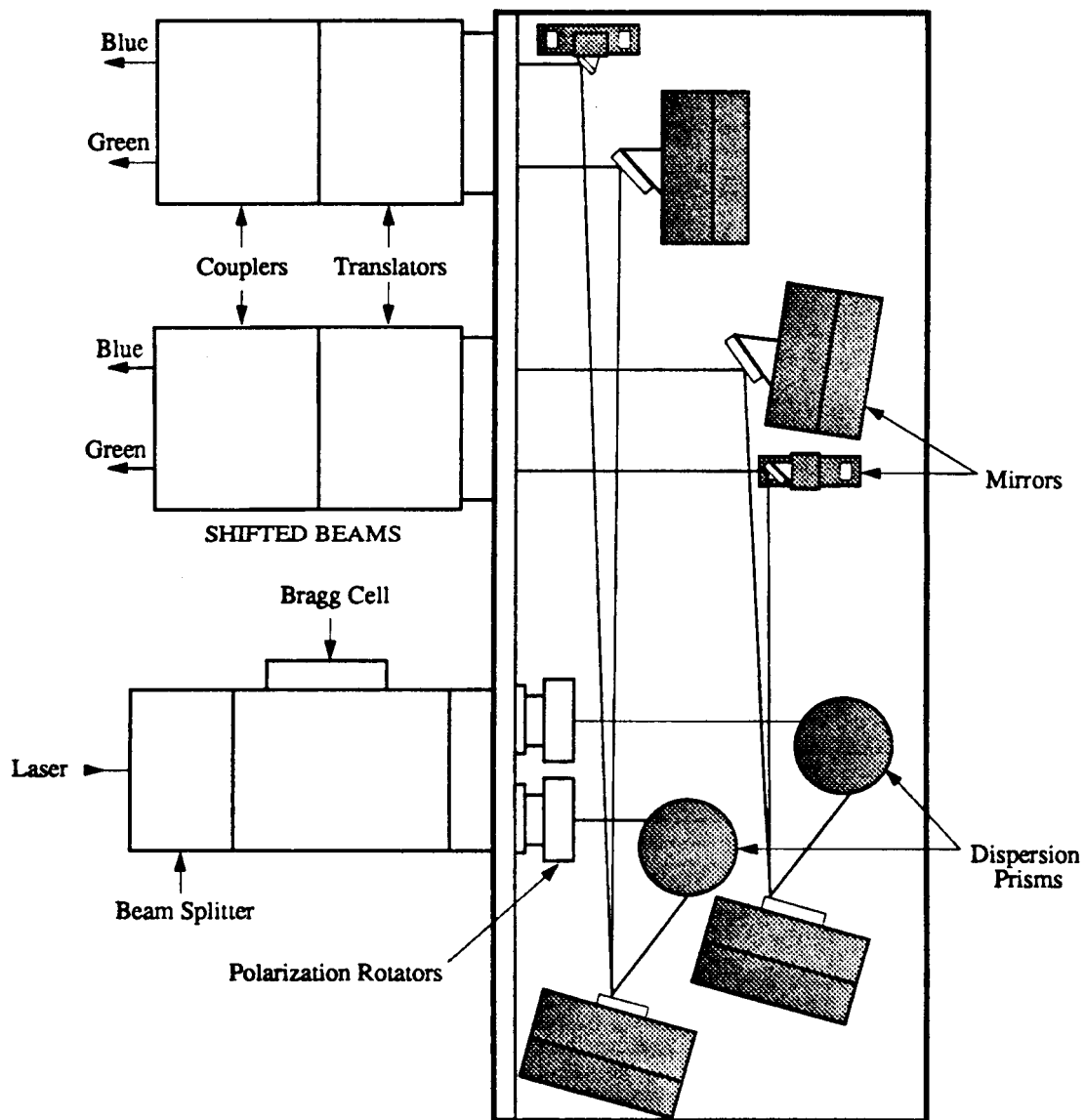
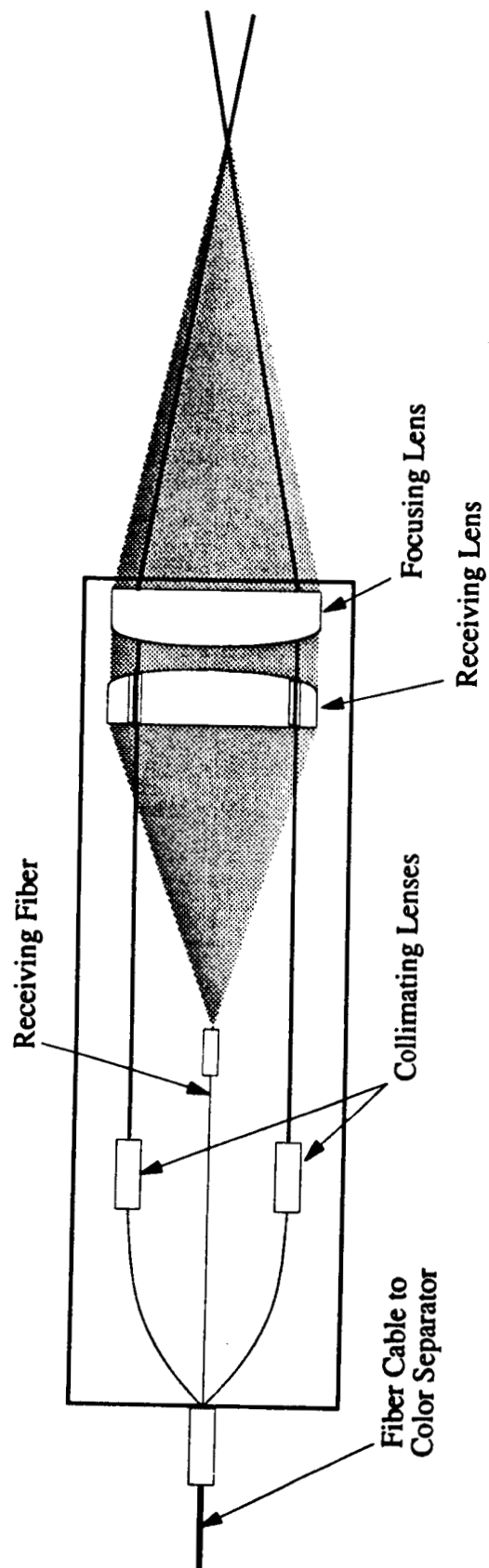


Figure. 15: LDV optics for color separation and coupling to fiber optic cables.



NOTE: Only one beam pair is shown for simplicity.

Figure. 16: Fiber optic probe in backscatter configuration.

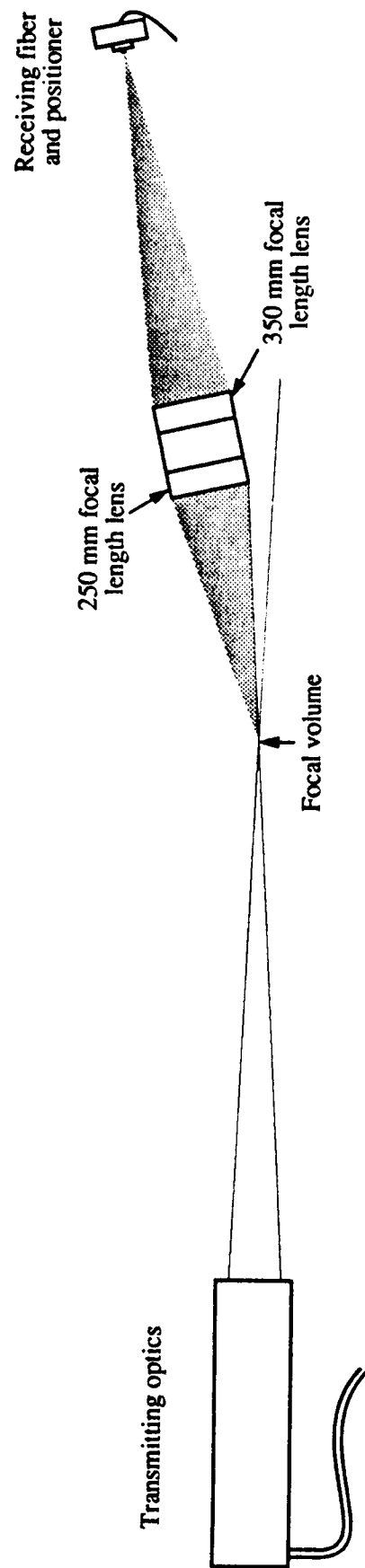


Figure. 17: LDV forward scatter configuration.

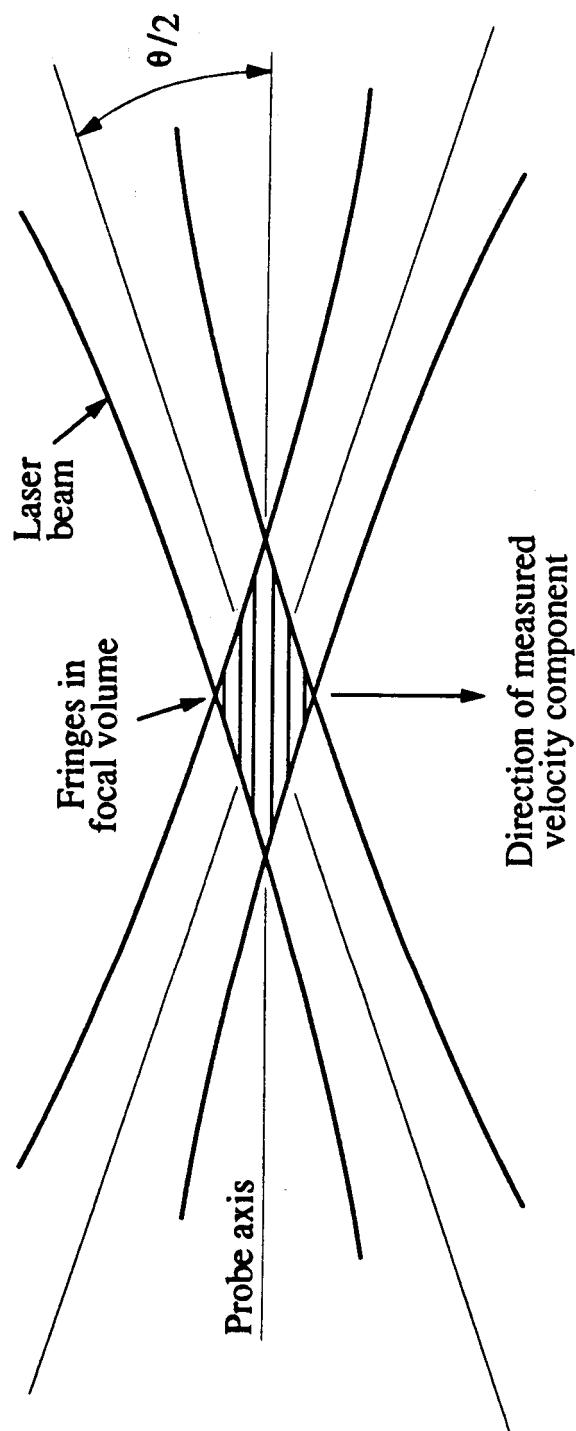


Figure. 18: Laser Doppler velocimeter focal volume.

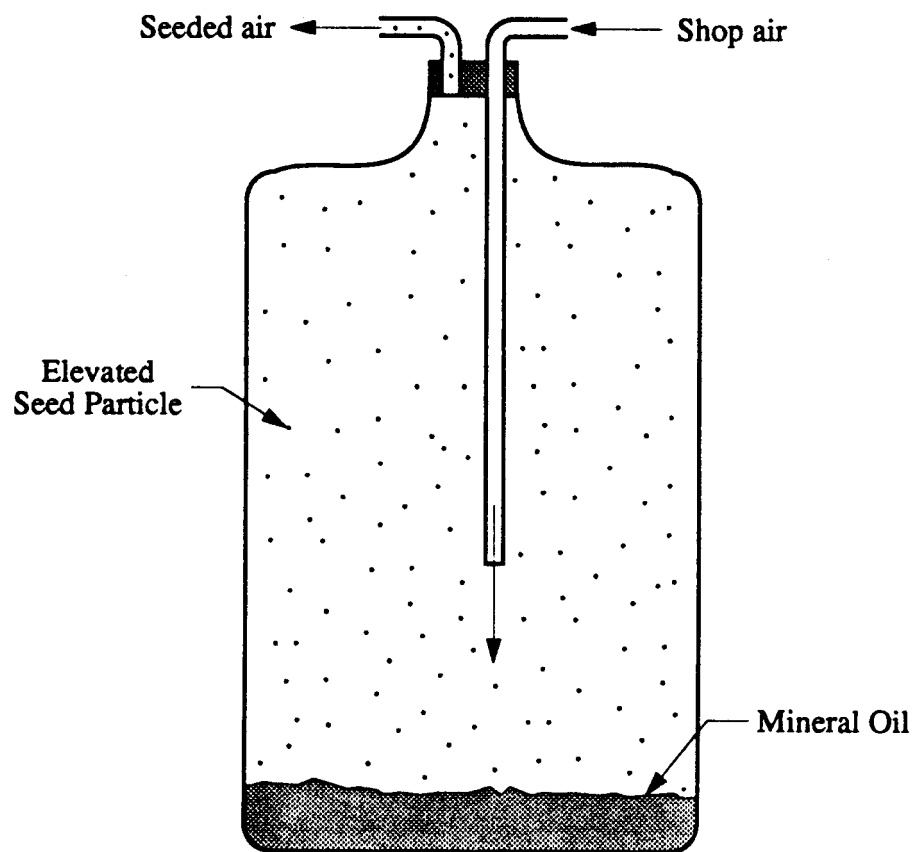


Figure. 19: Mineral oil seeding device.

Run: 32 ; Index: 24 ; Time: 19 : 17 , 5 Jan 1989
 Baro = 14.68 psia, Rm_temp = 63 F, Tt_tun = 56 F
 PPI = 1.622 PP2 = .0514 psid Load = -.7397 Lbs.
 Sens. 1 = -5.61304 m/s/MHz, Sens. 2 = -5.25588 m/s/MHz
 Synth 1 = 25 , Synth 2 = 25 1024 samples/chan
 Coinc. time = 10 , Elapsed time = 16 sec.
 Low filters: Lf1 = 8 , Lf2 = 8
 High filters: Hf1 = 16 , Hf2 = 16
 Chnl. 1 counter acc. = 7 , 5/8
 Chnl. 2 counter acc. = 7 , 5/8

X = 13.8 mm X/L = .076
 Y = 12.7 mm Y/H = .33
 Z = 44.5 mm Z/W = 6.2

Flow quantities

Uj(m/s)	:	+1.351E+02 (-1.99%)	
U1(m/s)	:	+2.205E+01 (+/- 7.4E-02)	U1/Uc = +.3380
U2	:	-5.853E-01 (+/- 9.0E-02)	U2/Uc = -.0090
Umag	:	+2.206E+01 (+/- 0.0E+00)	
Theta	:	-1.520E+00 (+/- 0.0E+00)	
U11(m/s)	:	+1.205E+00 (+/- 5.2E-02)	U11/Uc = +.0185
U22	:	+1.464E+00 (+/- 6.3E-02)	U22/Uc = +.0224
U12	:	-3.967E-02 (+/- 3.4E-03)	U12/Uc = -0.0000
U11/Uu	:	+5.463E-02 (+/- 2.4E-03)	
U22/Uu	:	+6.638E-02 (+/- 2.9E-03)	
U12/U11/U22:	:	-2.248E-02 (+/- 1.9E-03)	

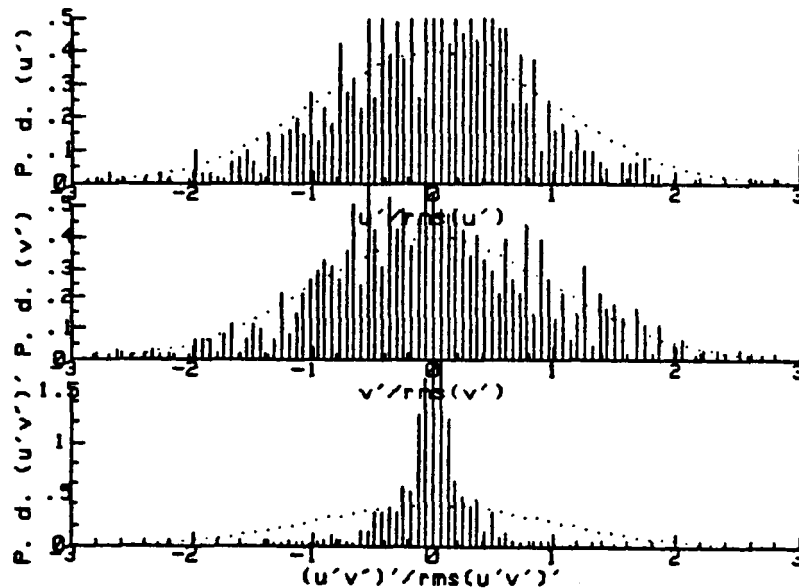


Figure 20: Diagnostic print out generated by LDV and hot wire data acquisition routines.

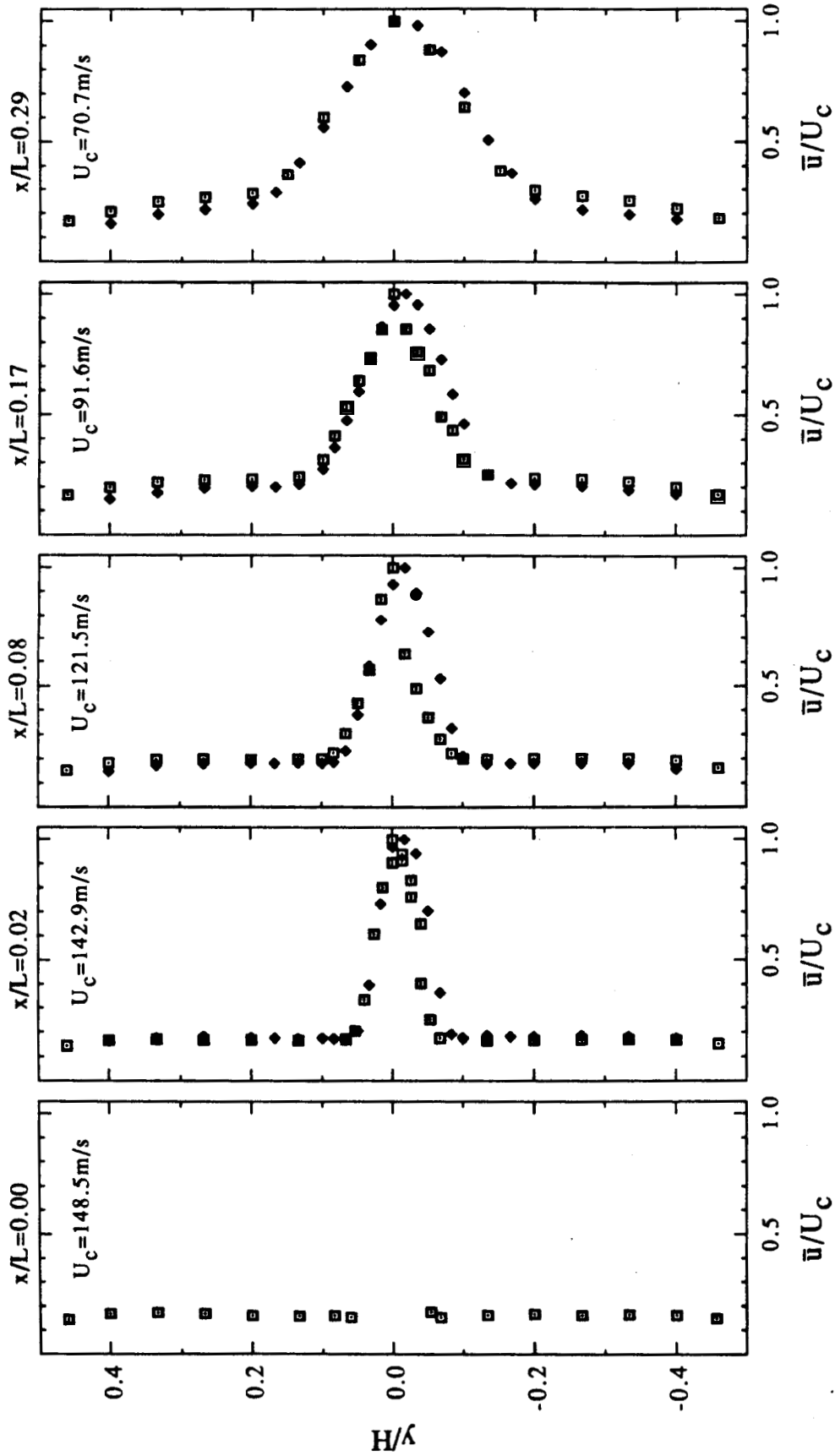


Figure 21: Axial velocity profiles at $z/d = -2.6$ obtained by LDV (\square) and hot wire anemometry (\blacklozenge) for $0 \leq x/L \leq 0.29$.

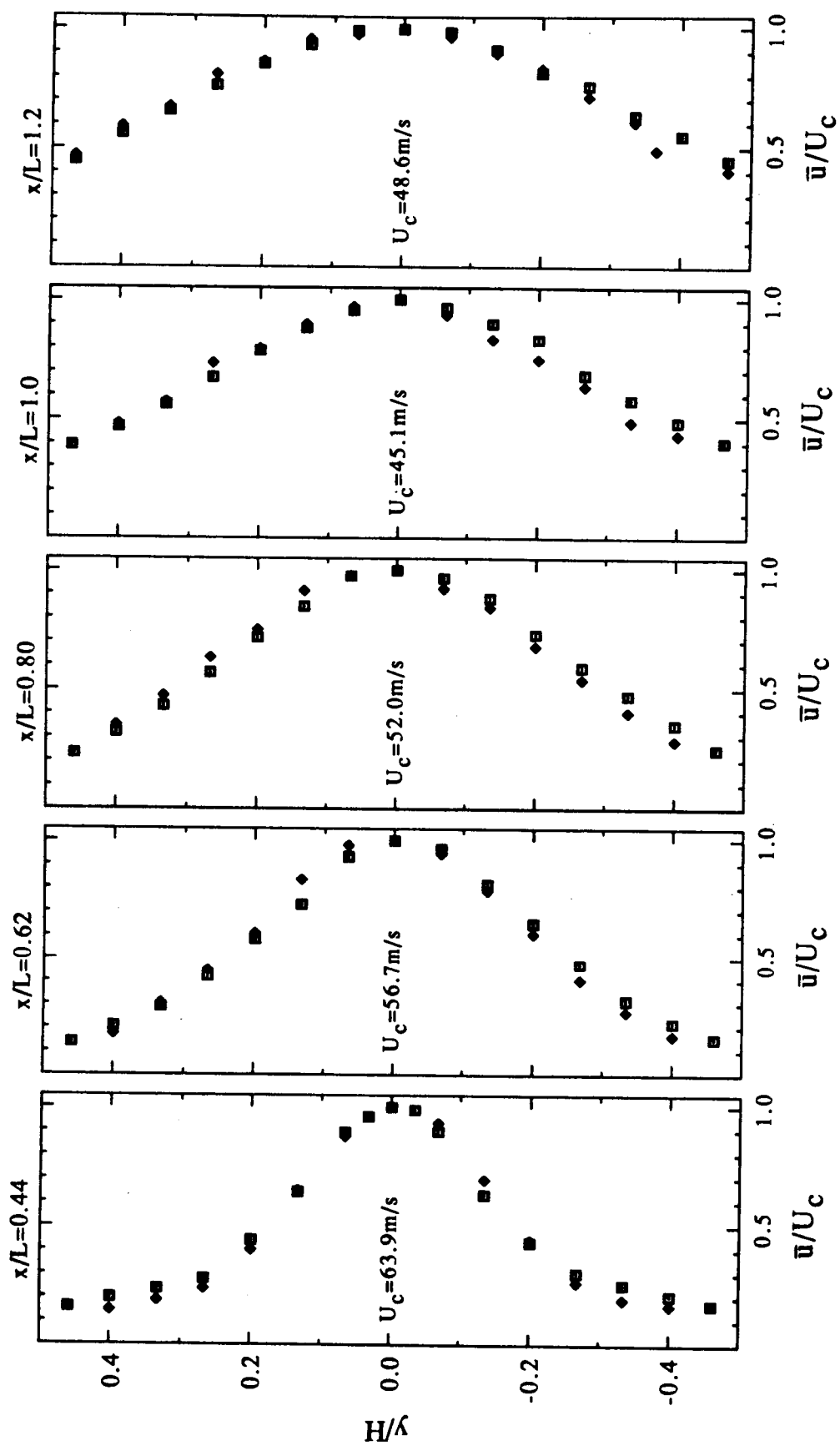


Figure 22: Axial velocity profiles at $z/d = -2.6$ obtained by LDV (\square) and hot wire anemometry (\diamond) for $0.44 \leq x/L \leq 1.2$.

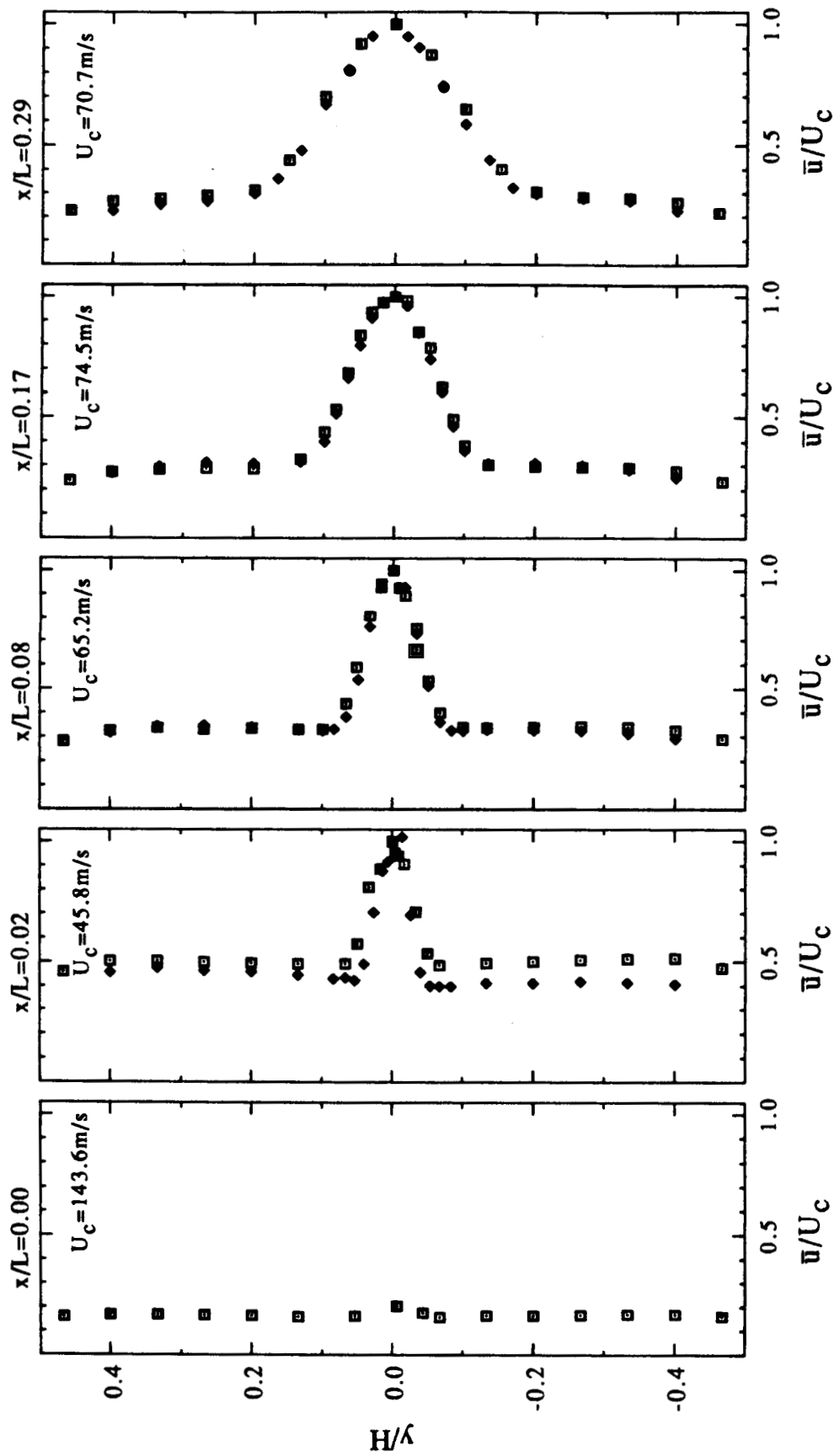


Figure 23: Axial velocity profiles at $z/d = -3.9$ obtained by LDV (\square) and hot wire anemometry (\diamond) for $0 \leq x/L \leq 0.29$.

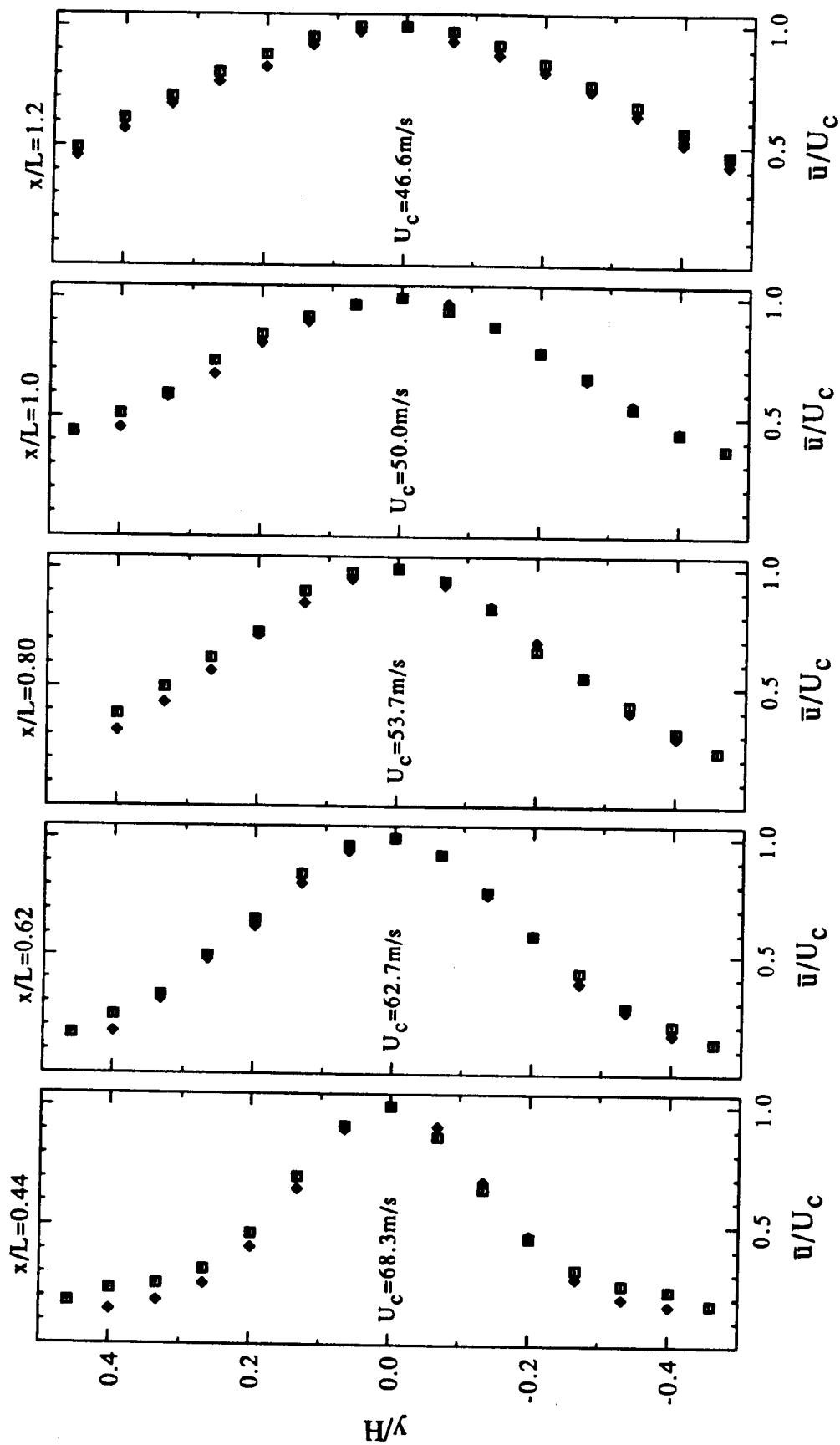


Figure 24: Axial velocity profiles at $z/d = -3.9$ obtained by LDV (\square) and hot wire anemometry (\diamond) for $0.44 \leq x/L \leq 1.2$.

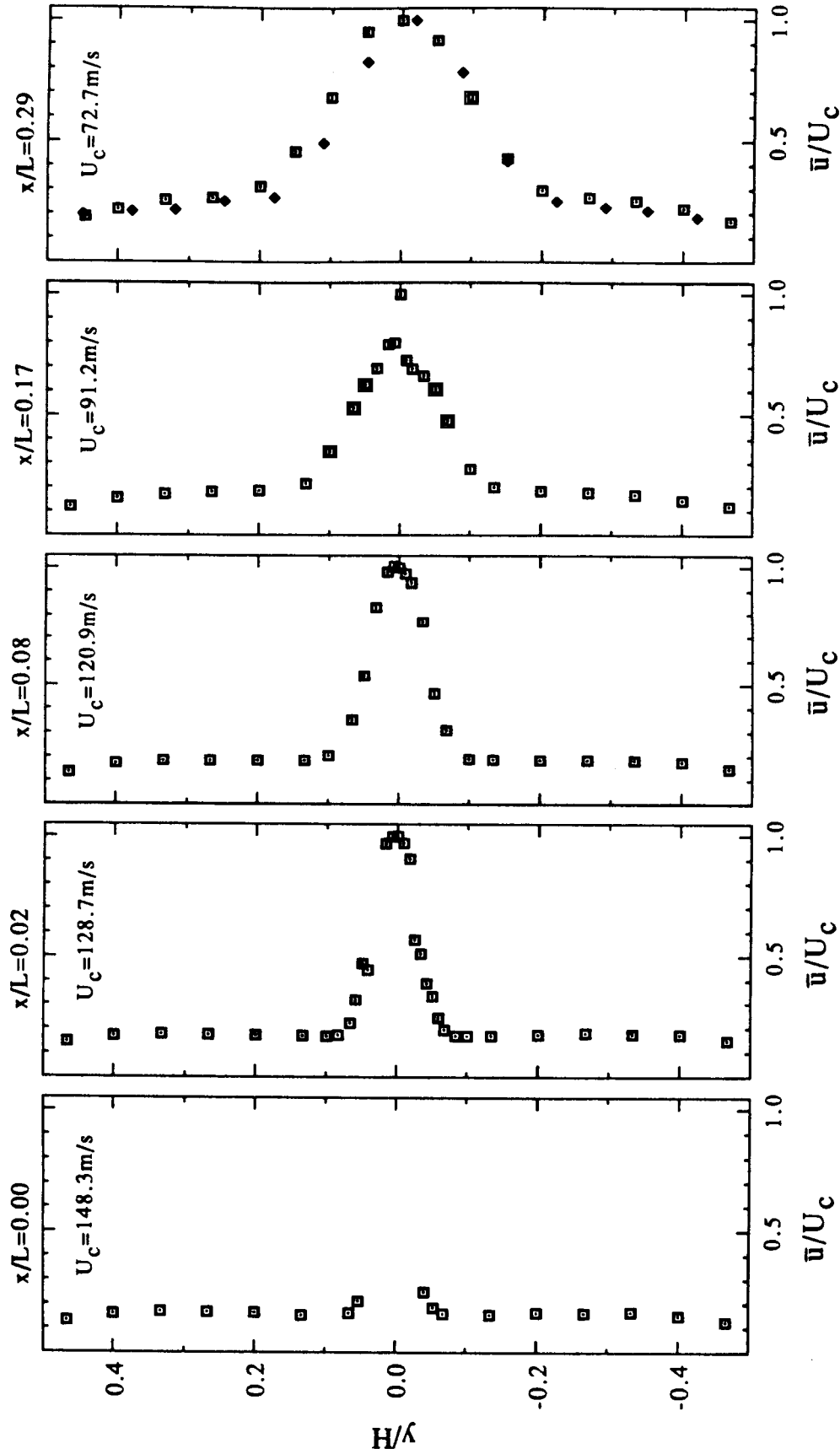


Figure 25: Axial velocity profiles at $z/d = -5.2$ obtained by LDV (\square) and hot wire anemometry (\blacklozenge) for $0 \leq x/L \leq 0.29$.

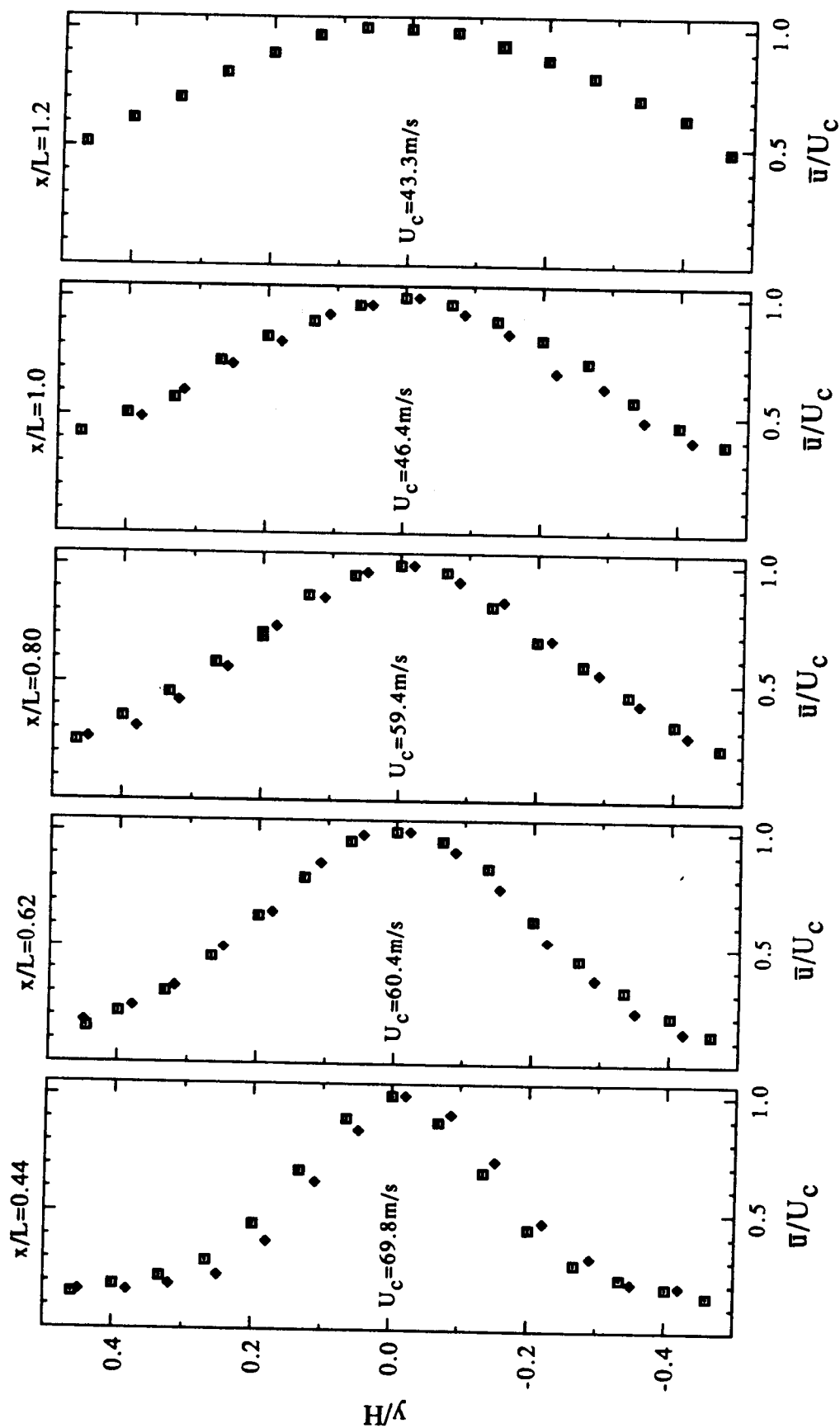


Figure 26: Axial velocity profiles at $z/d = -5.2$ obtained by LDV (\square) and hot wire anemometry (\diamond) for $0.44 \leq x/L \leq 1.2$.

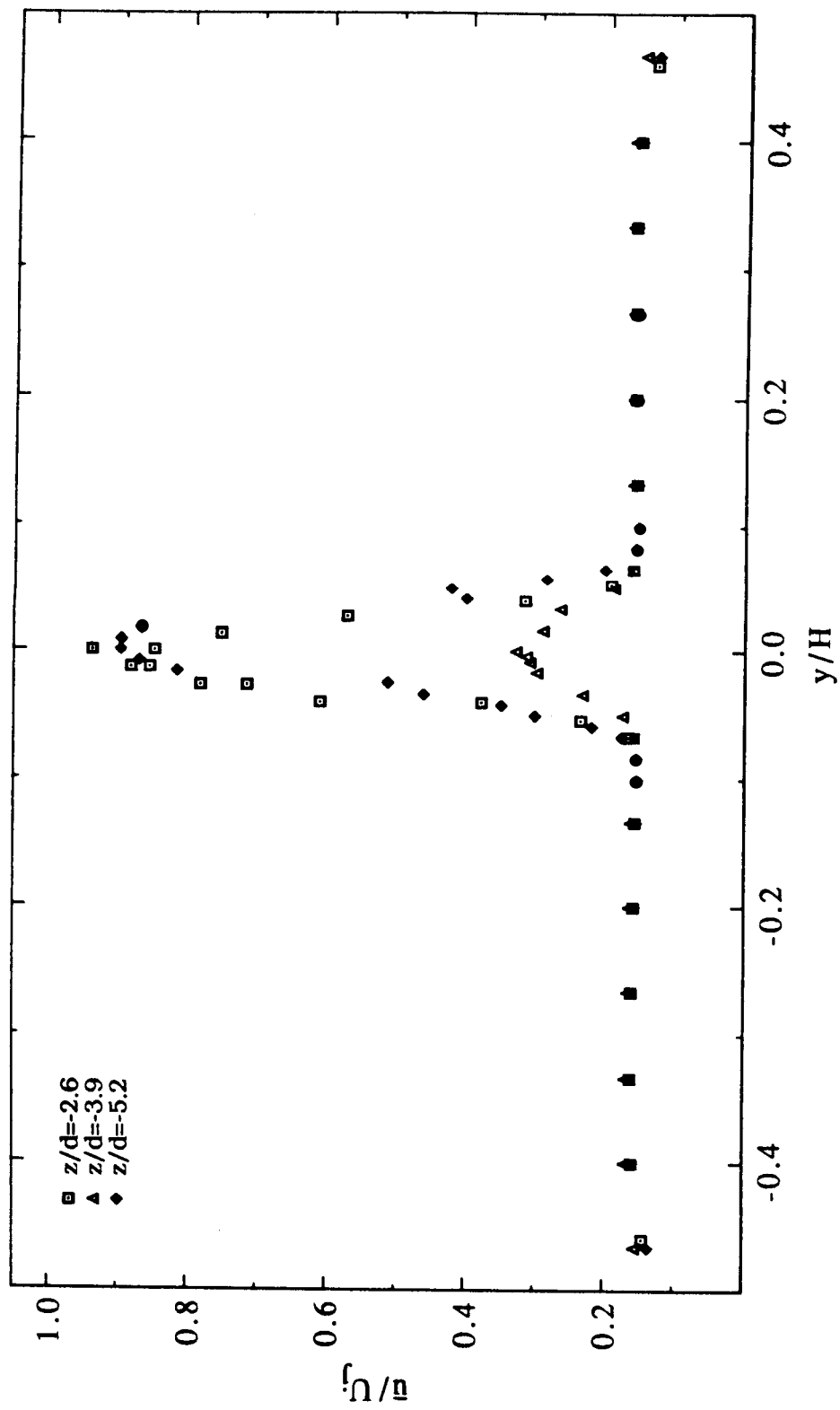


Figure 27: Axial velocity profiles at $x/L = 0.02$ obtained by LDV and normalized by the calculated jet exit velocity.

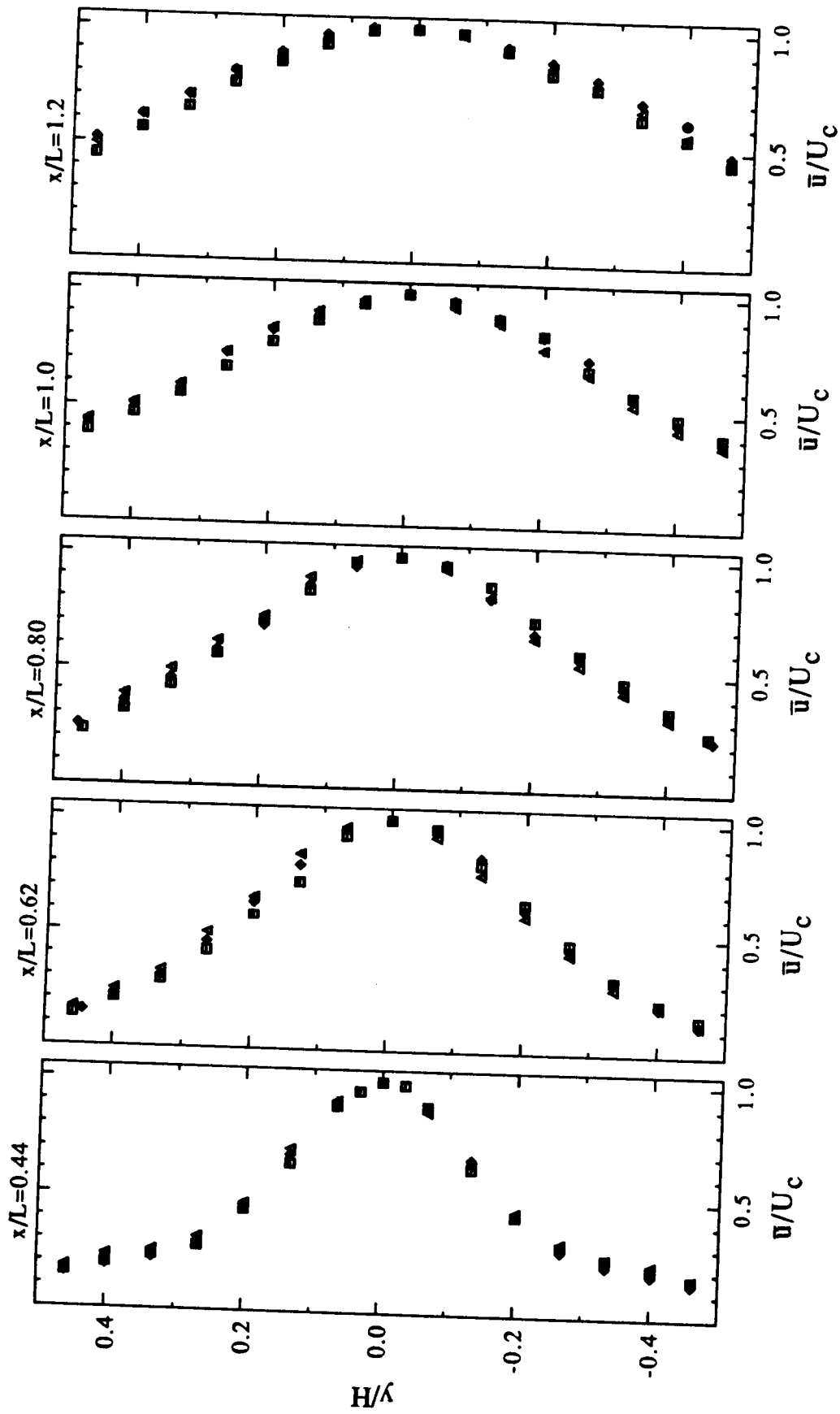


Figure 28: Axial velocity profiles at $z/d = -2.6$ (\square), -3.9 (Δ), and -5.2 (\diamond) obtained by LDV for 0.44 $\leq x/L \leq 1.2$.

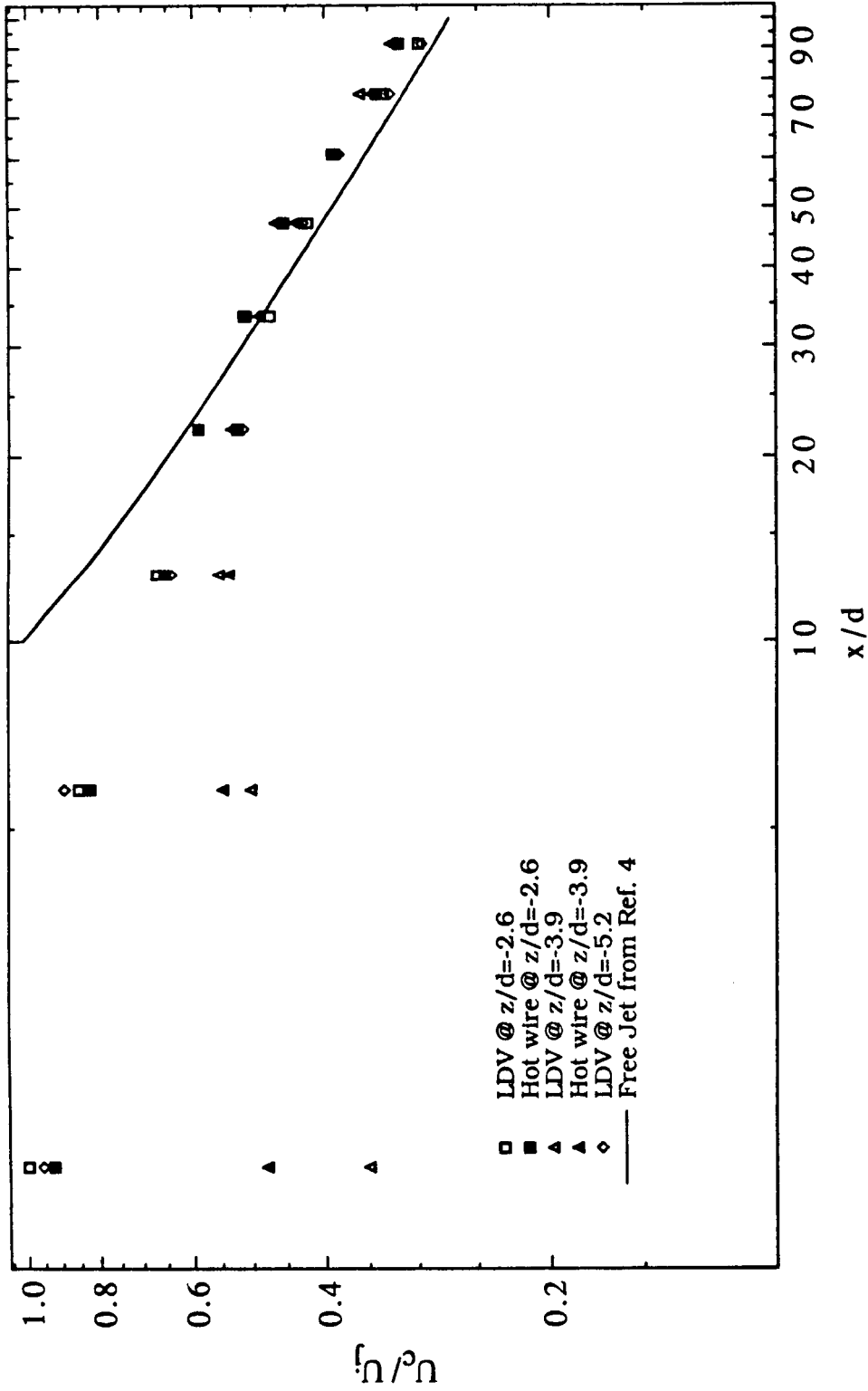


Figure 29: Centerline velocity results including free jet data from Ref. 4.

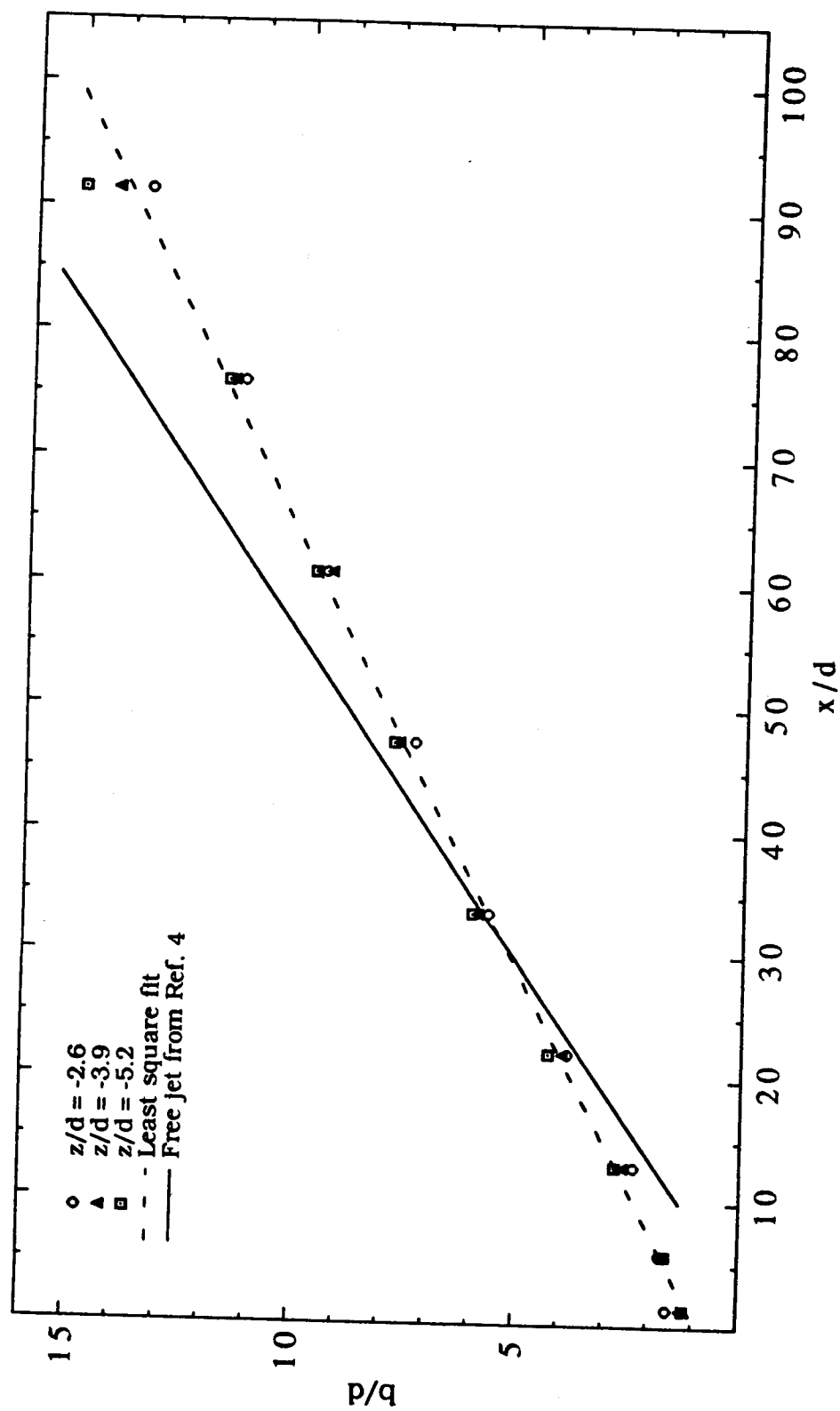


Figure 30: Evolution of the normalized jet width including free jet data from Ref. 4.

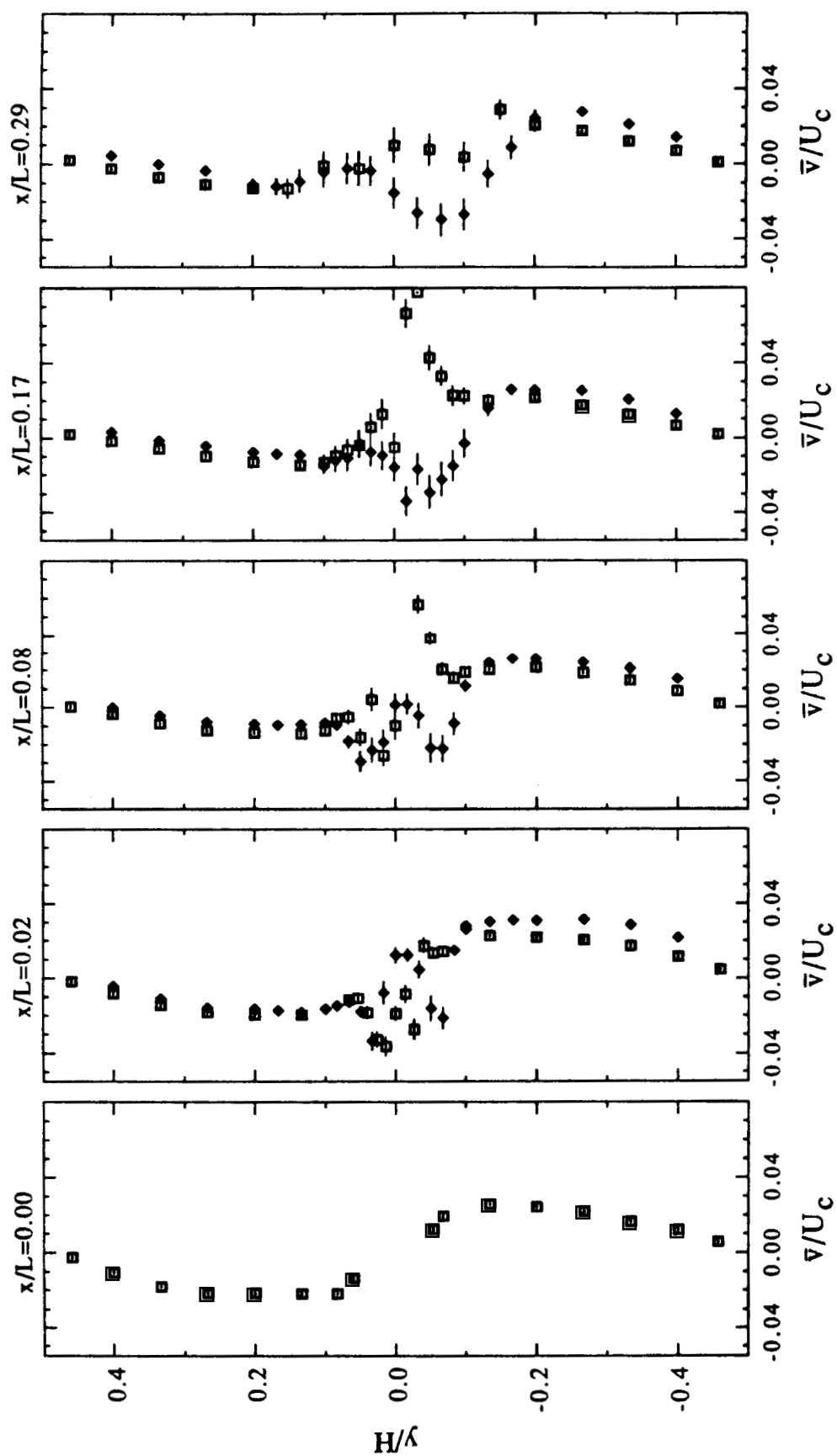


Figure 31: Transverse velocity profiles at $z/d = -2.6$ obtained by LDV (□) and hot wire anemometry (♦) for $0 \leq x/L \leq 0.29$.

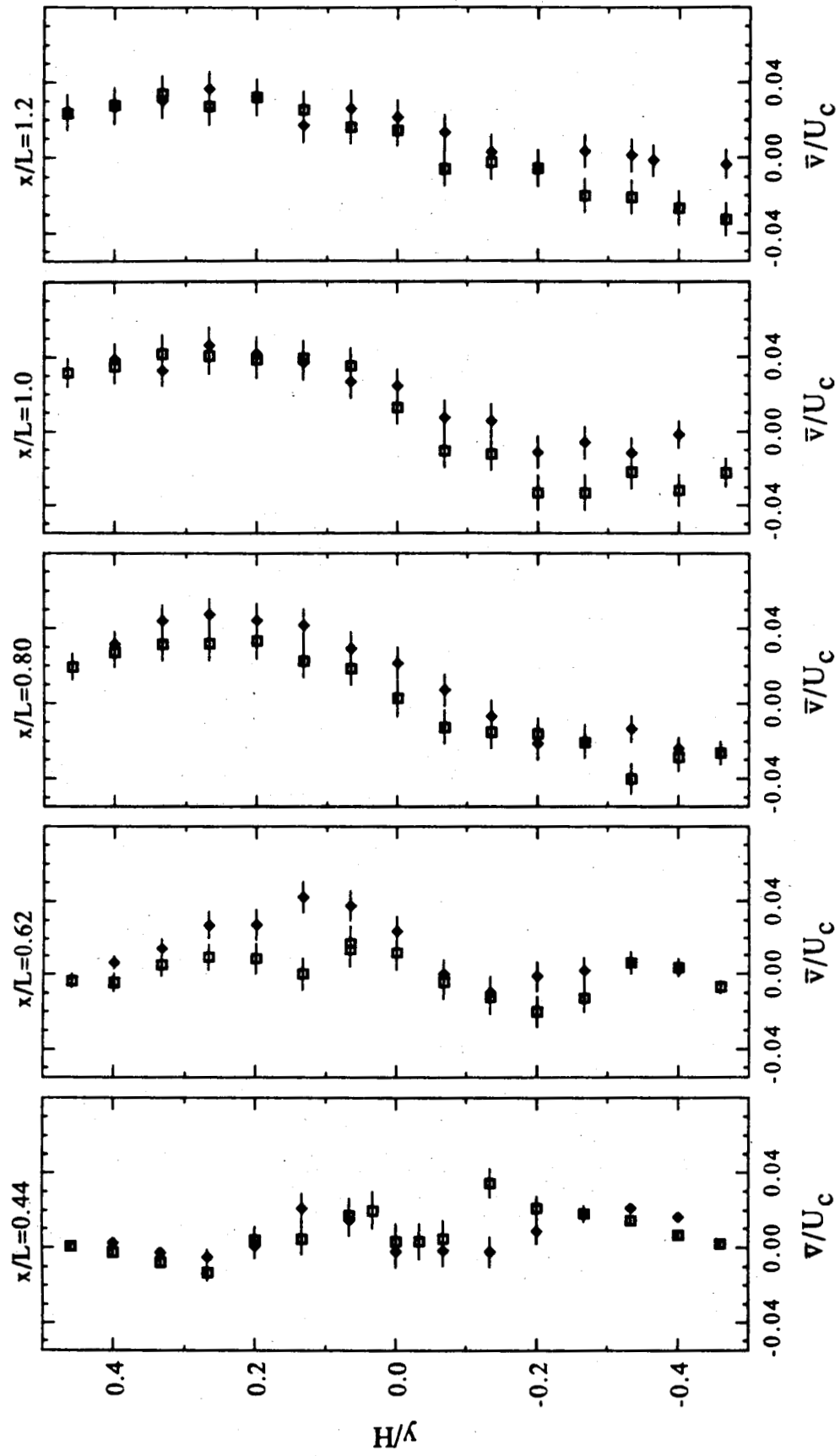


Figure 32: Transverse velocity profiles at $z/d = -2.6$ obtained by LDV (\square) and hot wire anemometry (\diamond) for $0.44 \leq x/L \leq 1.2$.

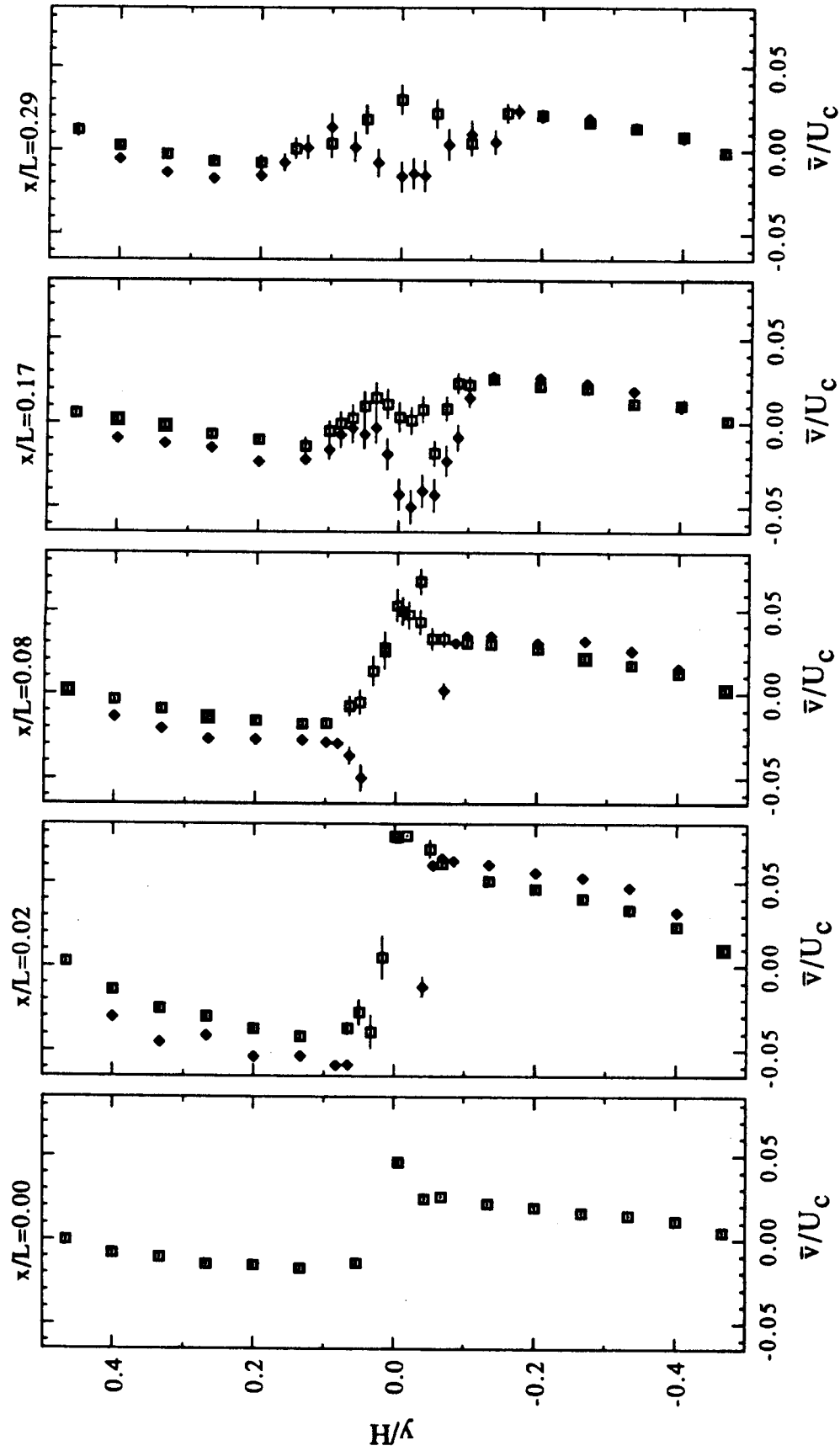


Figure 33: Transverse velocity profiles at $z/d = -3.9$ obtained by LDV (\blacksquare) and hot wire anemometry (\blacklozenge) for $0 \leq x/L \leq 0.29$.

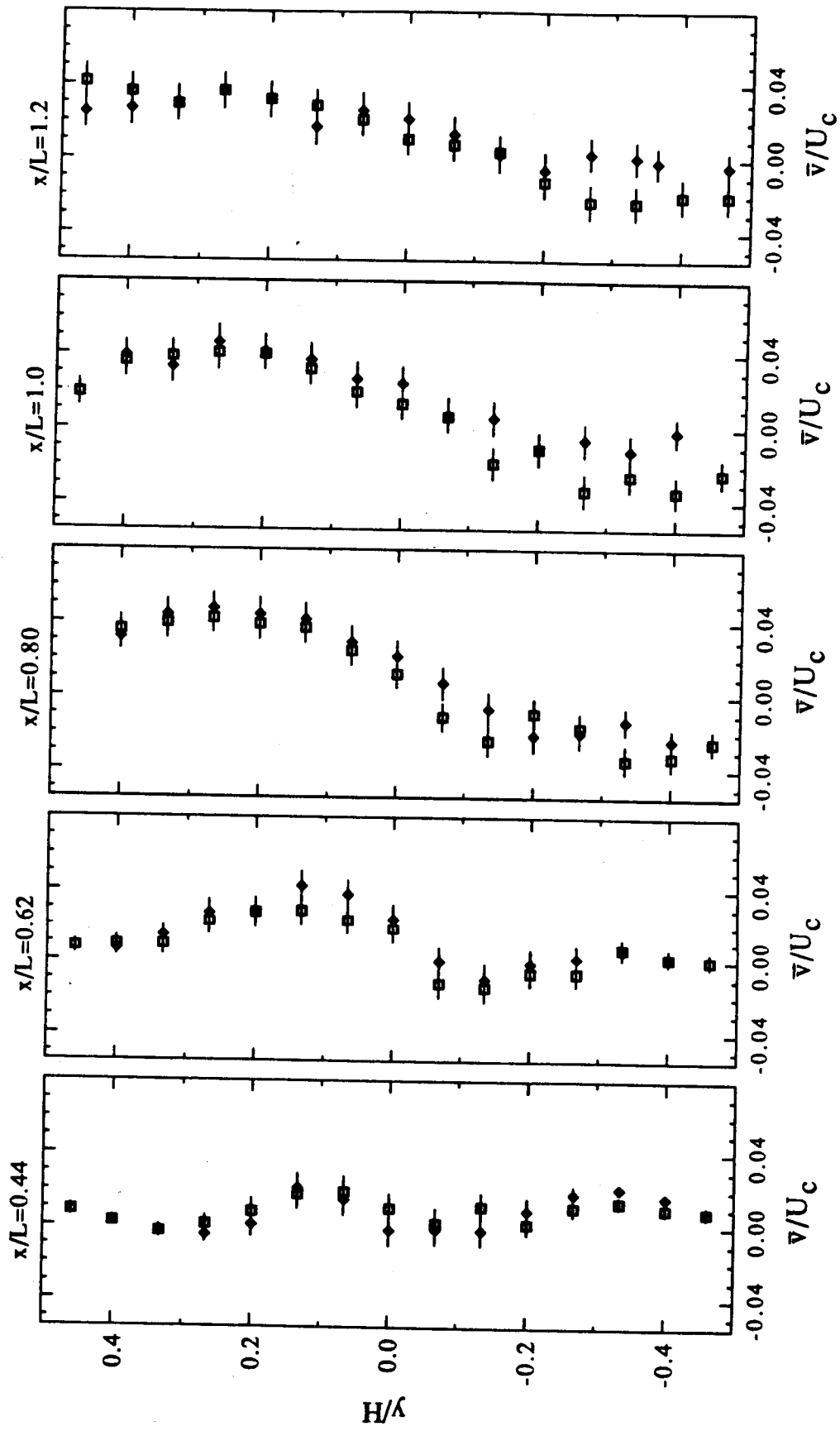


Figure 34: Transverse velocity profiles at $z/d = -3.9$ obtained by LDV (\square) and hot wire anemometry (\diamond) for $0.44 \leq x/L \leq 1.2$.

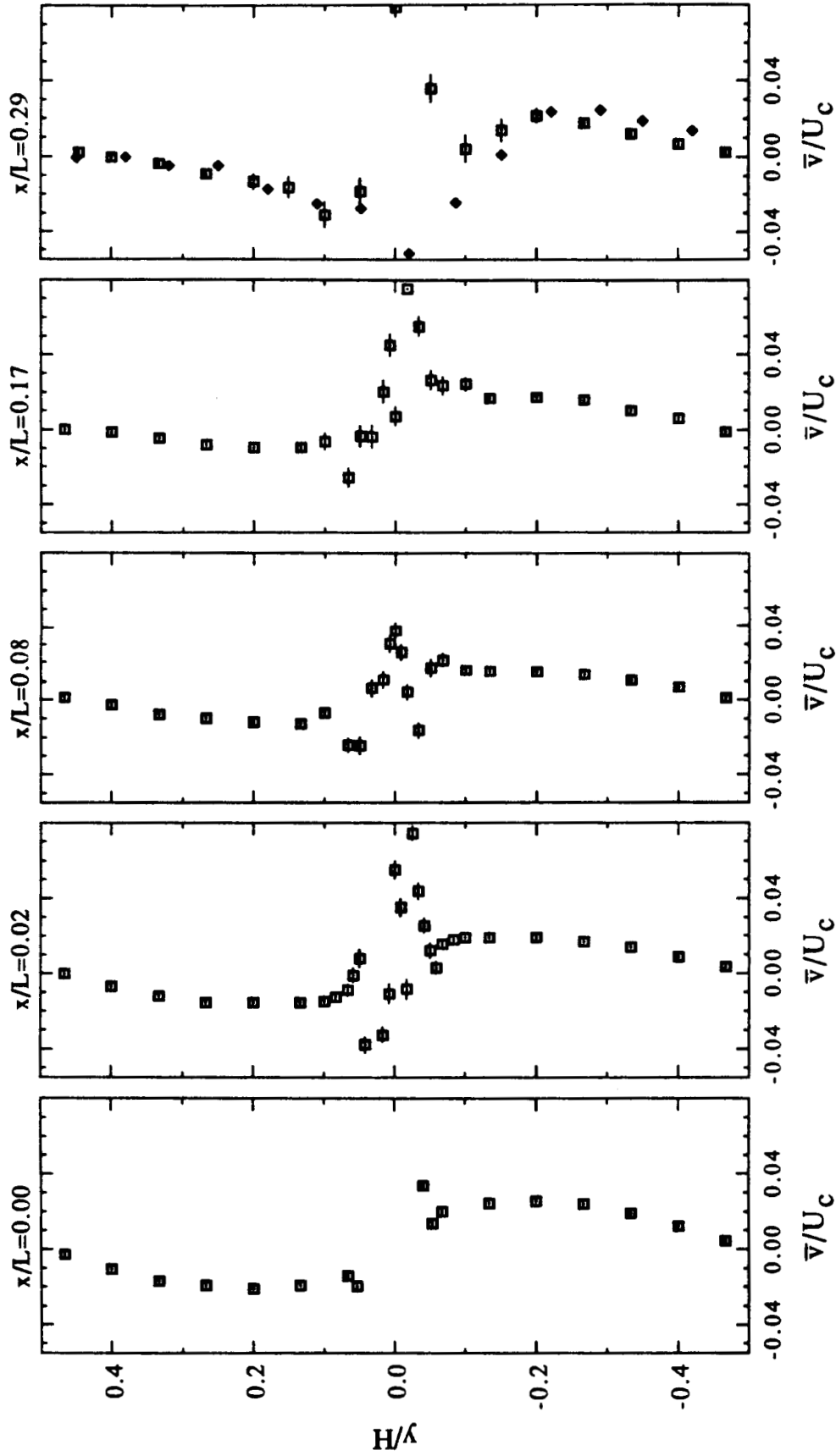


Figure 35: Transverse velocity profiles at $z/d = -5.2$ obtained by LDV (\square) and hot wire anemometry (\blacklozenge) for $0 \leq x/L \leq 0.29$.

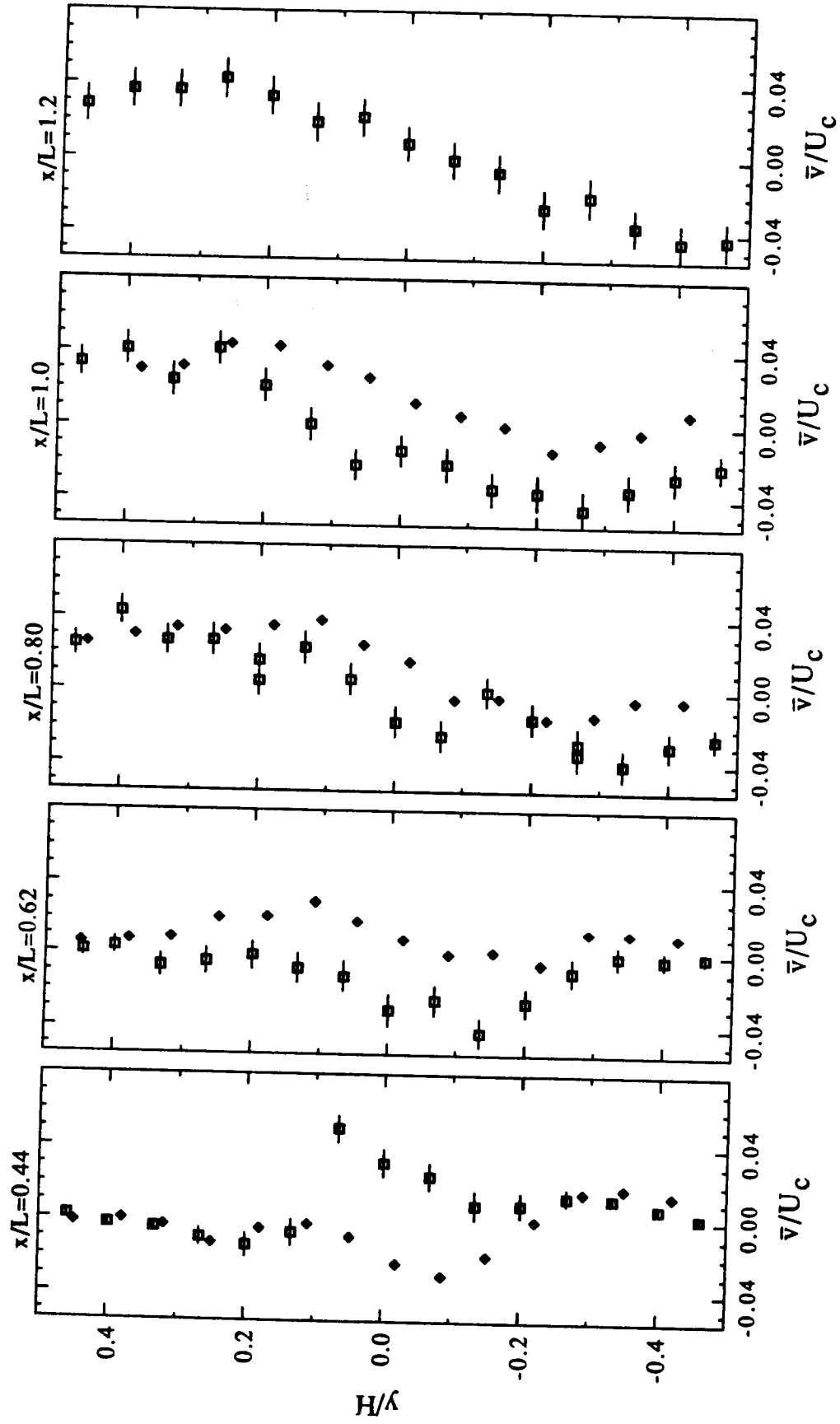


Figure 36: Transverse velocity profiles at $z/d = -5.2$ obtained by LDV (\square) and hot wire anemometry (\diamond) for $0.44 \leq x/L \leq 1.2$.

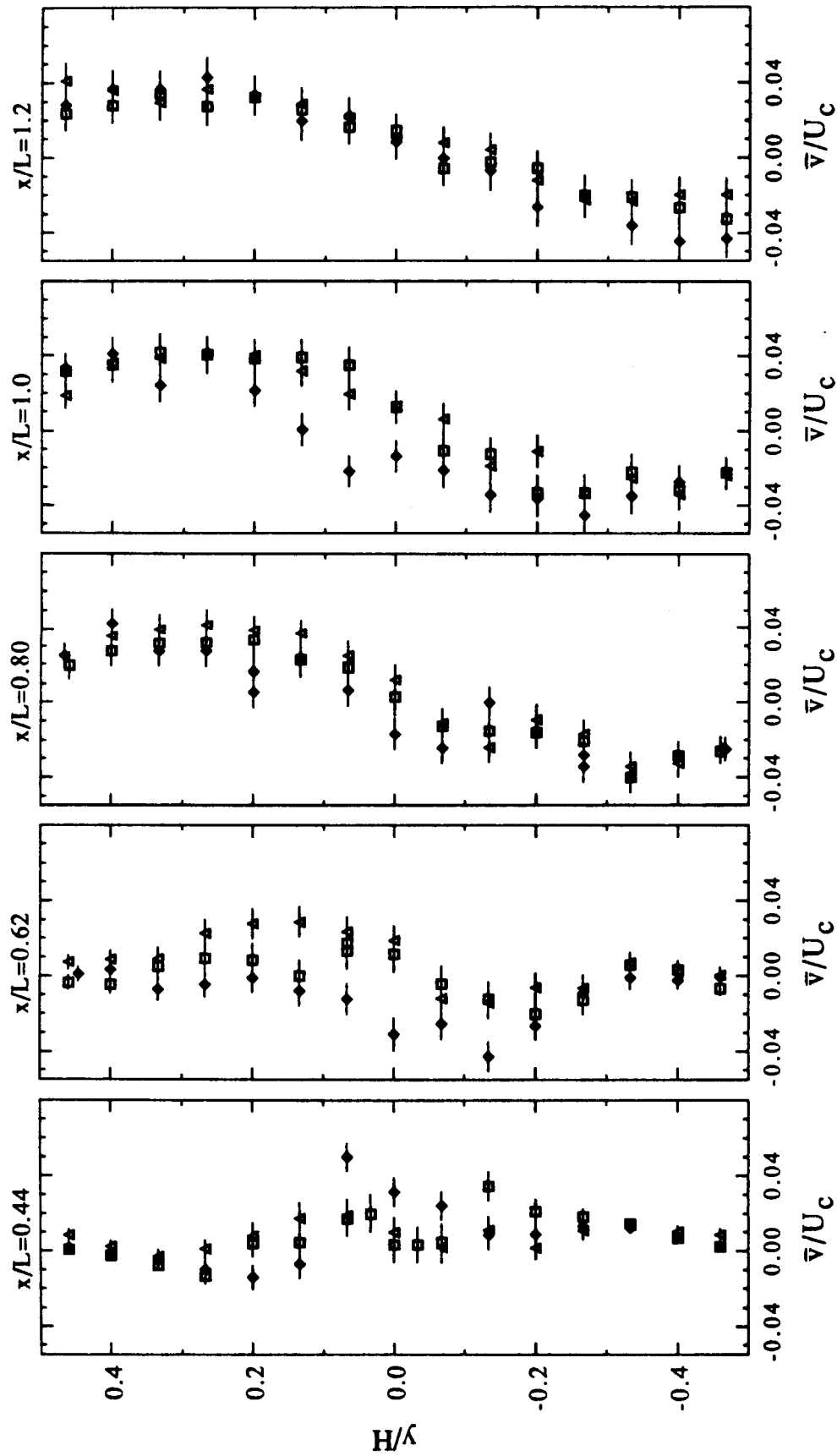


Figure 37: Transverse velocity profiles at $z/d = -2.6$ (\blacksquare), -3.9 (\blacktriangle), and -5.2 (\blacklozenge) obtained by LDV for $0.44 \leq x/L \leq 1.2$.

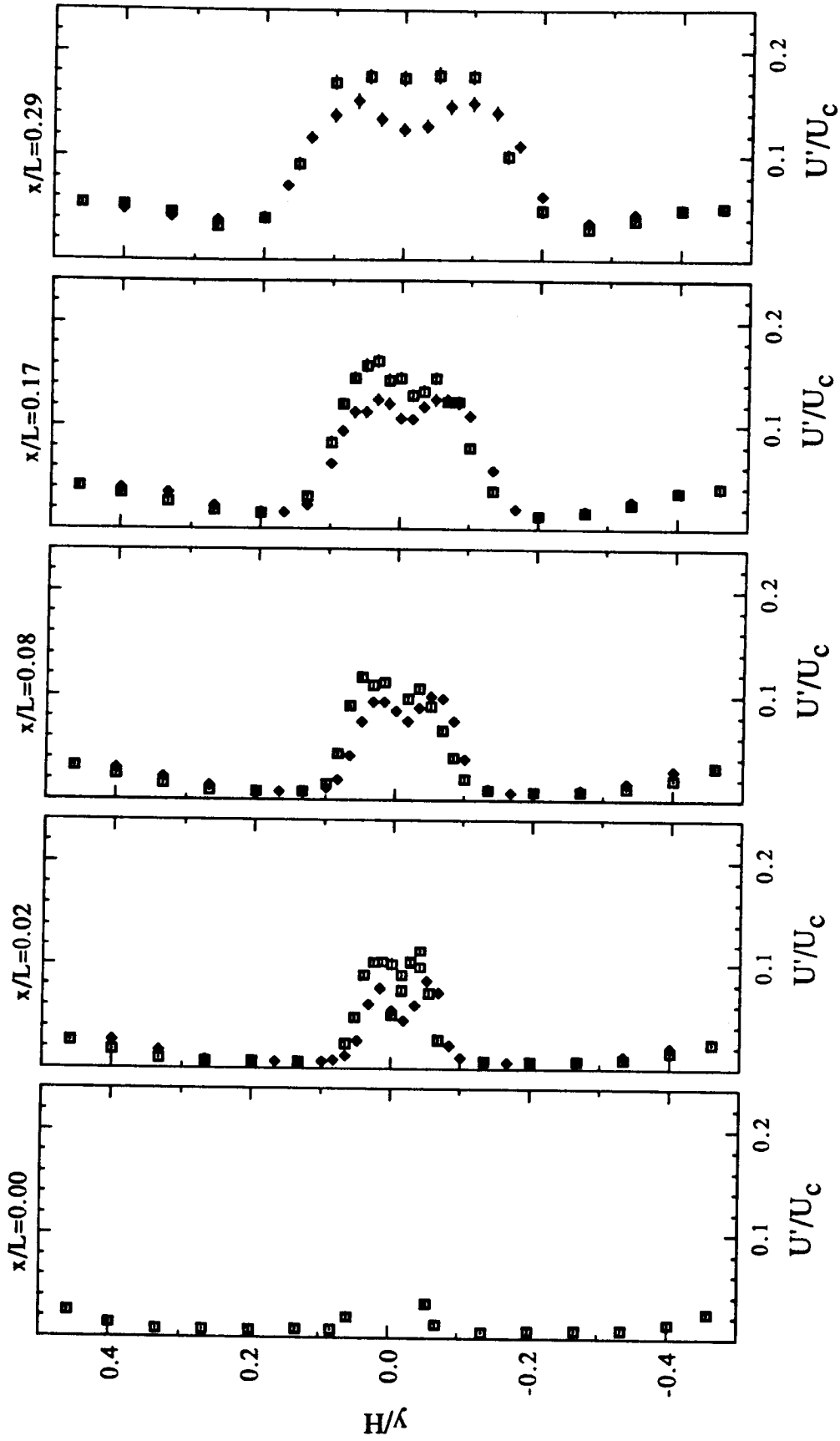


Figure 38: Axial turbulence intensity profiles at $z/d = -2.6$ obtained by LDV (\square) and hot wire anemometry (\diamond) for $0 \leq x/L \leq 0.29$.

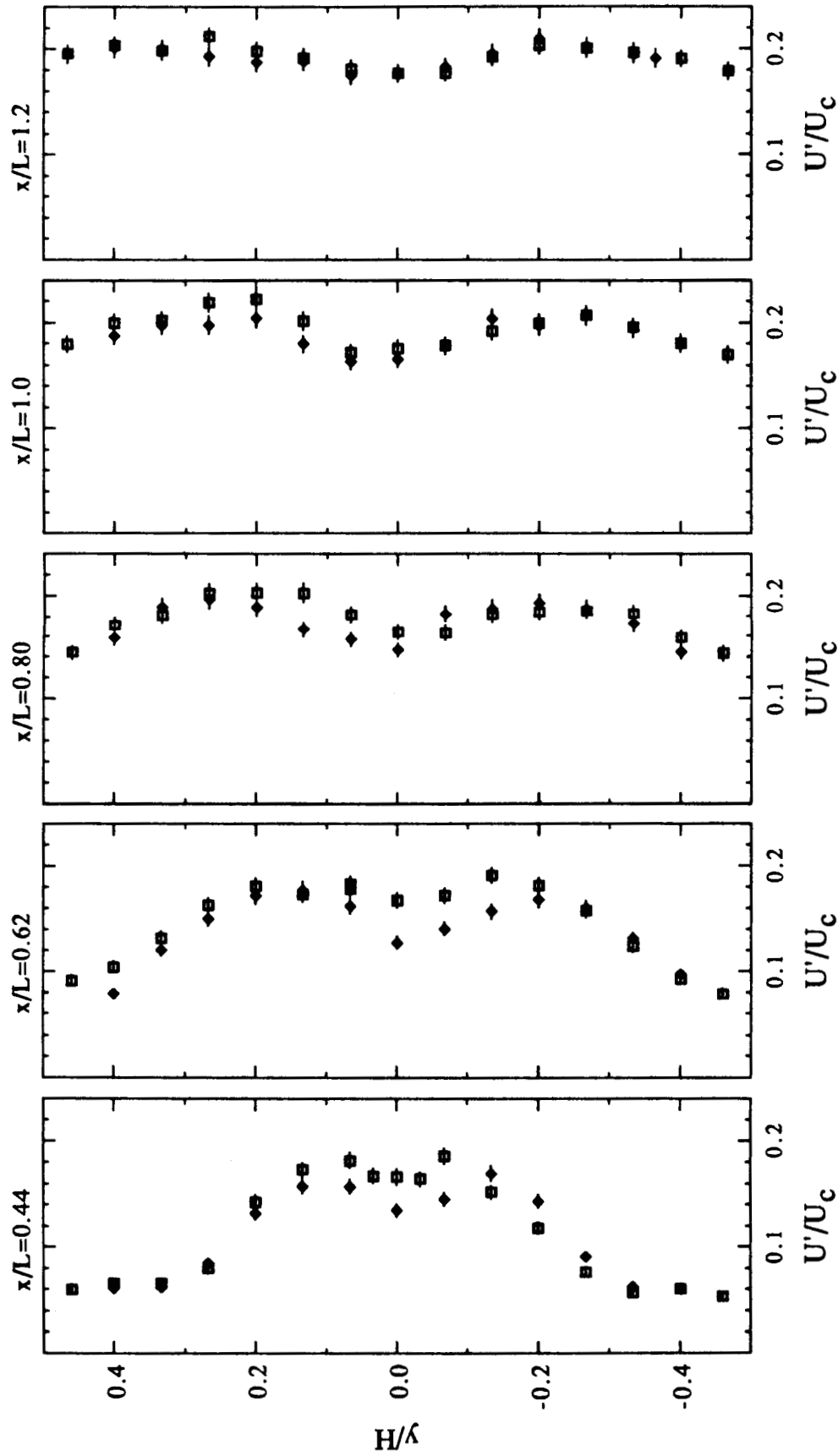


Figure 39: Axial turbulence intensity profiles at $z/d = -2.6$ obtained by LDV (□) and hot wire anemometry (♦) for $0.44 \leq x/L \leq 1.2$.

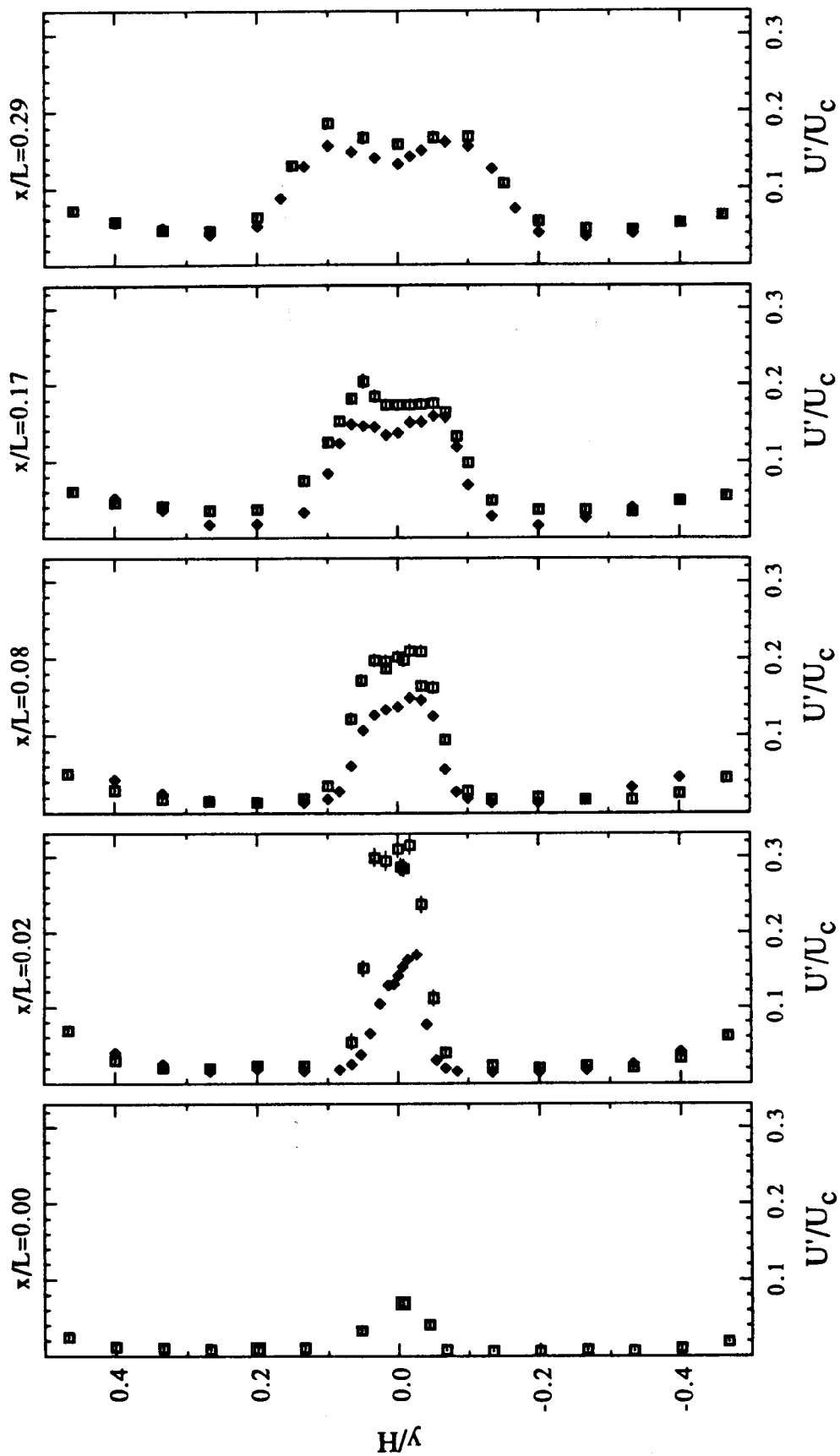


Figure 40: Axial turbulence intensity profiles at $z/d = -3.9$ obtained by LDV (■) and hot wire anemometry (◆) for $0 \leq x/L \leq 0.29$.

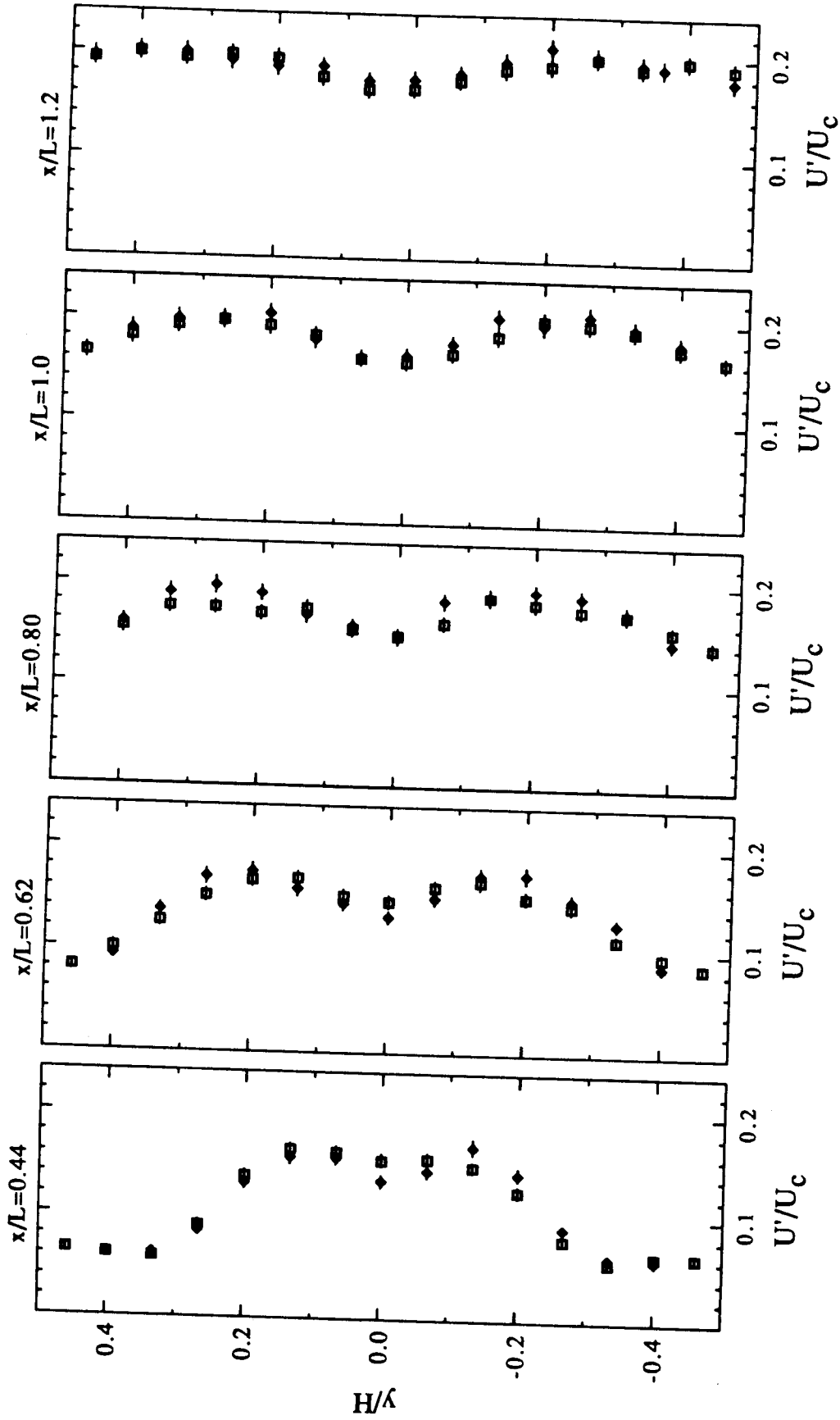


Figure 41: Axial turbulence intensity profiles at $z/d = -3.9$ obtained by LDV (\square) and hot wire anemometry (\diamond) for $0.44 \leq x/L \leq 1.2$.

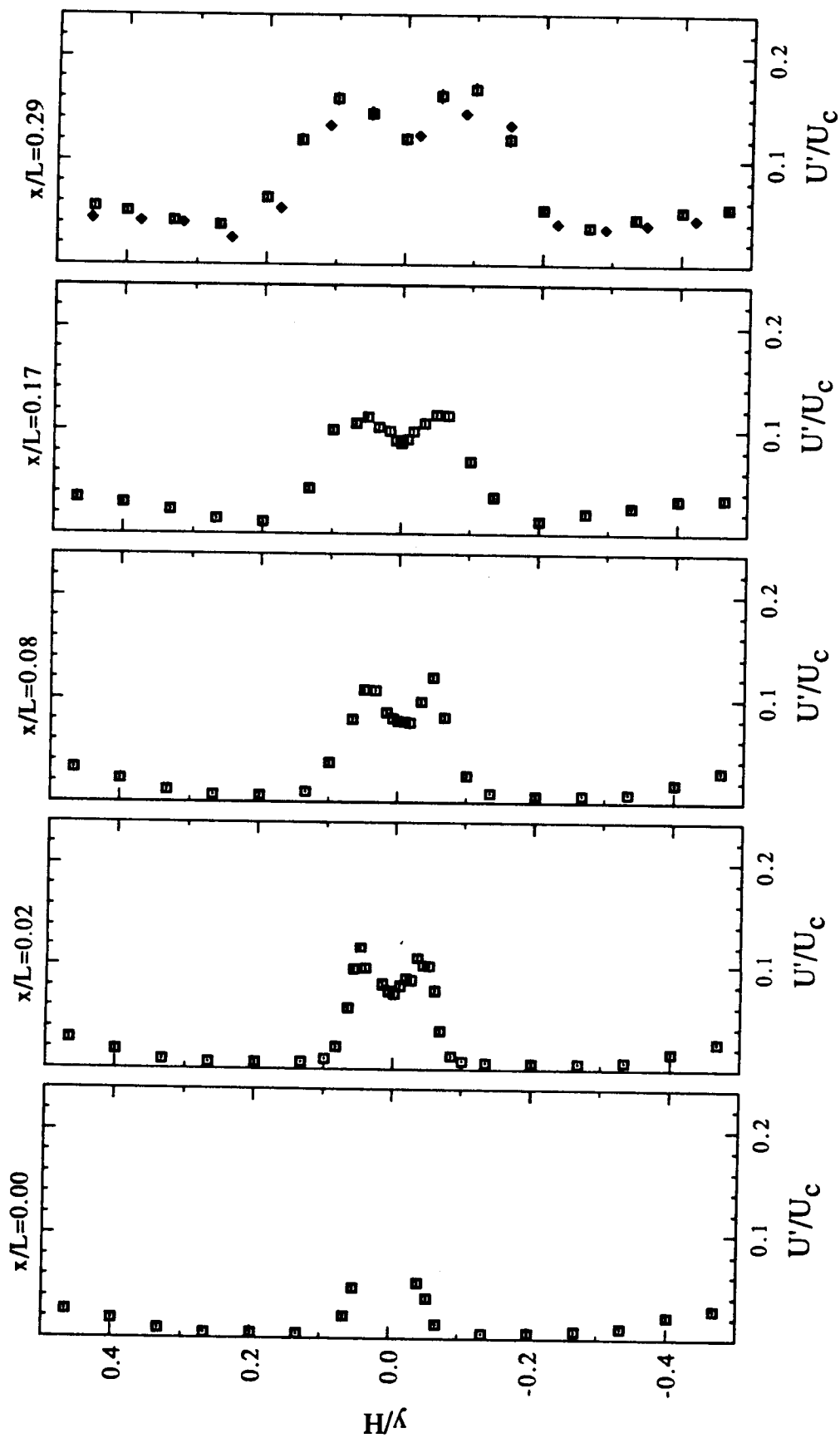


Figure 42: Axial turbulence intensity profiles at $z/d = -5.2$ obtained by LDV (\square) and hot wire anemometry (\diamond) for $0 \leq x/L \leq 0.29$.

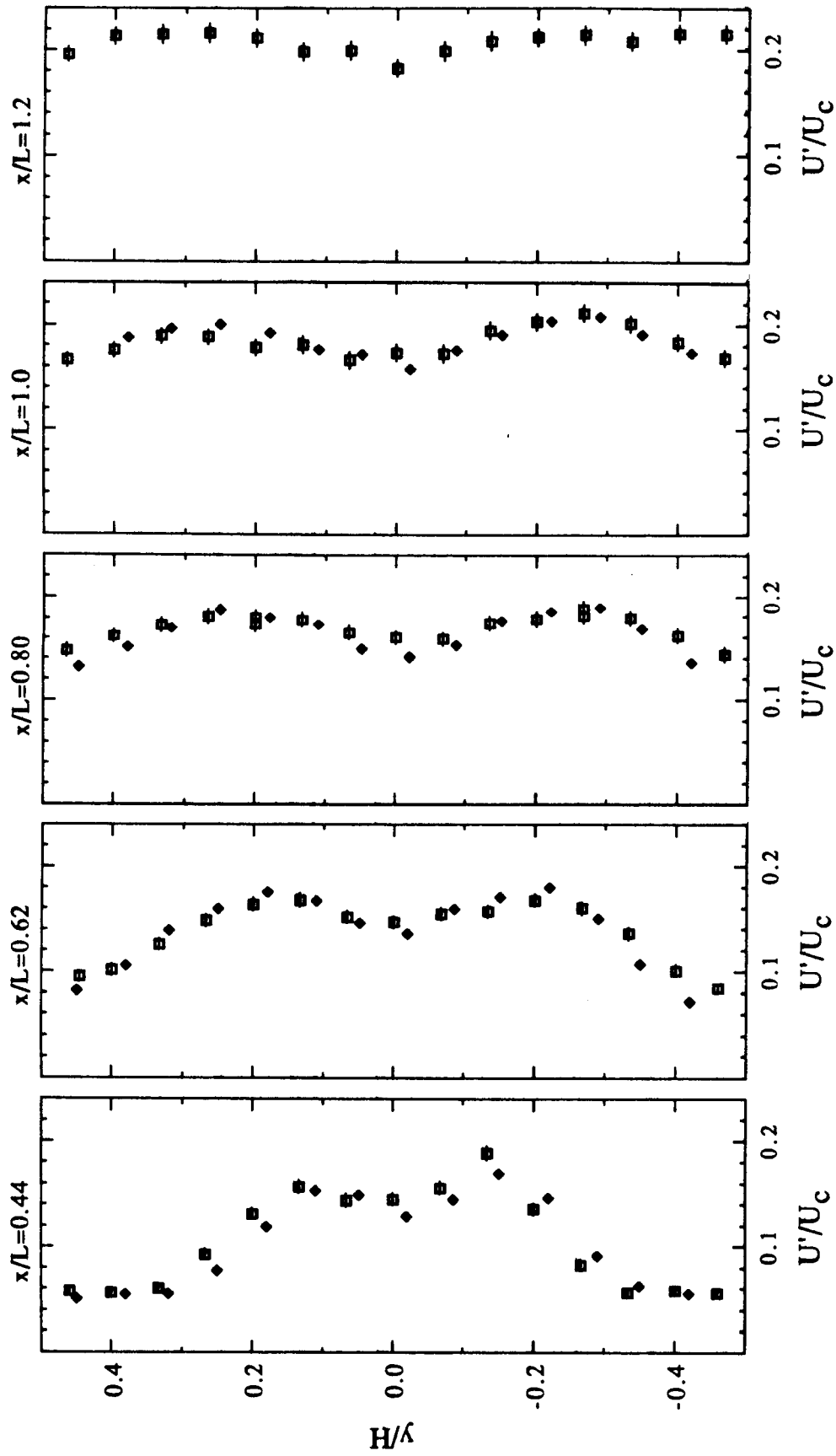


Figure 43: Axial turbulence intensity profiles at $z/d = -5.2$ obtained by LDV (□) and hot wire anemometry (♦) for $0.44 \leq x/L \leq 1.2$.

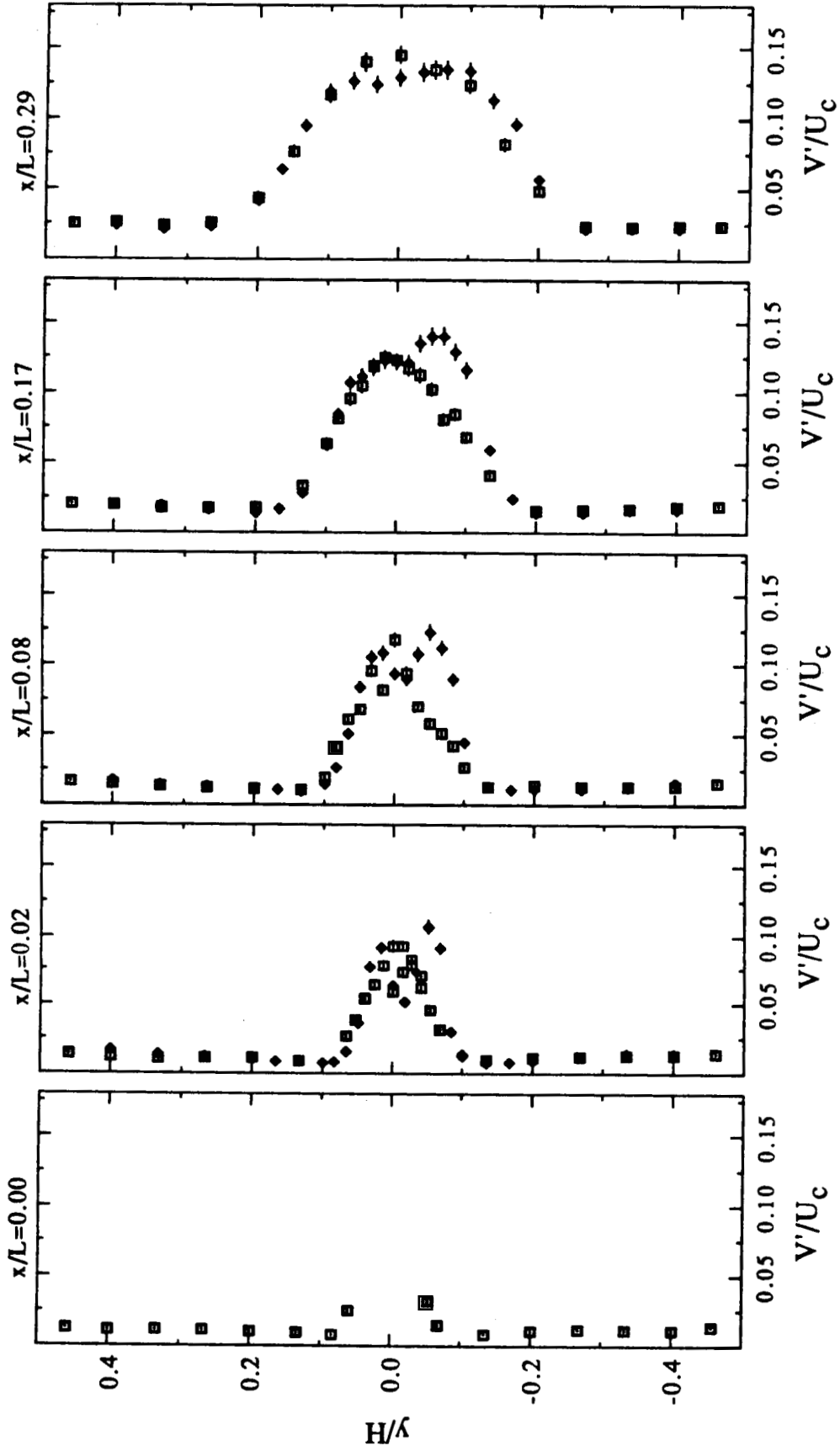


Figure 44: Transverse turbulence intensity profiles at $z/d = -2.6$ obtained by LDV (■) and hot wire anemometry (♦) for $0 \leq x/L \leq 0.29$.

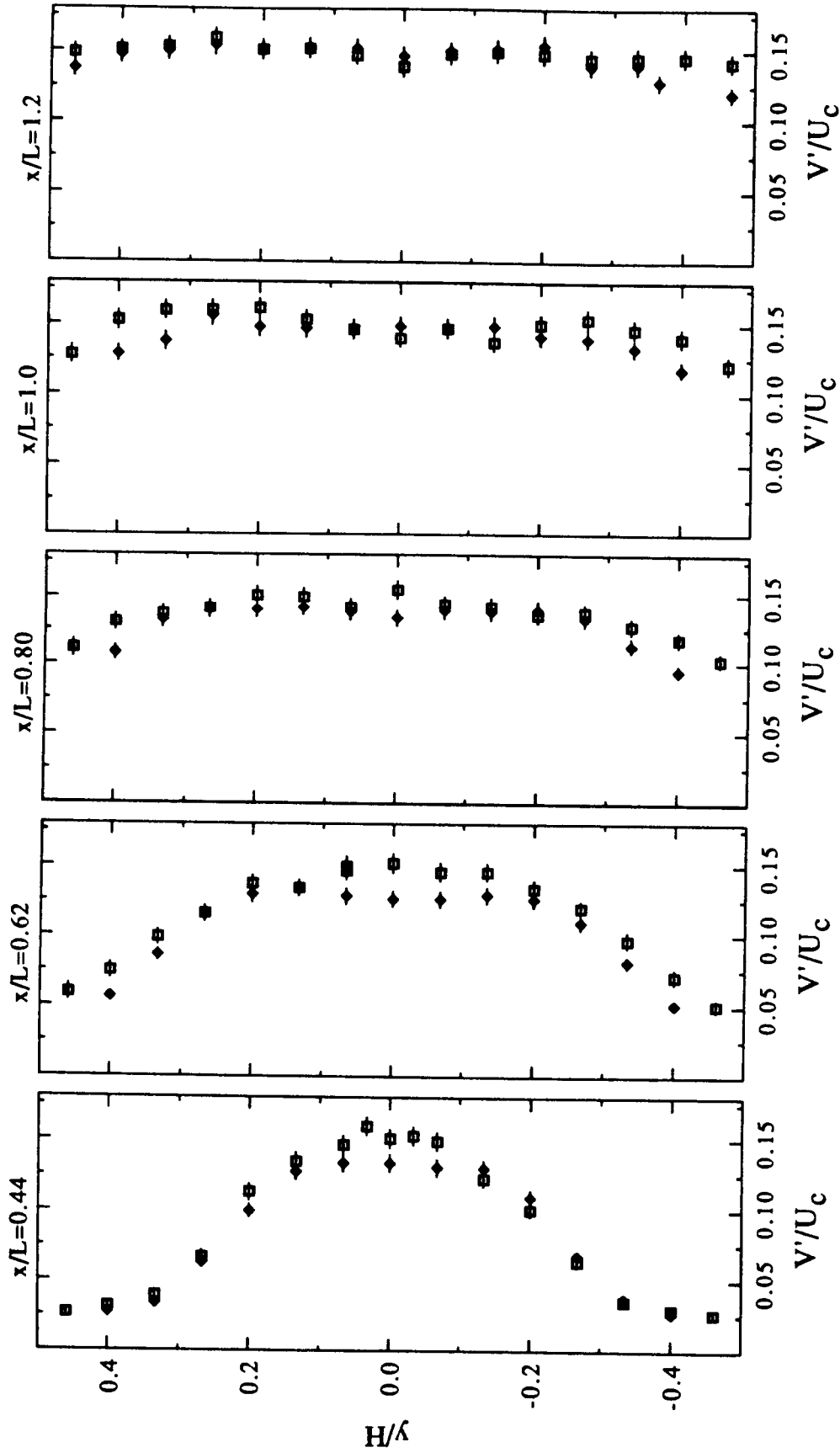


Figure 45: Transverse turbulence intensity profiles at $z/d = -2.6$ obtained by LDV (\square) and hot wire anemometry (\diamond) for $0.44 \leq x/L \leq 1.2$.

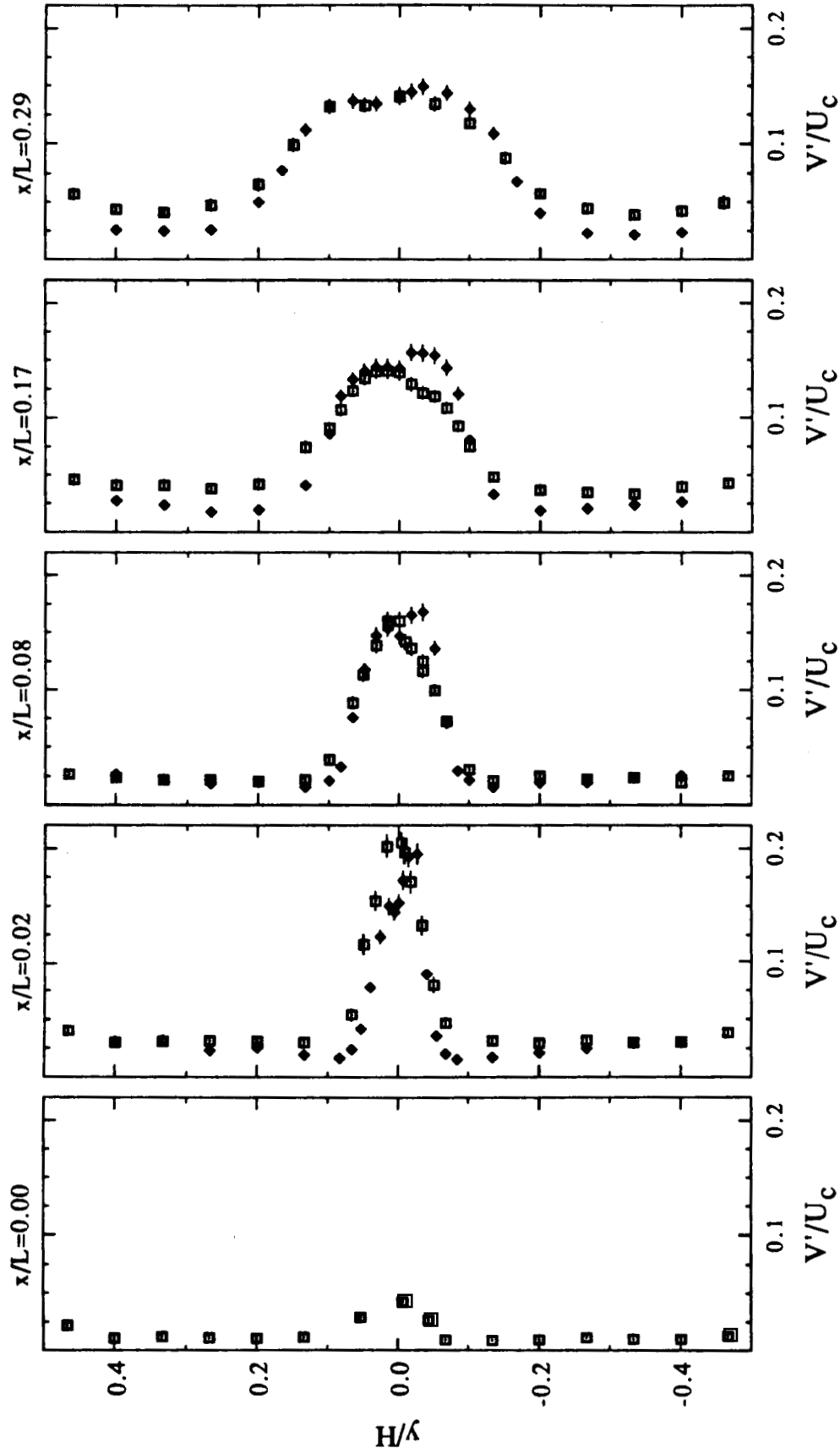


Figure 46: Transverse turbulence intensity profiles at $z/d = -3.9$ obtained by LDV (\square) and hot wire anemometry (\diamond) for $0 \leq x/L \leq 0.29$.

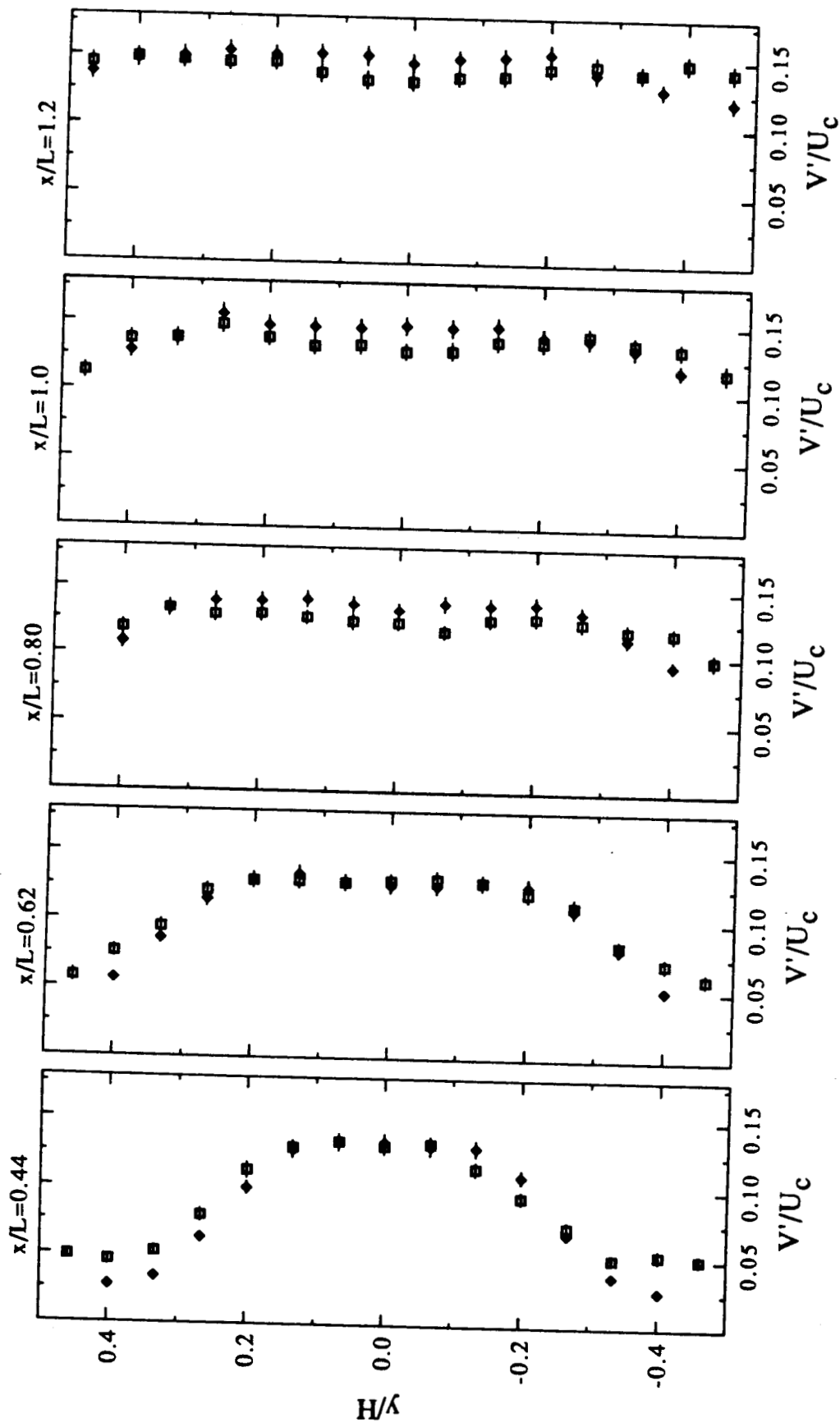


Figure 47: Transverse turbulence intensity profiles at $z/d = -3.9$ obtained by LDV (\square) and hot wire anemometry (\diamond) for $0.44 \leq x/L \leq 1.2$.

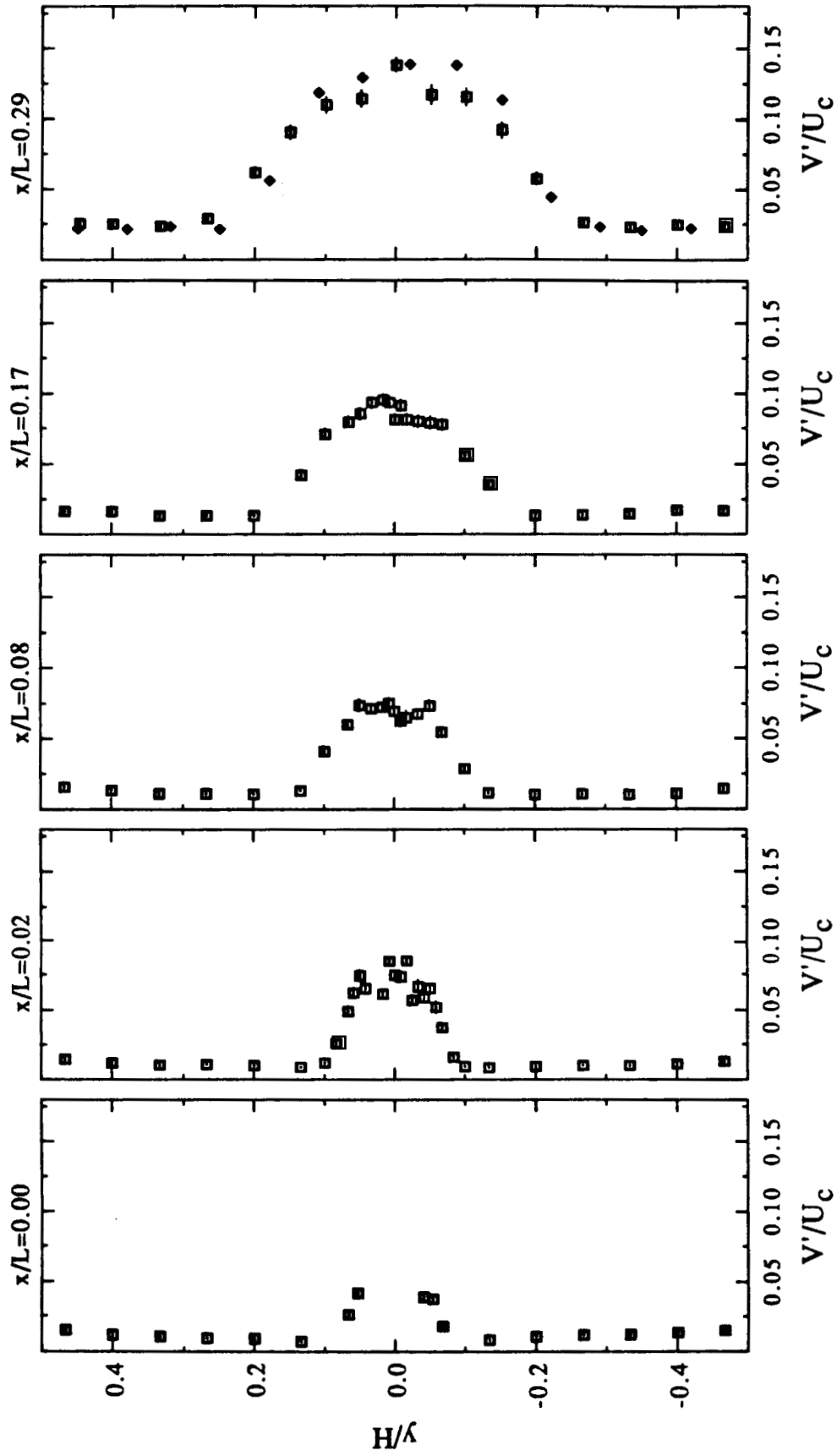


Figure 48: Transverse turbulence intensity profiles at $z/d = -5.2$ obtained by LDV (\square) and hot wire anemometry (\blacklozenge) for $0 \leq x/L \leq 0.29$.

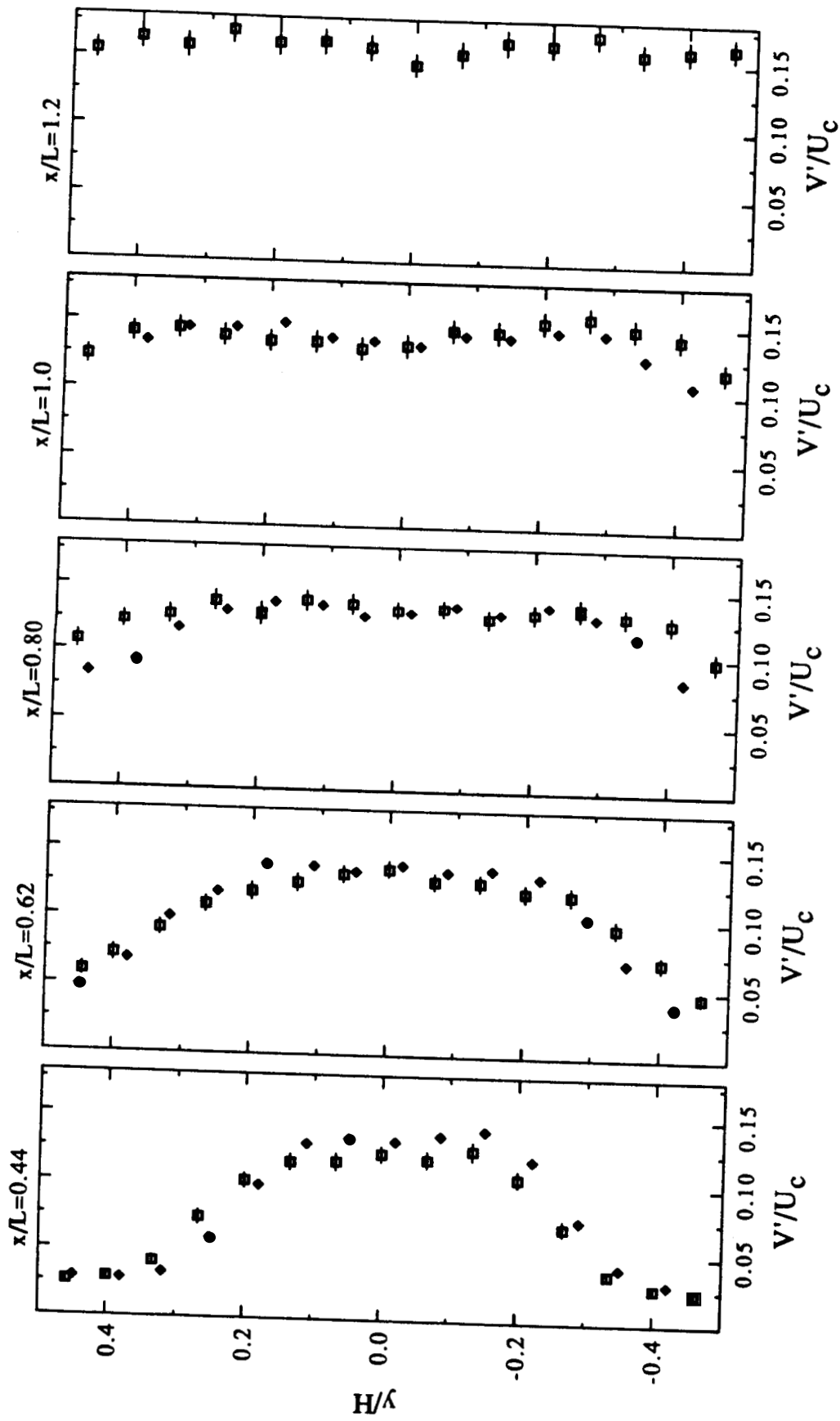


Figure 49: Transverse turbulence intensity profiles at $z/d = -5.2$ obtained by LDV (\square) and hot wire anemometry (\diamond) for $0.44 \leq x/L \leq 1.2$.

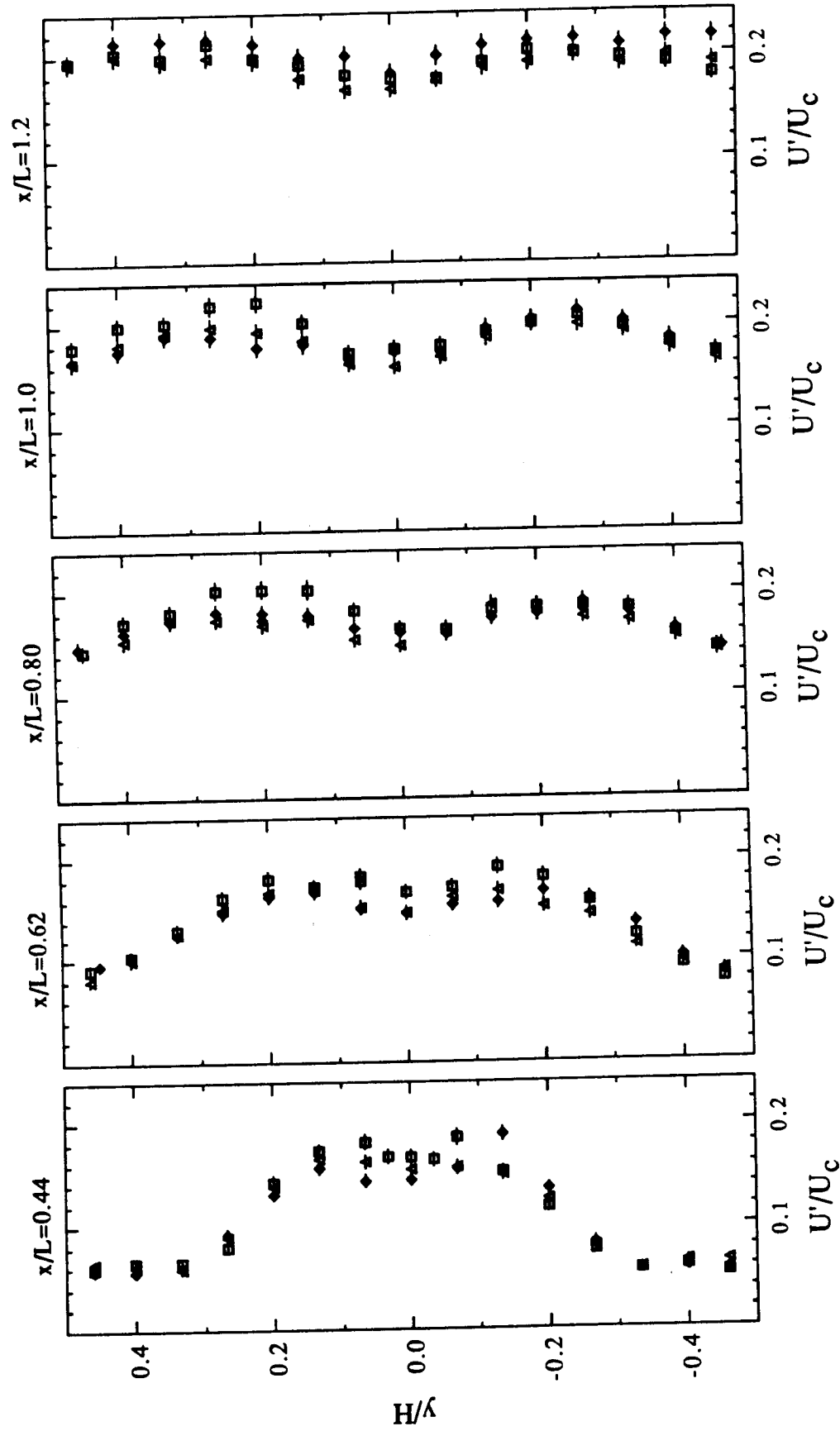


Figure 50: Axial turbulence intensity profiles at $z/d = -2.6$ (\blacksquare), -3.9 (\blacktriangle), and -5.2 (\blacklozenge) obtained by LDV for $0.44 \leq x/L \leq 1.2$.

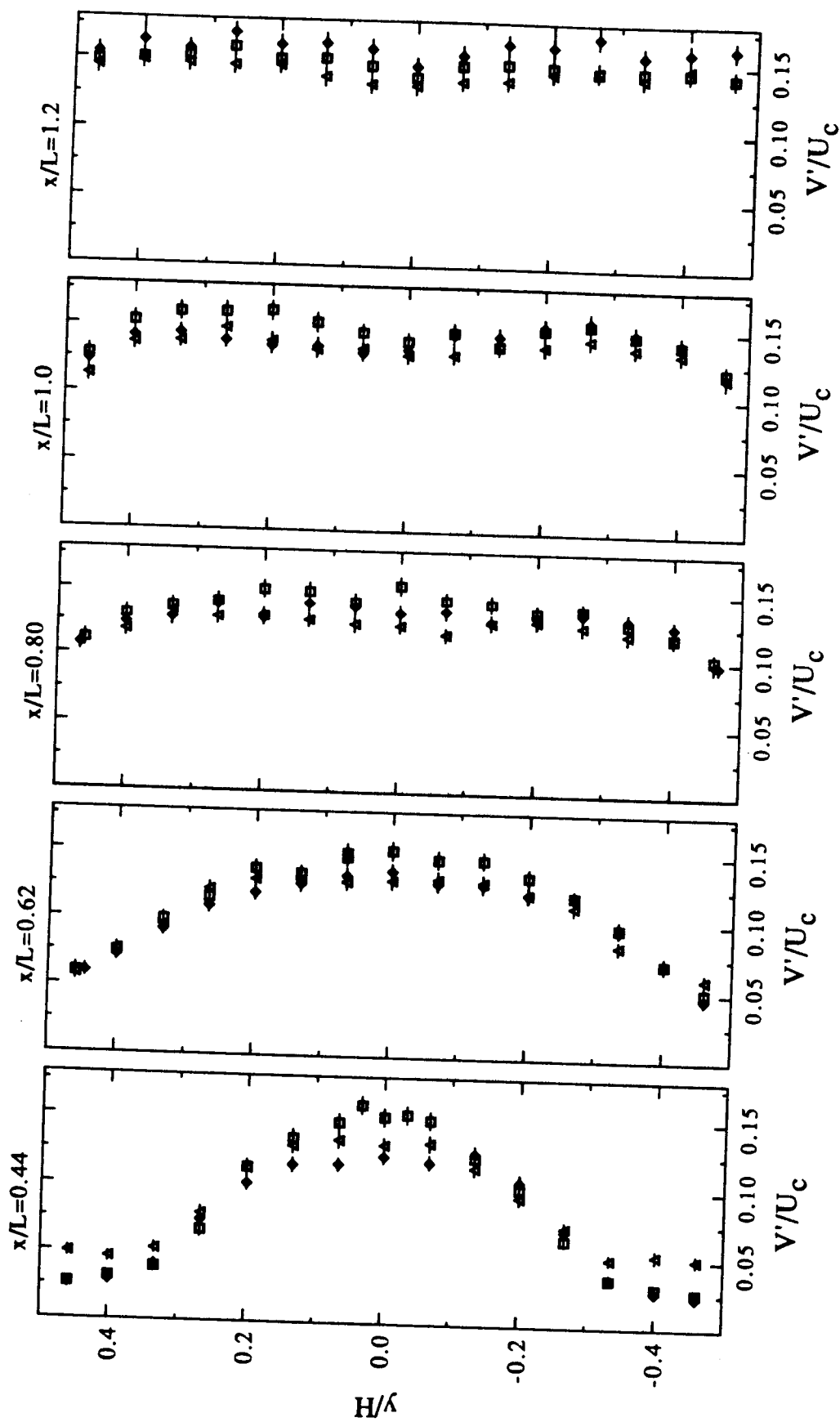


Figure 51: Transverse turbulence intensity profiles at $z/d = -2.6$ (◻), -3.9 (◻), and -5.2 (◈) obtained by LDV for $0.44 \leq x/L \leq 1.2$.

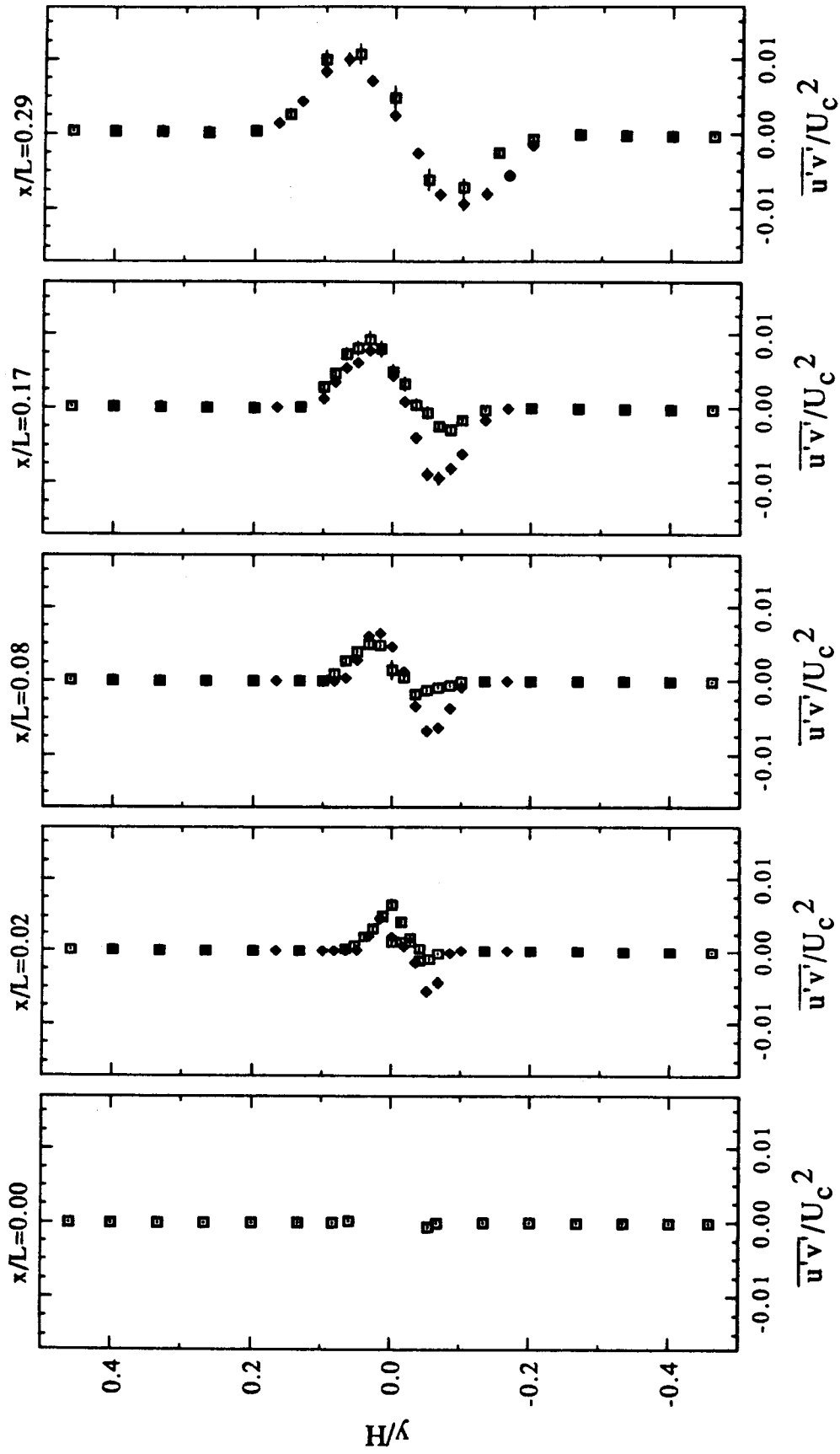


Figure 52: U-V Reynolds stress profiles at $z/d = -2.6$ obtained by LDV (\square) and hot wire anemometry (\diamond) for $0 \leq x/L \leq 0.29$.

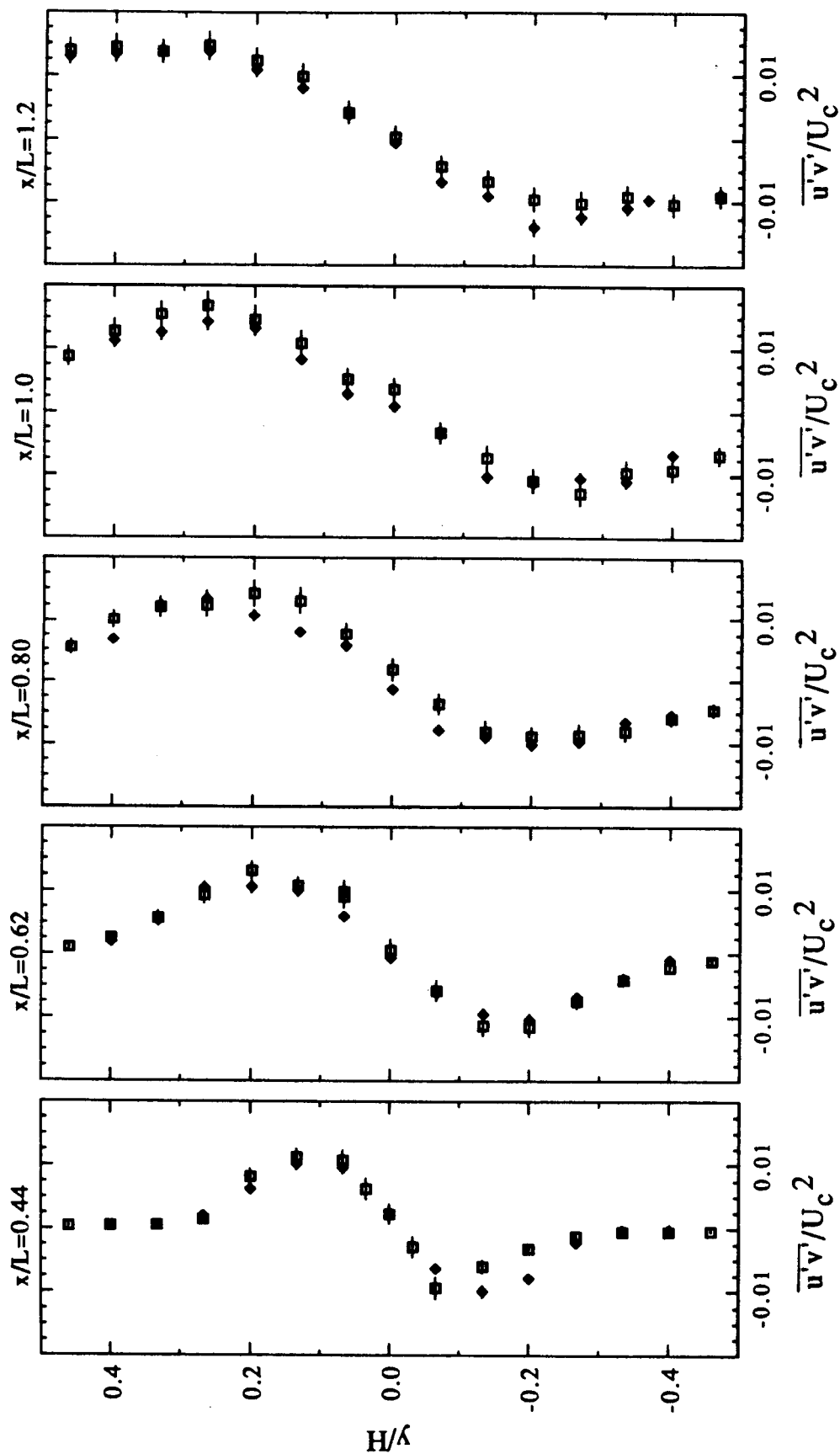


Figure 53: U-V Reynolds stress profiles at $z/d = -2.6$ obtained by LDV (□) and hot wire anemometry (♦) for $0.44 \leq x/L \leq 1.2$.

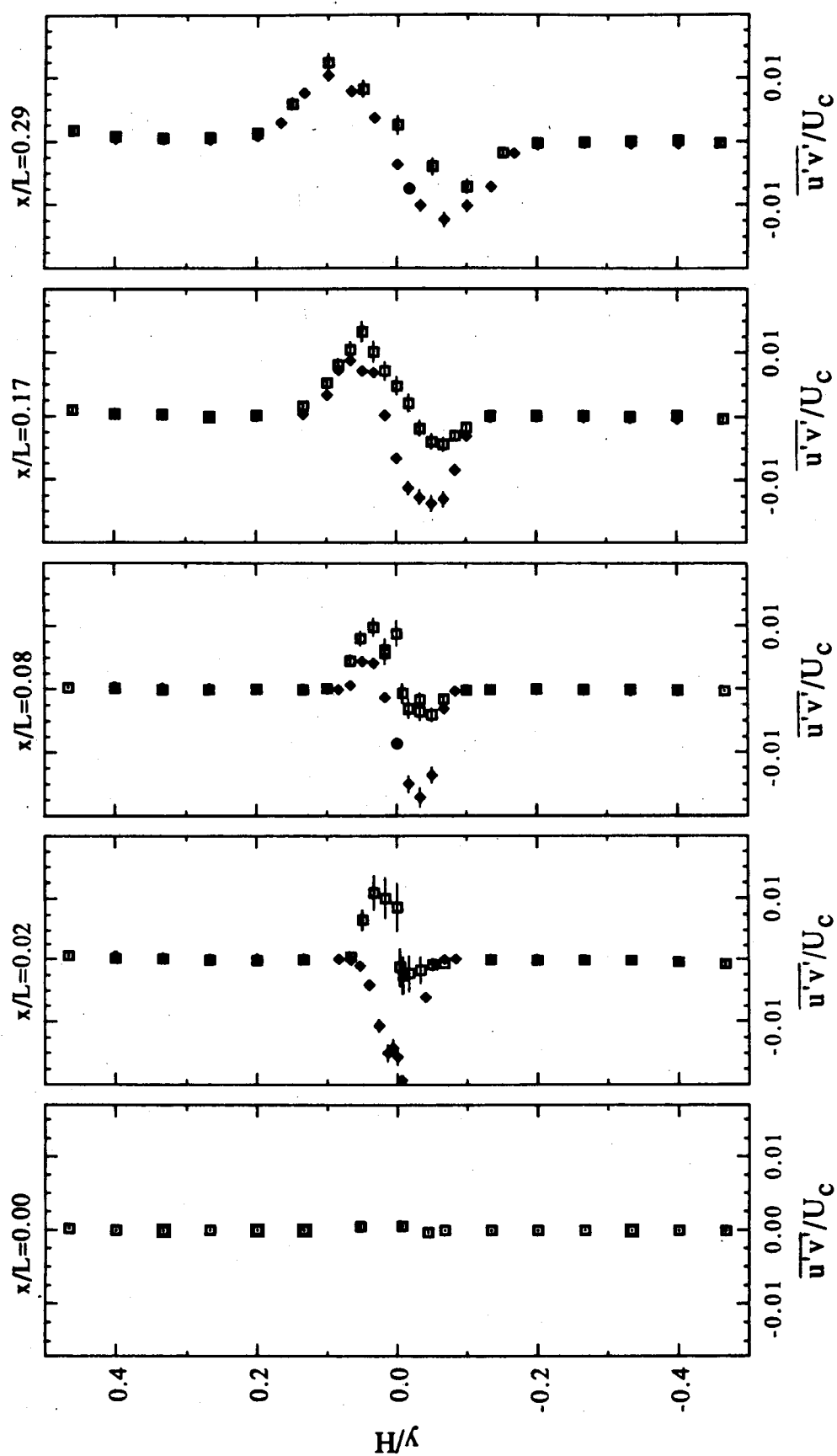


Figure 54: U-V Reynolds stress profiles at $z/d = -3.9$ obtained by LDV (\square) and hot wire anemometry (\diamond) for $0 \leq x/L \leq 0.29$.

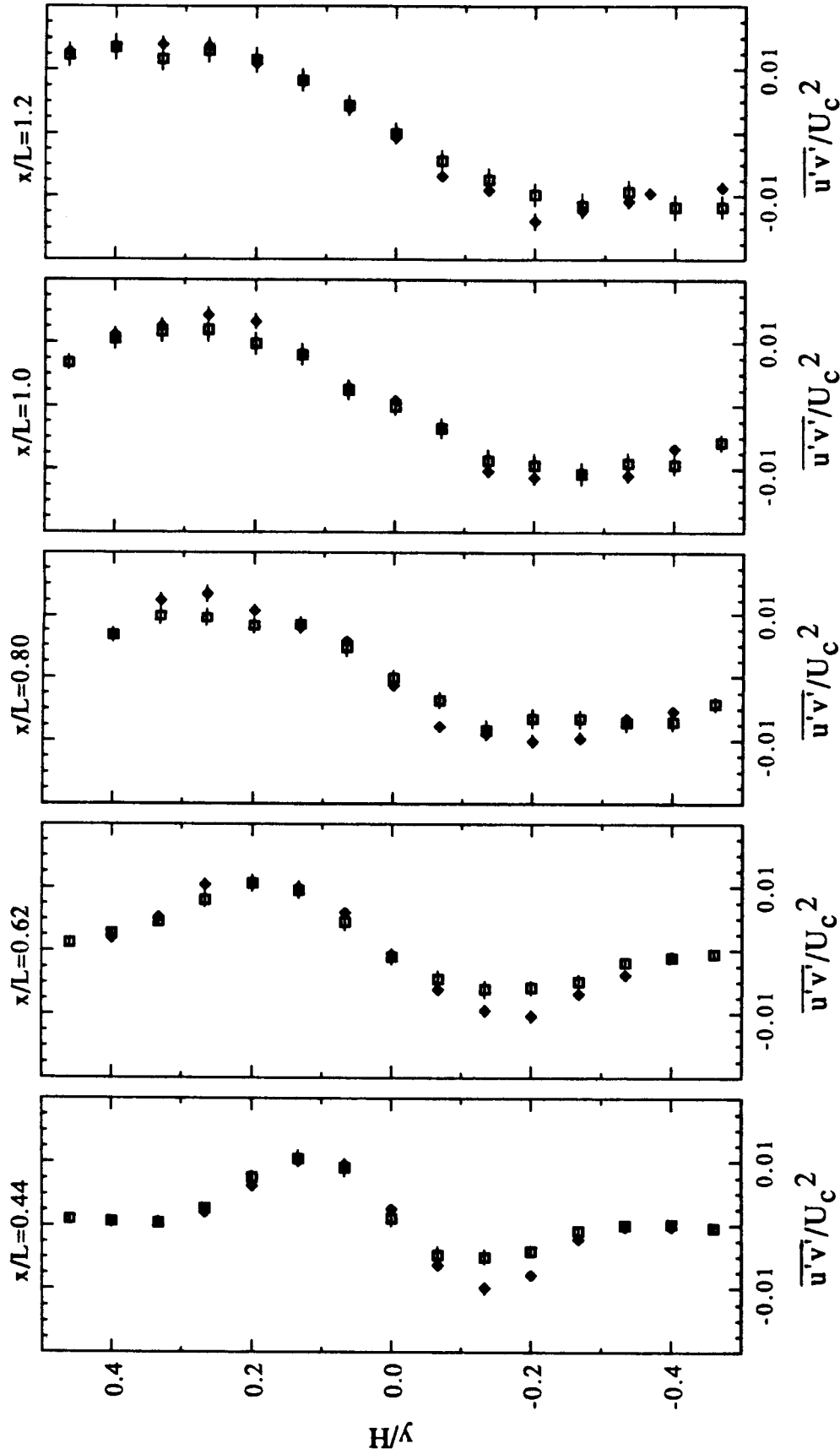


Figure 55: U-V Reynolds stress profiles at $z/d = -3.9$ obtained by LDV (■) and hot wire anemometry (◆) for $0.44 \leq x/L \leq 1.2$.

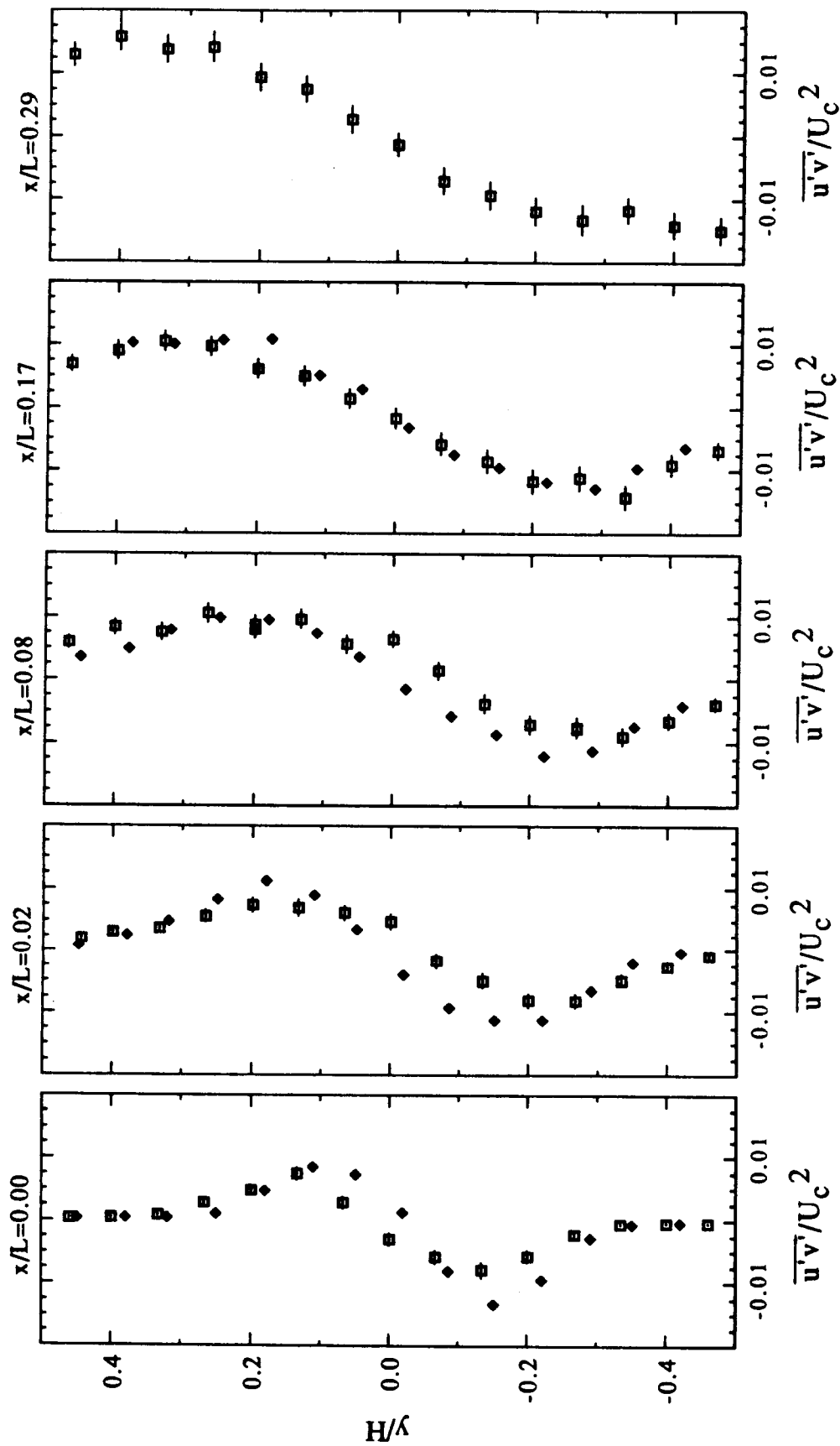


Figure 56: U-V Reynolds stress profiles at $z/d = -5.2$ obtained by LDV (\square) and hot wire anemometry (\diamond) for $0 \leq x/L \leq 0.29$.

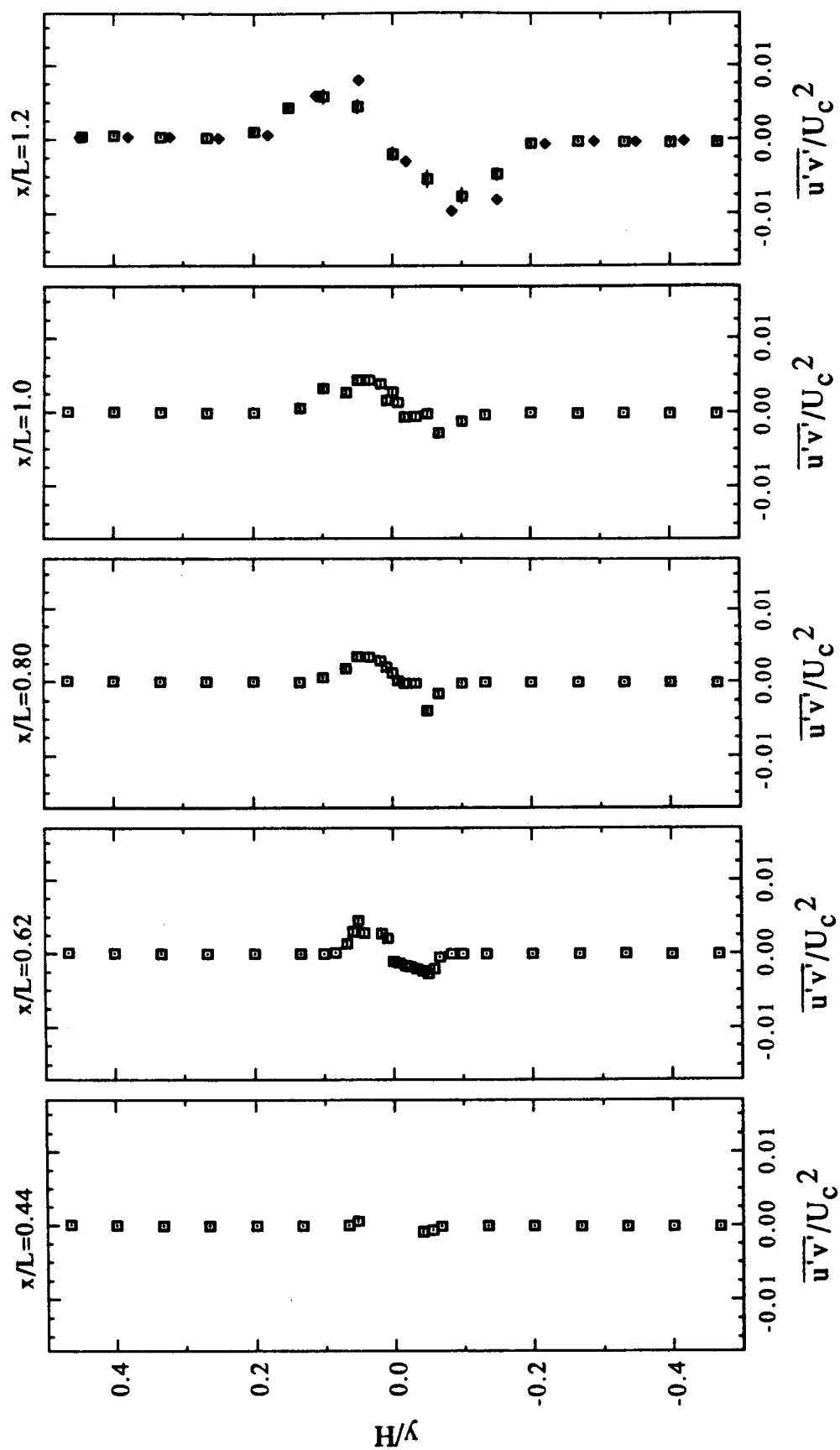


Figure 57: U-V Reynolds stress profiles at $z/d = -5.2$ obtained by LDV (□) and hot wire anemometry (♦) for $0.44 \leq x/L \leq 1.2$.

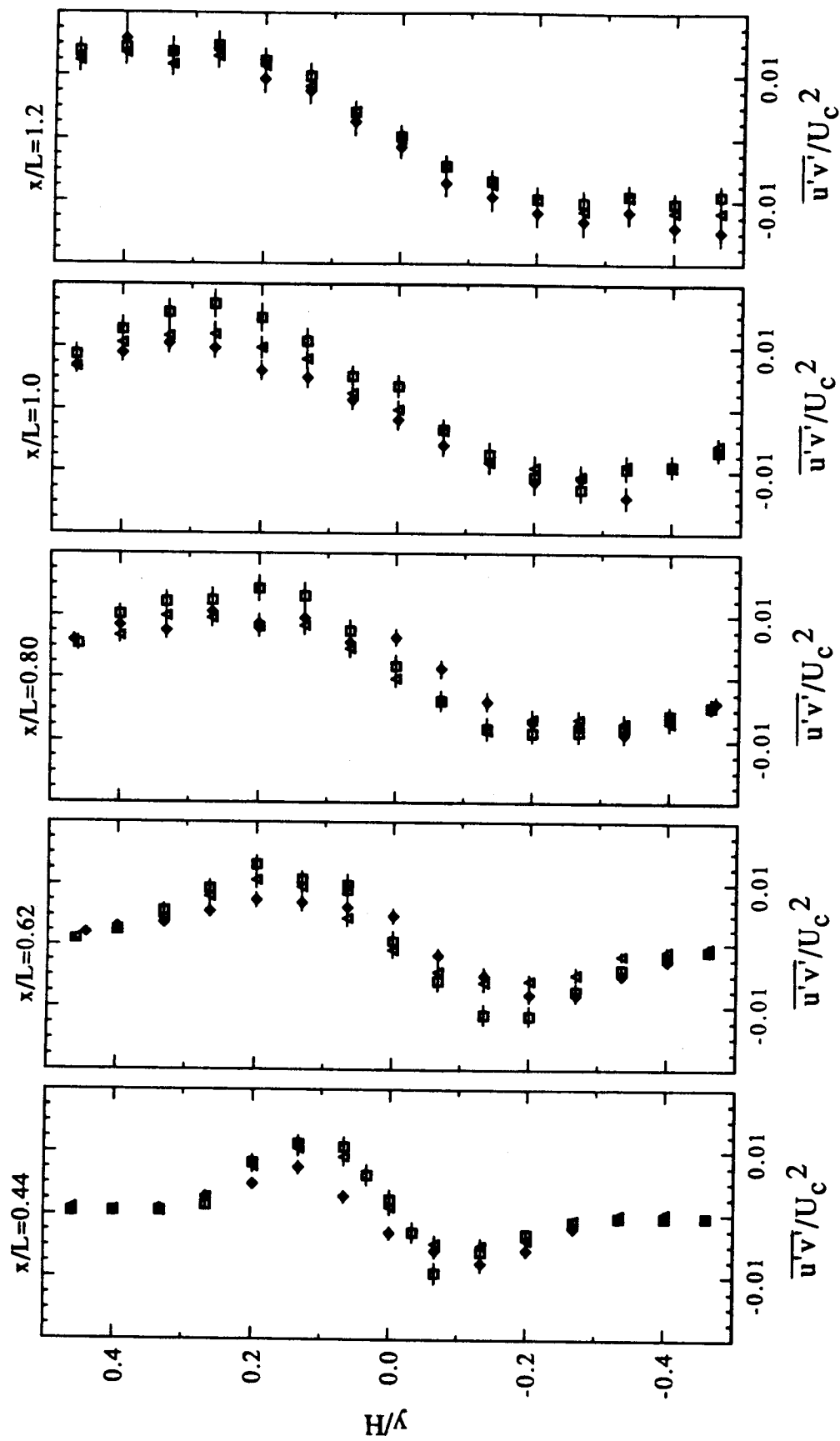


Figure 58: U-V Reynolds stress profiles at $z/d = -2.6$ (\square), -3.9 (Δ), and -5.2 (\diamond) obtained by LDV for $0.44 \leq x/L \leq 1.2$.

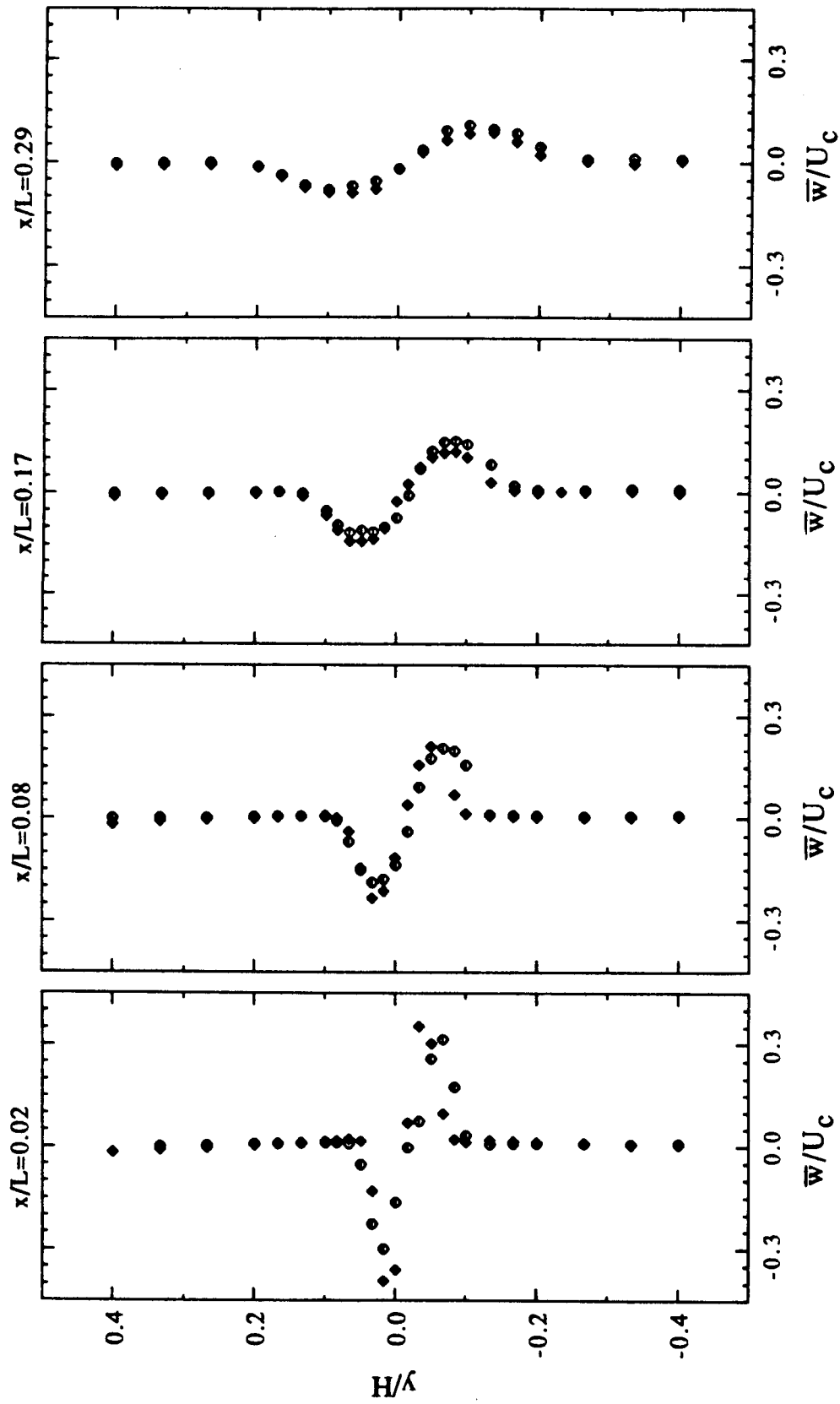


Figure 59: Vertical velocity profiles at $z/d = -2.6$ (\diamond) and -3.9 (\circ) obtained by hot wire anemometry for $0.02 \leq x/L \leq 0.29$.

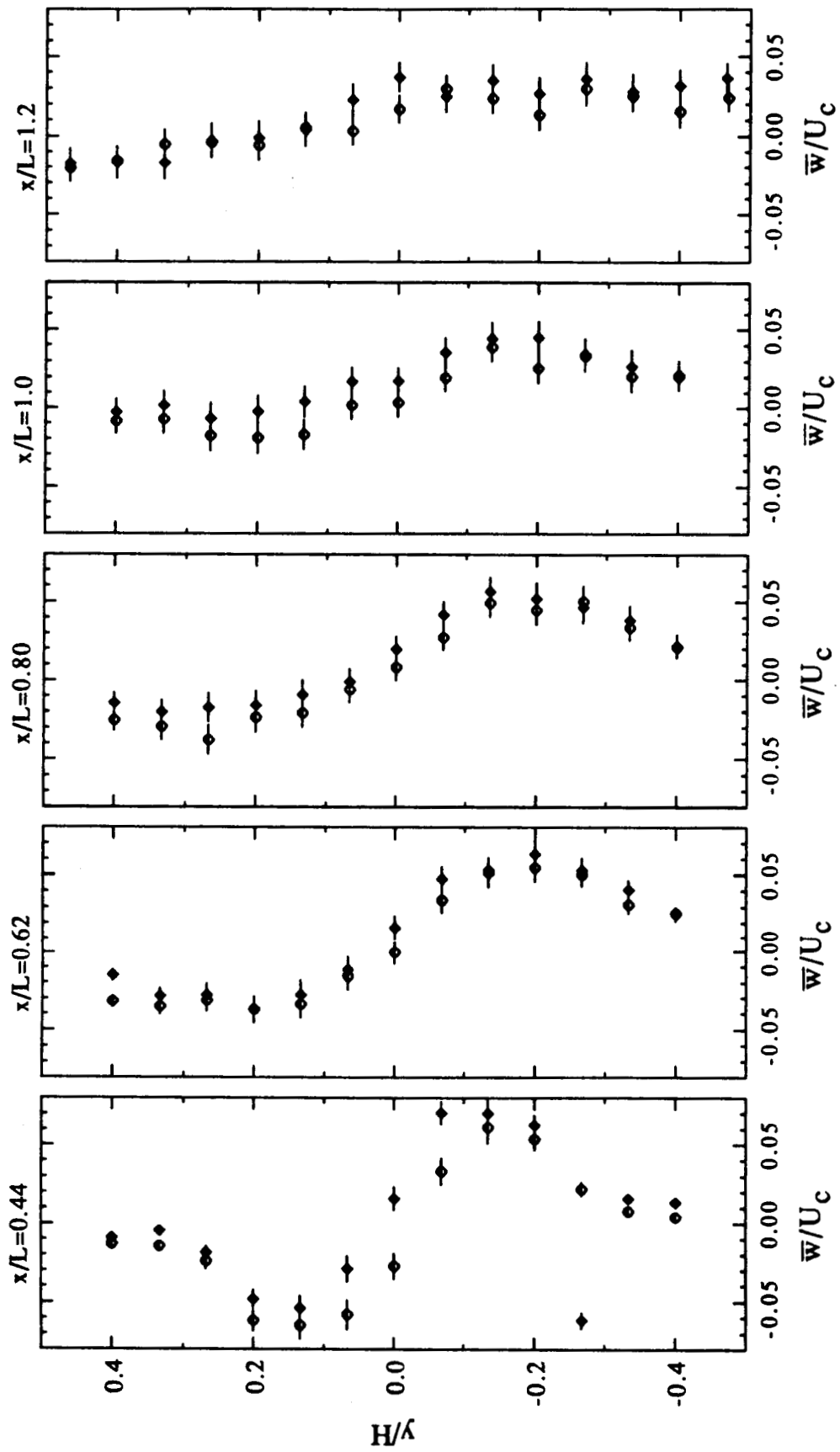


Figure 60: Vertical velocity profiles at $z/d = -2.6$ (♦) and -3.9 (○) obtained by hot wire anemometry for $0.44 \leq x/L \leq 1.2$.

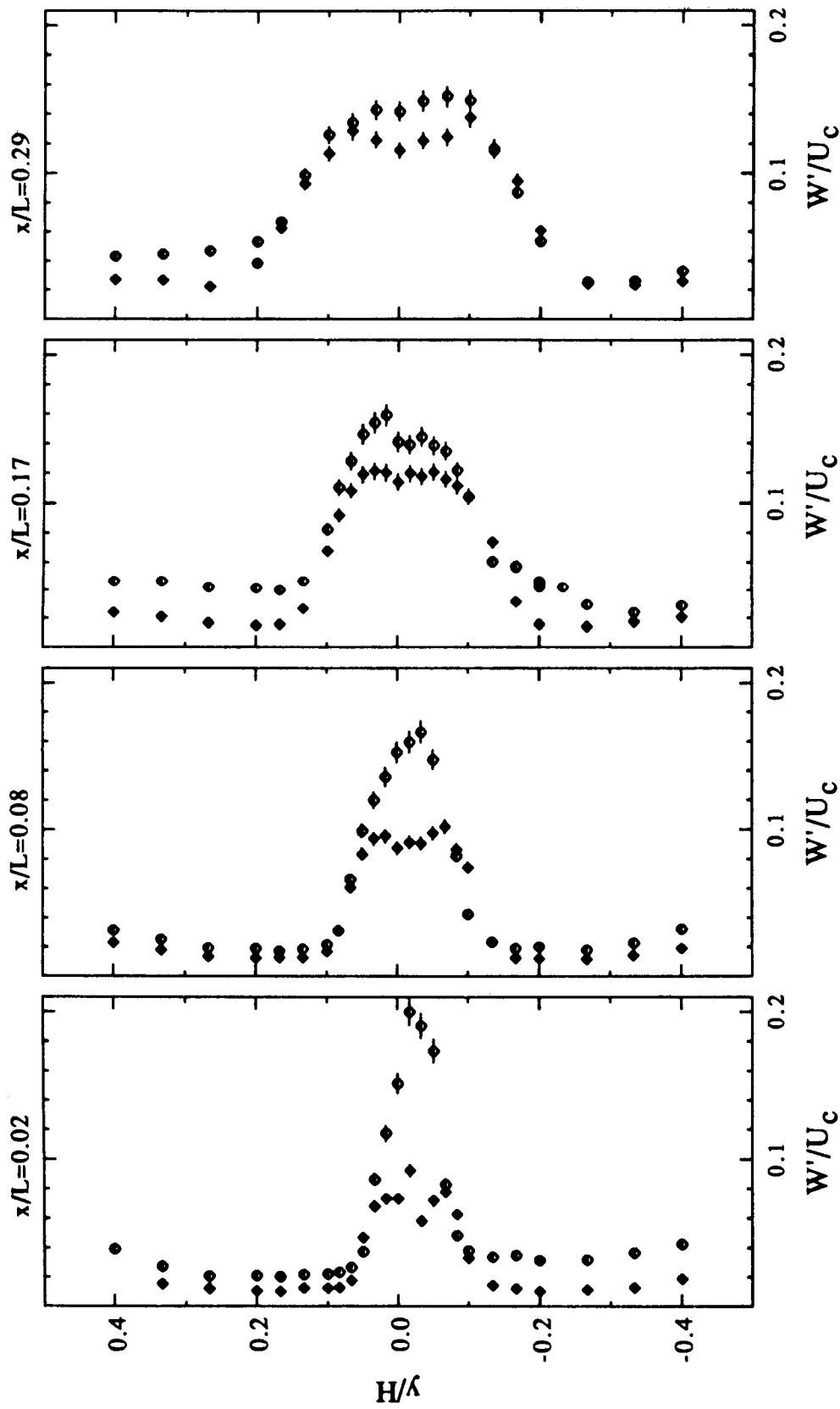


Figure 61: Vertical turbulence intensity profiles at $z/d = -2.6$ (\diamond) and -3.9 (\circ) obtained by hot wire anemometry for $0.02 \leq x/L \leq 0.29$.

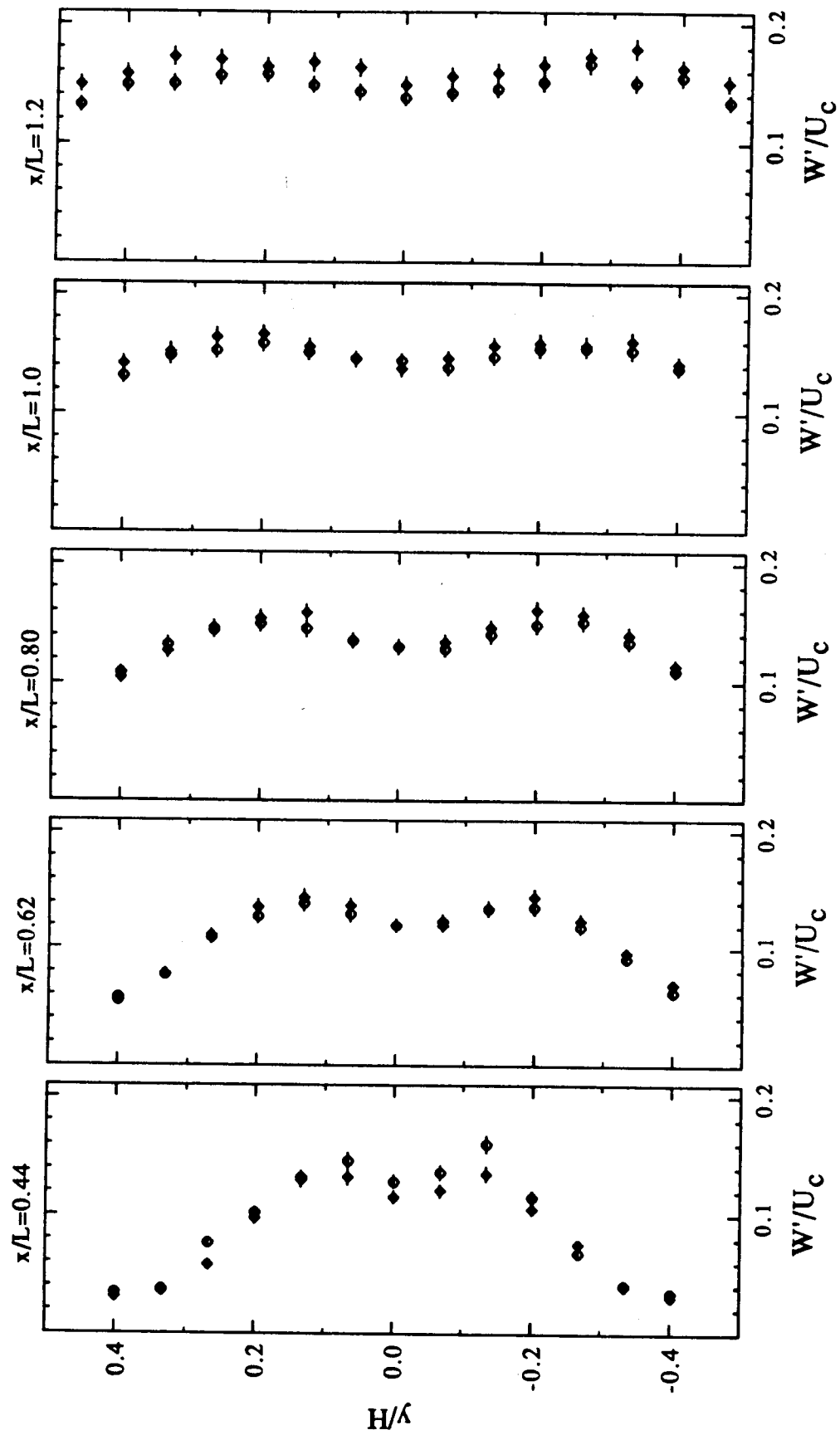


Figure 62: Vertical turbulence intensity profiles at $z/d = -2.6$ (♦) and -3.9 (◊) obtained by hot wire anemometry for $0.44 \leq x/L \leq 1.2$.

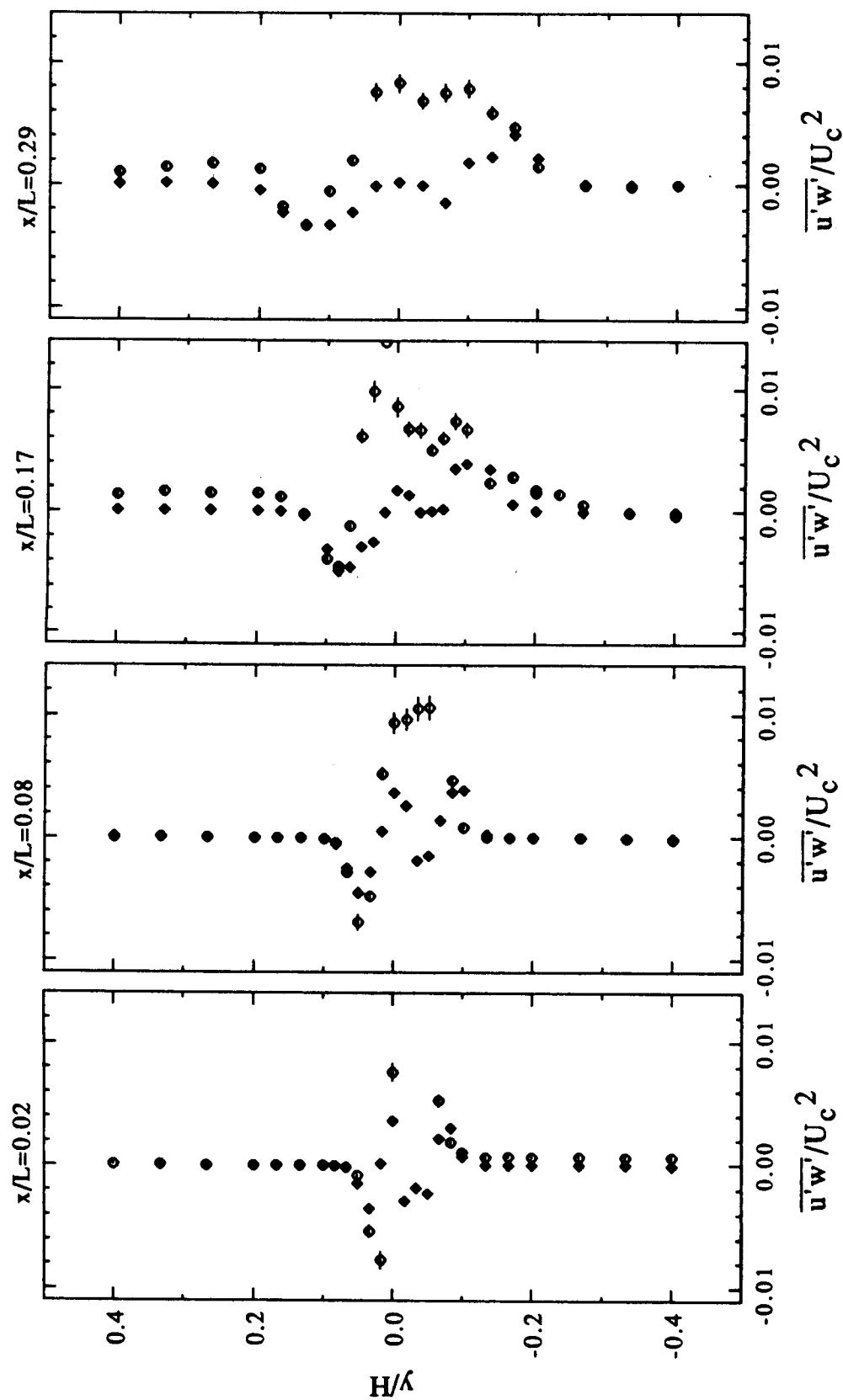


Figure 63: U-W Reynolds stress profiles at $z/d = -2.6$ (\bullet) and -3.9 (\blacklozenge) obtained by hot wire anemometry for $0.02 \leq x/L \leq 0.29$.

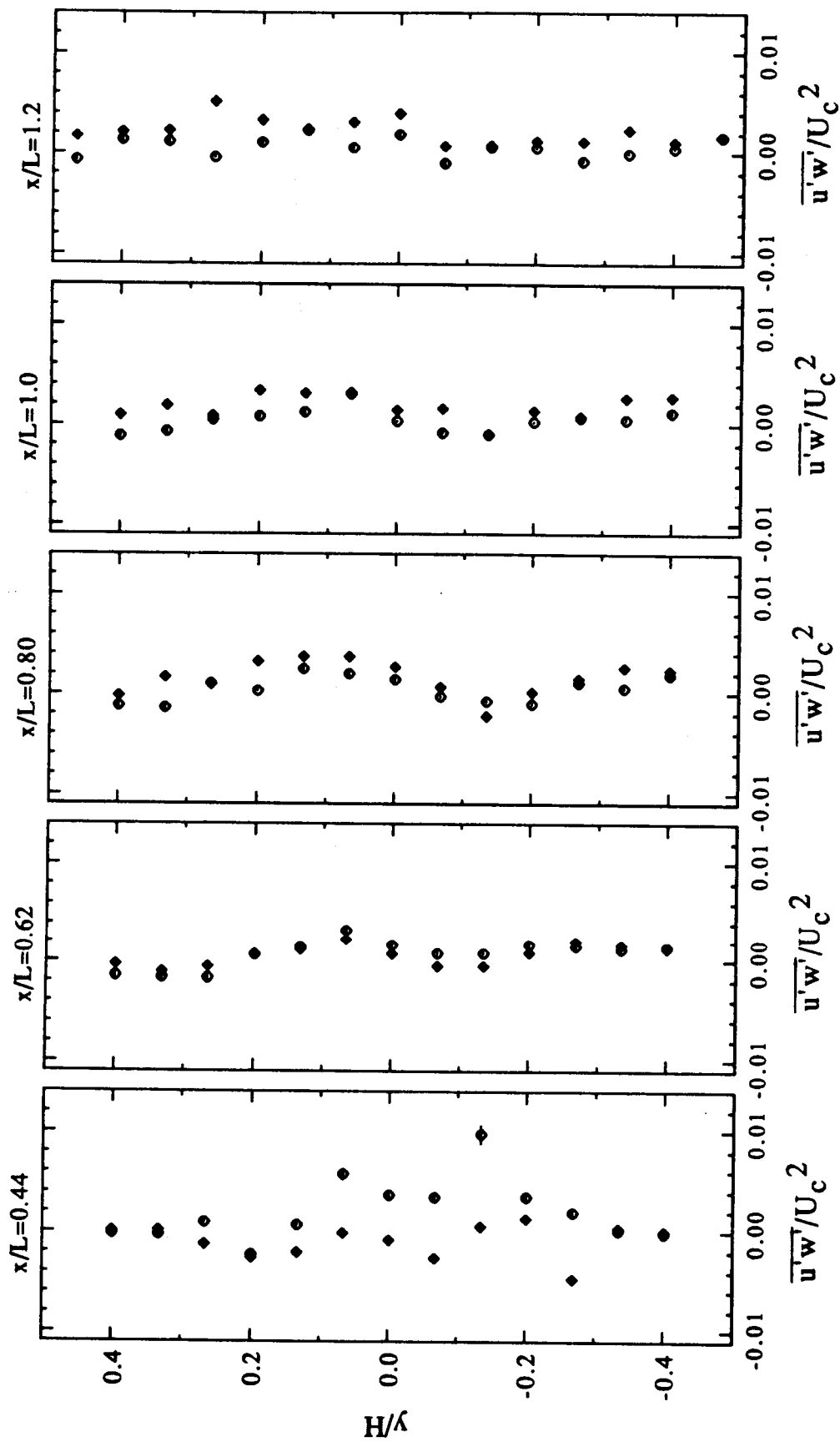


Figure 64: U-W Reynolds stress profiles at $z/d = -2.6$ (\diamond) and -3.9 (\circ) obtained by hot wire anemometry for $0.44 \leq x/L \leq 1.2$.

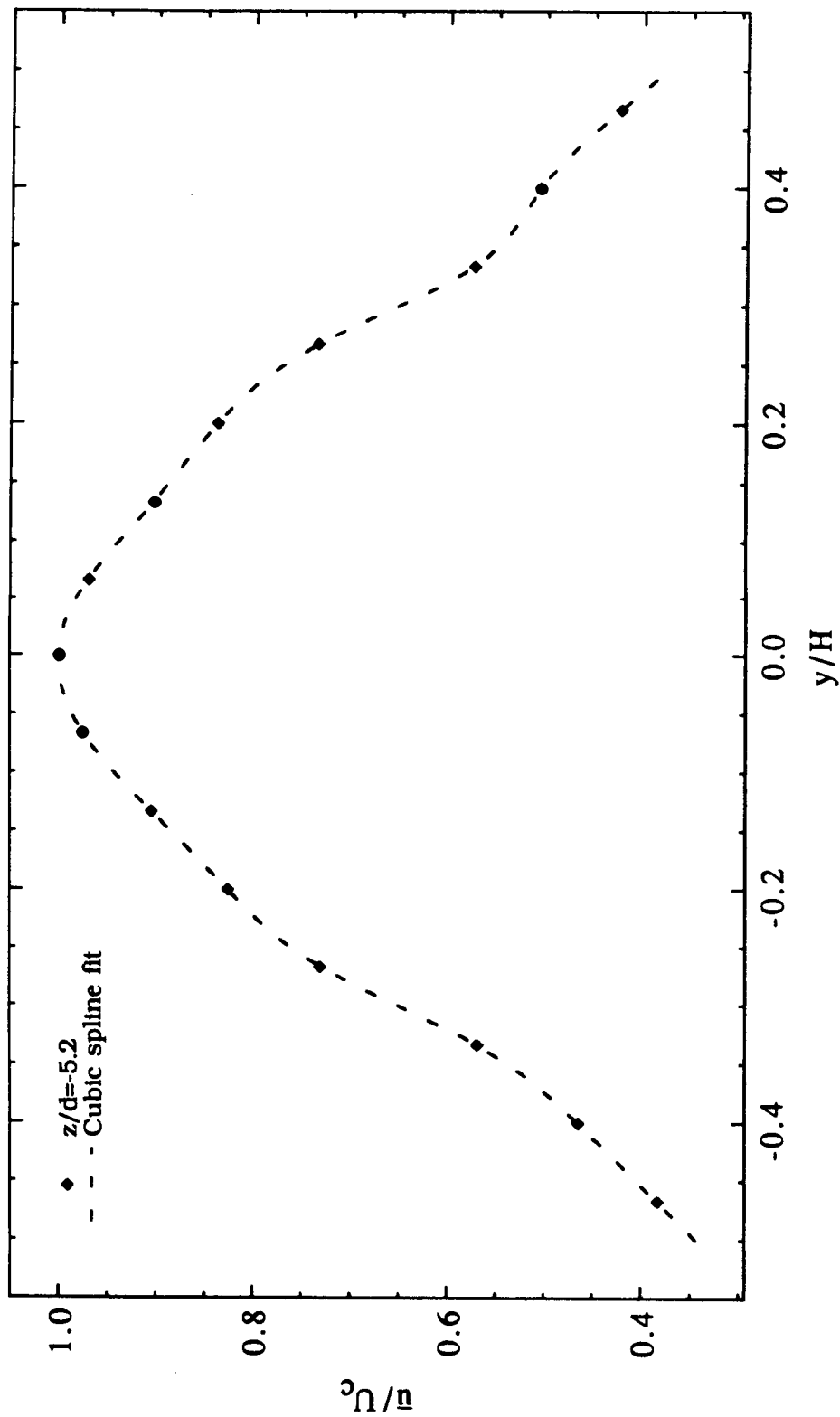


Figure 65: Axial velocity profile at mixing chamber exit for $z/d = -5.2$ and the cubic spline fit used in the ejector thrust calculation.

APPENDIX B
Sample Calculations

Primary Nozzle Exit Velocity Calculation

The nozzle exit velocity is calculated from the isentropic expansion of the nozzle total pressure to the static pressure at the nozzle exit. For the data point of Fig. 20:

$$u_e = \sqrt{2(p_o - p_e) / \rho_e}$$

$$\rho_e = \frac{p_e}{RT_e}$$

$$p_e = 14.68 \text{ psia} - 0.0514 \text{ psid} = 14.629 \text{ psia}$$

$$T_e = 56^\circ\text{F} + 460 = 516^\circ\text{R}$$

$$\begin{aligned}\rho_e &= \frac{(14.629 \text{ psia})(144 \text{ in}^2/\text{ft}^2)}{(32.2 \text{ lb}_m/\text{slug})(53.3 \text{ ft lb}_f/\text{lb}_m^\circ\text{R})(516^\circ\text{R})} \\ &= 0.0023787 \text{ slug/ft}^3 = 1.225 \text{ kg/m}^3\end{aligned}$$

$$p_o - p_e = 1.622 \text{ psid} + 0.0514 \text{ psid} = 1.673 \text{ psid}$$

$$u_e = \left[\frac{2(1.673 \text{ psid})(144 \text{ in}^2/\text{ft}^2)}{(0.0023787 \text{ slug/ft}^3)} \right]^{1/2}$$

$$= 443.1 \text{ ft/s} = 135.1 \text{ m/s}$$

The highest normalized centerline velocity obtained was 0.938.

Incorporating this correction for pipe and nozzle losses yields:

$$u_e = (0.938)(135.1 \text{ m/s}) = 126.7 \text{ m/s}$$

Ejector Thrust Calculation

The ejector thrust is calculated from the fluid momentum at the exit of the mixing chamber. This calculation includes the integration of the exit velocity profile at $z/d=-5.2$ as follows:

$$T_{ej} = \int_A \rho u (u \cdot dA) = \rho S \int_{-H}^{+H} u^2 dy$$

$$\rho = \frac{p}{RT}$$

$$p = p_{amb} = 14.68 \text{ psia}$$

$$T = 68^\circ\text{F} + 460 = 528^\circ\text{R} \quad (\text{ambient temperature})$$

$$\begin{aligned} \rho &= \frac{(14.68 \text{ psia})(144 \text{ in}^2/\text{ft}^2)}{(32.2 \text{ lb}_m/\text{slug})(53.3 \text{ ft lb}_f/\text{lb}_m^\circ\text{R})(528^\circ\text{R})} \\ &= 0.0023328 \text{ slug/ft}^3 = 1.2017 \text{ kg/m}^3 \end{aligned}$$

$$S = 0.1143 \text{ m} \quad (\text{mixing chamber height})$$

$$\int_{-H}^{+H} u^2 dy = 47.232 \text{ m}^3/\text{s}^2 \quad (\text{from integration of Fig. 65})$$

$$T_{ej} = (1.225 \text{ kg/m}^3)(0.1143 \text{ m})(47.232 \text{ m}^3/\text{s}^2)$$

$$= 6.4875 \text{ N}$$

Primary Nozzle Thrust and Augmentation Ratio Calculations

The nozzle thrust is calculated from the fluid momentum at the jet exit as follows:

$$T_n = \rho_e u_e^2 A_e$$

$$\rho_e = \frac{p_e}{RT_e}$$

$$p_e = p_{amb} = 14.68 \text{ psia}$$

$$T_e = 57^\circ\text{F} + 460 = 517^\circ\text{R} \quad (\text{primary flow temperature})$$

$$\begin{aligned} \rho_e &= \frac{(14.68 \text{ psia})(144 \text{ in}^2/\text{ft}^2)}{(32.2 \text{ lb}_m/\text{slug})(53.3 \text{ ft lb}_f/\text{lb}_m^\circ\text{R})(517^\circ\text{R})} \\ &= 0.0023824 \text{ slug}/\text{ft}^3 = 1.2273 \text{ kg}/\text{m}^3 \end{aligned}$$

The exit velocity is calculated from the isentropic expansion to ambient pressure since no confining walls are present in the free jet configuration.

$$\begin{aligned} u_e &= \sqrt{2(p_o - p_{amb}) / \rho_{amb}} \\ &= \left[\frac{2(16.81 \text{ psia} - 14.68 \text{ psia})(144 \text{ in}^2/\text{ft}^2)}{(0.0023824 \text{ slug}/\text{ft}^3)} \right]^{1/2} \\ &= 507.2 \text{ ft}/\text{s} = 154.6 \text{ m}/\text{s} \end{aligned}$$

A value of 0.897 was obtained for the normalized centerline velocity on the date of the mixing chamber exit survey used in the ejector

thrust calculations. Incorporating this correction for pipe and nozzle losses yields:

$$u_e = (0.897)(154.6 \text{ m/s}) = 138.7 \text{ m/s}$$

The exit area of the primary nozzle is calculated as the sum of the area of the twelve nozzle segments:

$$A_e = (0.094 \text{ in})(0.281 \text{ in})(12) = 0.317 \text{ in}^2 = 2.045 \times 10^{-4} \text{ m}^2$$

Finally, the computed primary nozzle thrust is:

$$\begin{aligned} T_n &= (1.2273 \text{ kg/m}^3)(138.7 \text{ m/s})^2 (2.045 \times 10^{-4} \text{ m}^2) \\ &= 4.8262 \text{ N} \end{aligned}$$

Thrust Augmentation Ratio:

$$\begin{aligned} \phi &= T_{ej} / T_n \\ &= 6.4875 / 4.8262 = 1.344 \end{aligned}$$

APPENDIX C
LDV Performance

PRECEDING PAGE BLANK NOT FILMED

An underlying purpose of this study was to evaluate the performance of the new two-component fiberoptic LDV made by TSI. This LDV system was intended to be used in the backscatter light collection mode as illustrated previously in Fig. 15. However, the low signal-to-noise ratio encountered in the backscatter mode necessitated the modification to forward scatter light collection as illustrated in Fig. 16. All flow field measurements were obtained in this configuration. Because of the seeding quality and other variables, backscatter measurements of the flow field were not possible.

In an effort to quantify the relatively poor backscatter performance, measurements of the signal-to-noise ratio were made at the end of the mixing chamber in a near ideal flow. Without primary jet flow, measurements were obtained between the glass surfaces in the low-turbulence potential core of a small axisymmetric jet seeded with mineral oil. At a laser power of 680 mW, the estimated signal-to-noise ratio in both forward and backscatter is tabulated below for each respective beam pair. All measurements are in decibels.

	Green	Blue
Forward Scatter	20-30	25-35
Backscatter	5-15	7-20

There are a few recommendations for improvement of the backscatter performance. An optimization of the receiving optics may show the greatest results as the precise location of the receiving focus was difficult to determine. The use of a FFT data acquisition routine may also be advantageous. This method of data analysis has

been shown to facilitate the measurement of flows with low signal-to-noise ratios that are not possible with standard counter processors.

Another factor unrelated to the LDV optics is the operation of the laser light source. It should be noted that lasers with older plasma tubes often develop modes that are counter-productive to LDV operation. This was believed to be the case with the laser used in this experiment. Since these modes typically occur at relatively high power levels, measurements were obtained at laser power levels between 700 and 800 milliwatts. At a higher power with a new plasma tube, the signal-to-noise ratio of this LDV system may be increased.

Included below is the procedure used to obtain a measurable signal and a valid velocity measurement using the TSI fiberoptic probe in the forward scatter configuration.

1. Set photomultiplier tubes to maximum power.
2. Adjust laser power and aperture to yield a satisfactory Doppler burst for blue, the weakest of the beam pairs. A typical waveform on an oscilloscope should resemble a sine wave and measure 0.6 to 0.8 volts peak-to-peak at its maximum. For the Spectra-Physics model 165, the optimum laser power was determined to be 0.75 watts.
3. Monitor both the blue and green waveforms on an oscilloscope with the scales set to 0.2 V/division and 0.2 μ s/division.
4. Adjust the seeding density so that the Doppler bursts are separated by at least 100 microseconds.

5. Adjust the thresholds of the counter processors to yield a coincident data rate that is approximately 20-40% of the individual data rates.
6. If the data rate drops noticeably, either/or:
 - a) Clean oil deposits from optical windows.
 - b) Adjust receiving fiber position to maximize the data rate.
 - c) Lower the thresholds when very close to the ejector walls.



Report Documentation Page

1. Report No. NASA CR-177531		2. Government Accession No.		3. Recipient's Catalog No.	
4. Title and Subtitle An Experimental Study of a Three-Dimensional Thrust Augmenting Ejector Using Laser Doppler Velocimetry				5. Report Date May 1989	
				6. Performing Organization Code	
7. Author(s) Bruce L. Storms				8. Performing Organization Report No.	
				10. Work Unit No. 505-61-21	
9. Performing Organization Name and Address California Polytechnic State University San Luis Obispo, California				11. Contract or Grant No. NCC2-484	
				13. Type of Report and Period Covered Contractor Report	
12. Sponsoring Agency Name and Address National Aeronautics and Space Administration Washington, DC 20546-0001				14. Sponsoring Agency Code	
15. Supplementary Notes Point of Contact: Jim Ross, Ames Research Center, MS 247-2, Moffett Field, CA 94035 (415) 694-6722 or FTS 464-6722					
16. Abstract <p>Flow field measurements have been obtained in a three-dimensional thrust augmenting ejector using laser Doppler velocimetry and hot wire anemometry. The primary nozzle, segmented into twelve slots of aspect ratio 3.0, was tested at a pressure ratio of 1.15. Results are presented on the mean velocity, turbulence intensity, and Reynolds stress progressions in the mixing chamber of the constant area ejector. The segmented nozzle was found to produce streamwise vortices that may increase the mixing efficiency of the ejector flow field. Compared to free jet results, the jet development is reduced by the presence of the ejector walls. The resulting thrust augmentation ratio of this ejector was also calculated to be 1.34.</p>					
17. Key Words (Suggested by Author(s)) Ejector Thrust augmentation Laser doppler velocimetry			18. Distribution Statement Unclassified-Unlimited Subject Category - 34		
19. Security Classif. (of this report) Unclassified		20. Security Classif. (of this page) Unclassified		21. No. of pages 135	
				22. Price A07	